WAGNER JOSÉ GONÇALVES DA SILVA PINTO

NUMERICAL AND EXPERIMENTAL ANALYSIS OF THE FLOW OVER A COMMERCIAL VEHICLE – PICKUP

UNIVERSIDADE FEDERAL DE UBERLÂNDIA

FACULDADE DE ENGENHARIA MECÂNICA

2016

WAGNER JOSÉ GONÇALVES DA SILVA PINTO

NUMERICAL AND EXPERIMENTAL ANALYSIS OF THE FLOW OVER A COMMERCIAL VEHICLE – PICKUP

Undergraduate thesis submitted to the Course of Aeronautical Engineering from the Federal University of Uberlândia as a part of requirement for obtaining the BACHELORS DEGREE ON AERONAUTICAL ENGINEERING.

Tutor: Prof. Dr. Odenir de Almeida

UBERLÂNDIA – MG

2016

WAGNER JOSÉ GONÇALVES DA SILVA PINTO

NUMERICAL AND EXPERIMENTAL ANALYSIS OF THE FLOW OVER A COMMERCIAL VEHICLE – PICKUP

Undergraduate thesis **APROVED** by the Course of Aeronautical Engineering from the Faculty of Mechanical Engineering of the Federal University of Uberlândia.

Thesis Committee Composition:

_____

Prof. Dr Odenir de Almeida

_____

Prof Dr. Francisco José de Souza

_____

Ing. Samara Cunha Rosa (FCA Fiat Chrysler Automobiles)

Uberlândia, 14 March 2016

ACKNOLEGEMENTS

First of all I'd like to thank the Federal University of Uberlândia (UFU) and more specifically the Faculty of Mechanical Engineering (FEMEC) for providing a high level academic formation that is concluded on the production of this manuscript. I am also grateful to the Fluid Mechanics Laboratory (MFLab) and its staff and colleagues for providing a great ambiance and the means for this work.

I personally thank MSc. Pedro Ricardo for all the support in all aspects regarding the numerical simulations, especially meshing, and Reinaldo Tome Paulino for the amazing work on the test article and all the efforts on improving the wind-tunnel facility. I'm very grateful to Prof. Dr. Odenir de Almeida for the advising and Ing. Samara Cunha for sharing her knowledge and experiences on the matter and promoting an industrial vision on this research.

Furthermore, I express my thanks to Isabela Iuriko for all the love, support and patience.

PINTO, W. J. G. S. P. **Numerical and Experimental Analysis of the Flow Over A Commercial Vehicle – Pickup.** 2016. 95 f. Trabalho de Conclusão de Curso, Universidade Federal de Uberlândia, Uberlândia.

RESUMO

As *pick-ups* compreendem uma importante categoria de veículo comercial por combinar o transporte de passageiros e de carga. A presença de uma caçamba aberta é responsável pela formação de uma topologia de escoamento única que é naturalmente de grande interesse para pesquisas dos fabricantes e que vem aos poucos sendo mais discutida em artigos acadêmicos. Este trabalho apresenta um estudo numérico e experimental do escoamento ao redor de uma *pick-up* genérica baseada nos líderes de mercado de pick-ups leves do Brasil. O modelo de *pick-up* proposto é composto apenas por superfícies planas e cantos vivos e é derivado de um estudo dimensional dos cinco principais modelos da categoria; uma segunda versão é concebida a partir do arredondamento desses cantos. Simulações são realizadas usando as equações de Navier-Stokes médias (RANS) no *software* STAR-CCM+ com o modelo de turbulência SST k-ω; malha é constituída de elementos tetraédricos e o efeito da camada de prisma é estudado. No túnel de vento, anemometria de fio quente e visualização parietal por tufos são utilizados num modelo 1:10 e são usadas como referência para validação inicial dos resultados numéricos. Apesar de uma nova geometria ser testada, resultados são similares aos presentes na literatura. Arredondar o modelo causou uma redução de 30% no arrasto; variações significativas na estrutura global do escoamento na caçamba e na esteira não são observadas. A solução computacional é preparada para o modelo reduzido e para a *pick-up* em tamanho real em velocidades típicas de rodovia; para a faixa de escalas testadas (Re de 5×10^5 a 5×10^6), acredita-se que o problema seja independente do Reynolds, desse modo dados obtidos em túnel de vento dinamicamente não similares ainda são representativos do escoamento real. Esse trabalho visa servir como referência para análises futuras e deste modo um estudo mais refinado de *setup* numérico (malha e *solver*) e a aplicação de outras rotinas experimentais é recomendado. A investigação de mecanismos de redução de arrasto e dos efeitos de outras modificações na geometria é sugerida para as próximas etapas.

Palavras-chave: Aerodinâmica Externa; Pick-up; CFD; Anemometria de Fio-Quente; Túnel de vento.

PINTO, W. J. G. S. P. **Numerical and Experimental Analysis of the Flow Over A Commercial Vehicle – Pickup.** 2016. 95 f. Trabalho de Conclusão de Curso, Universidade Federal de Uberlândia, Uberlândia.

ABSTRACT

The pickups correspond to an important category of commercial vehicle once they combine passenger and cargo transport. The presence of an open trunk is responsible for a unique flow topology within a natural great interest for manufacturer's research and that is gradually being more discussed on academic articles. This work presents a numerical and experimental study of the flow around a generic pickup based on the leaders of the light pickup market in Brazil. The proposed pickup model is composed only by flat surfaces and sharp edges and it's derived from a dimensional study of five principal models of the category; a second version is conceived with the application of fillets on those edges. Simulations are performed using Reynolds Averaged Navier Stokes equations (RANS) on STAR-CCM+ solver with SST k-ω turbulence model; mesh is constituted of tetrahedral elements and the effect of a prismatic boundary layer is studied. On wind-tunnel, hot-wire anemometry and wall tufts visualization techniques are deployed for 1:10 scale model and serve as a reference for numerical results initial validation. Although a new geometry is tested, the results are similar to previous works. Rounding the model caused a reduction of 30% in the drag coefficient; no significant change is noted on the overall distribution of the structures on trunk and wake. Computational solution is prepared for reduced and full size pickup on typical highway velocities; for the range of tested scales (Re from 5×10^5 to 5×10^6), problem is believed to be independent of Reynolds, therefore wind-tunnel data that is not dynamic similar is still representative of real flow. This work is aimed to serve as a benchmark for future analyses so that more refined examination on CFD setup (mesh and solver) and application of other experimental routines are recommended. The investigation of drag reducing devices and the effects of other geometry variations is suggested as next steps.

Key-words : External aerodynamics; Pickup; CFD; Hot-wire anemometry; Wind-tunnel.

LIST OF FIGURES

Figure 1.1 - Graphic depicting representative horsepower requirements versus vehicle speed for a heavy vehicle tractor-trailer truck (WOOD and BAUER, 2003). 7
Figure 1.2 - New passenger cars: CO_2 emissions by vehicle segment (The International Council on Clean Transportation, 2011). 7
Figure 1.3 - Drag coefficients of different commercial vehicles (HUCHO, 1987) 8
Figure 1.4 - Example of the effect of an aerodynamic add-on (cab-spoiler) in a truck (HUCHO, 1987). 9
Figure 2.1- Flow around a car and major locations of flow separation (HUCHO; SOVRAN, 1993). 13
Figure 2.2 - Proposed nomenclature for pick-up parts 14
Figure 2.3 - Generic pickup model proposed by Al-Garni; Bernal; Khalighi (2003). 15
Figure 2.4 – Mean pressure coefficient distribution along the symmetry plane on the pickup truck (AL-GARNI; BERNAL 2010). 15
Figure 2.5 - Streamlines of the mean velocity field in the symmetry plane of the wake (left) and on the horizontal plane at z = 15 mm behind tailgate (right) of pickup truck (AL-GARNI; BERNAL 2010). 16
Figure 2.6 - Proposed vortex system of the flow around a pickup (AL-GARNI; BERNAL 2010). 17
Figure 2.7 - Wake shape behind a pickup truck (MOKHTAR; BRITCHER; CAMP, 2009). 17
Figure 2.8 – Pickup drag coefficient range described on the literature. 18
Figure 4.1 – Reference pickup vehicles. 25
Figure 4.2 – Test article composing dimensions. 27
Figure 4.3 – Pickup models: baseline (left) and rounded (right). 29
Figure 4.4 – Refinement regions on symmetry plan (L is the pickup length; l is the trunk length; and W is the pickup width) 30
Figure 4.5 - Surface mesh of wheel (right) and trunk (left). 31

Figure 4.6 – Numerical surface mesh on symmetry plane and pickup (from top to bottom: TETRA, BASELINE and ROUNDED)..... 32
Figure 4.7 - Wind tunnel facility..... 35
Figure 4.8 – Pickup model parts..... 36
Figure 4.9 - Finalized pickup model..... 36
Figure 4.10 - Experimental setup..... 39
Figure 4.11 - Experimental setup (left). On detail (right) the hot-wire support and probe on position P1 and Pitot tube on test section roof..... 40
Figure 4.12 – Fluorescent minitufts on car moving at 160 km/h past stationary camera (MERZKIRCH, 1987)..... 40
Figure 4.13 - Model with wool tufts..... 41
Figure 4.14 - Experimental setup for wall tufts test..... 41
Figure 5.1 - Residuals monitor for simulation with the TETRA (top) and BASELINE (bottom) meshes (in scale, U_0 = 25 m/s)..... 43
Figure 5.2 - Evolution of numerical force coefficients for in scale TETRA (left) and BASELINE (right) meshes, U_0 = 25 m/s..... 43
Figure 5.3 – Evolution of partial average (left) and standard deviation (right) of drag coefficient sequence for baseline and rounded in scale model, U_0 = 25 m/s..... 44
Figure 5.4 - Normalized velocity field on symmetry plane, baseline model for TETRA (top) and BASELINE (bottom) meshes (in scale, U_0 = 25 m/s)..... 45
Figure 5.5 - Streamline on symmetry plane for TETRA (left) and BASELINE (right) mesh (in scale, U_0 = 25 m/s)..... 46
Figure 5.6 - Streamline on center of trunk for TETRA (top) and BASELINE (bottom) meshes (in scale, U_0 = 25 m/s)..... 46
Figure 5.7 – Evolution of Turbulent Kinetic Energy on pickup trunk and wake for TETRA (top) and BASELINE mesh (bottom)..... 47
Figure 5.8 - Axis system..... 47
Figure 5.9 - Pressure coefficient on symmetry plane of the cab, bed and underbody for TETRA and BASELINE meshes (in scale, U_0 = 25 m/s)..... 49
Figure 5.10 - Pressure coefficient on symmetry plane of the cabin rear surface and tailgate for TETRA and BASELINE meshes (in scale, U_0 = 25 m/s)..... 49
Figure 5.11 – Streamwise velocity field in symmetry plane and vectors on tested points for BASELINE mesh at wind tunnel conditions (in scale, U_0 = 25.0 m/s)..... 50

Figure 5.12 - Numerical and experimental velocity profiles at U_0 = 16.7 m/s (top) and U_0 = 25.0 m/s (bottom). 52
Figure 5.13 - Experimental velocity profiles limits for U_0 = 16.7 m/s (top) and U_0 = 25 m/s (bottom). 53
Figure 5.14 – Spectral energy distribution for velocity signal acquired at P2 (left) and P3 (right), Z = 55 mm (U_0 = 25 m/s), using unity as reference for decibels (smoothed curve in red). 54
Figure 5.15 - Spectral energy distribution of measured velocities on pickup wake at P2 (top line) and P3 (bottom line) for U_0 = 16.7 m/s (left column) and U_0 = 25.0 m/s (right column), using unity as reference for decibels. 56
Figure 5.16 – Wall tufts on trunk for U_0 = 10.0 m/s (left), U_0 = 16.7 m/s (center) and U_0 = 25.0 m/s (right). 57
Figure 5.17 – Wall tufts on trunk for U_0 = 10 m/s (top), U_0 = 16.7 m/s (center) and U_0 = 25.0 m/s (bottom). 58
Figure 5.18 – Trunk close wall flow topology for wall tufts test (center) and shear stress streamlines on trunk surface for TETRA (left) and BASELINE (right) mesh (U_0 = 25.0 m/s). 59
Figure 5.19 – Wall tufts (center) and numerical shear streamlines for TETRA (left) and BASELINE (right) mesh (U_0 = 25 m/s). 59
Figure 5.20 – Normalized velocity field on symmetry plane, baseline model U_0 = 25 m/s..... 61
Figure 5.21 – Normalized velocity field on symmetry plane, rounded model U_0 = 25 m/s..... 62
Figure 5.22 - Streamline on center of trunk for baseline (top) and rounded (bottom) models (in scale, U_0 = 25 m/s). 62
Figure 5.23 - Pressure coefficient on symmetry plane of the cab, bed and underbody for baseline and rounded models (in scale, U_0 = 25 m/s). 63
Figure 5.24 – Pressure coefficient on symmetry plane of the cabin rear surface and tailgate for baseline and rounded models (in scale, U_0 = 25 m/s). 64
Figure 5.25 – Surface pressure coefficient on rear cabin and tailgate exterior (top) and on bed and tailgate interior (bottom) for baseline (left) and rounded (right) models (in scale, U_0 = 25 m/s). 65
Figure 5.26 – Iso-surface of $\lambda_2 = -4.0 \times 10^4$ s^{-2} for baseline model, in scale U_0 = 25 m/s. 66
Figure 5.27 – Iso-surface of $\lambda_2 = -4.0 \times 10^4$ s^{-2} for rounded model, in scale U_0 = 25 m/s. 66

Figure 5.28 – Iso-velocity surface for 1/3 of freestream velocity: U_0 = 16.67 m/s (left column), U_0 = 25.00 (center column) and U_0 = 33.33 m/s (right column), for baseline(top line) and rounded (bottom line) in scale models. 69
Figure 5.29 - Pressure coefficient on symmetry plane of the cab, bed and underbody of the baseline model in all scales. 70
Figure 5.30 – Pressure coefficient on symmetry plane of the cabin rear surface and tailgate of the baseline model in all scales. 70
Figure 5.31 - Pressure coefficient on symmetry plane of the cab, bed and underbody of the rounded model in all scales. 71
Figure 5.32 – Pressure coefficient on symmetry plane of the cabin rear surface and tailgate of the rounded model in all scales..... 71
Figure 5.33 - Streamline on symmetry plane for rounded model in scale (left) and full size (right) for U_0 = 16 m/s (top), U_0 = 25 m/s (center) and U_0 = 33 m/s (bottom)..... 72
Figure 5.34 - Normalized velocity field on symmetry plane at Re1 (top) and Re6 (bottom) for rounded model..... 73
Figure 5.35 - Streamline on center of trunk for rounded model for two scales: Re1 (top) and Re6 (bottom). 74
Figure 5.36 – Iso-velocity surface for 1/3 of freestream velocity for Re1 (top) and Re6 (bottom) for rounded model (structures on upstream of the model are omitted). 74
Figure 5.37 - Drag coefficient for all on scales. 75
Figure 5.38- Percentage C_D oscillation from all scales average value for baseline and rounded models..... 76

LIST OF TABLES

Table 4.1 – Brazilian Light pickups licensing in July 2014 (FENABRAVE, 2014)..... 24
Table 4.2 – Pickup models dimensions..... 26
Table 4.3 – Statistics of dimensions analysis. 28
Table 4.4 - Overall dimensions and blockage ratio of generic pickup models in the literature. .. 29
Table 4.5 - Simulations Matrix..... 34
Table 5.1 – Positions and frequencies of maximum spectral energy peaks on pickup wake. 55
Table 5.2 – Tested scales..... 68

SUMMARY

CHAPTER 1 - Introduction **6**
CHAPTER 2 - Phenomenology **11**
2.1. Fundamentals of Automotive Aerodynamics 11
2.2. Pickup aerodynamics 14
CHAPTER 3 - Bibliographic review **19**
CHAPTER 4 - Methodology **24**
4.1. Test Article 24
4.2. Numerical 30
4.2.1. Numerical Domain and Mesh 30
4.2.2. Boundary Conditions and Solver 33
4.3. Experimental setup 35
4.3.1. Wind tunnel Facility and Model 35
4.3.2. Quantitative method - Hot-wire Anemometry 37
4.3.3. Qualitative method - Wall Tufts 40
CHAPTER 5 - Results and Discussions **42**
5.1. Numerical Solution Properties and Validation 42
5.1.1. Numerical Solution Properties 42
5.1.2. Mesh study 45
5.1.3. Experimental Results and Validation 50
5.1.3.1. Quantitative – Velocity Profiles 50
5.1.3.2. Qualitative – Wall Tufts Visualization 57
5.2. Model study 61
5.3. Scale study 68
CHAPTER 6 - Conclusion **77**
REFERENCES **79**

APPENDIX I **82**
APPENDIX II **83**
I - Boundary layer 84
II – Calibration and Turbulence Intensity 85

CHAPTER I

Introduction

The development of the automotive industry is close related with the technological advances. Significant market and a global concurrence demands constant improvement from the production chain to the final product. In the 20's century, the power plants can be considered the component that most evolved, achieving better performance and less consumption. Following this trend, aerodynamic aspects defined the design of modern vehicles and continue to shape cars.

A compromise between safety, performance and design is performed by each manufacturer. The balance between those domains, directly influenced by financial and productive aspects, is the key to a better vehicle. The variety of models and the complexity of the flow related to each one of them, summed to the dynamics of human occupation and transports needs, demand a continuous evolution of the techniques.

The movement of a car is constraint mainly by two factors: rolling resistance and aerodynamic forces. In general, for commercial vehicles, after 90 km/h, typical highway speed, aerodynamic effects are the major source of those restraining forces, also contributing to instability when lateral forces and moments are taken in account. Therefore, the reduction of drag affects directly the performance and the CO_2 emission. Figure 1.1 presents the evolution of aerodynamic and rolling forces with the speed for a heavy vehicle tractor trailer truck. After 50 mph (80 km/h) the drag is the most important component.

Environmental concerns demand from all transportation industry consistent noise and consumption reduction, so that there are constant reformulation and creation of related legislation, in both national and global context. The new standards play an important role in pushing the development of the industry, as seen in Figure 1.2, the average CO_2 emission dropped for all segments in the European market from 2001 to 2010.

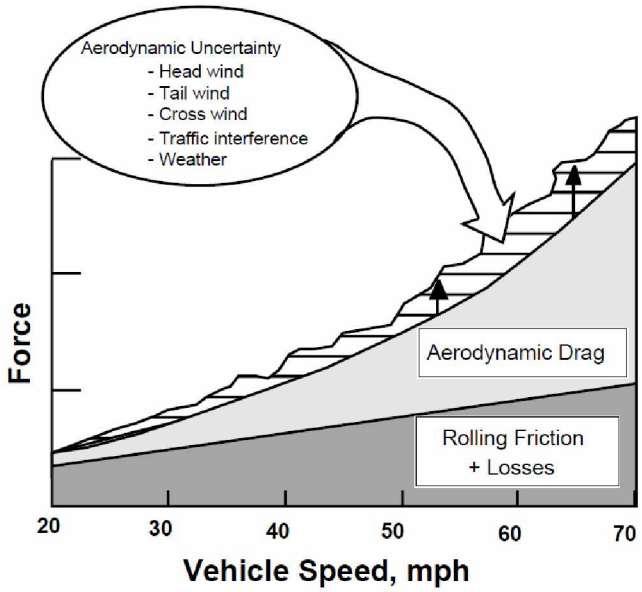

Figure 1.1 - Graphic depicting representative horsepower requirements versus vehicle speed for a heavy vehicle tractor-trailer truck (WOOD and BAUER, 2003).

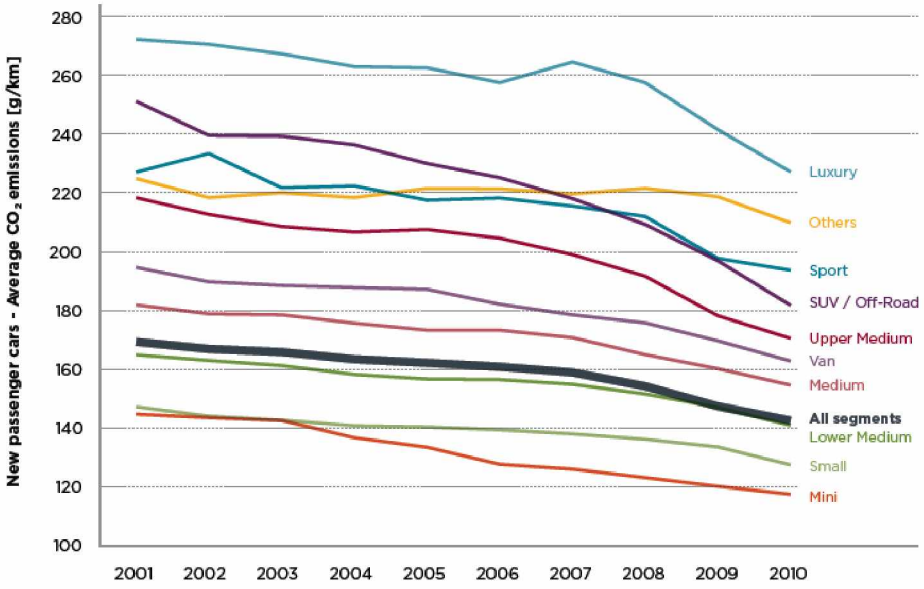

Figure 1.2 - New passenger cars: CO_2 emissions by vehicle segment (The International Council on Clean Transportation, 2011).

A notable example of such initiatives is the INOVAR-AUTO program (Brazilian law number 12,715 of 2012) that intends to promote R&D investments for companies that produce, distribute or present projects to invest in the automotive production in Brazil. One of its pillars is reducing fuel consumption: a decrease of 18.84% by 2017 will result in 2% direct tax deduction for the final product.

Such aspects are aligned with the pursuit for more comfort and economical differentials, pushing the competitors to comprehend and optimize all the phenomenology associated with fuel consumption. The most touched category is commercial vehicles, such as trucks, buses, vans and pick-ups, mostly for its large use and unique geometry that results in bigger drag than for those of passengers' cars (see Figure 1.3). The limitations created by theirs applications requirements, space for cargo, demands more creative solutions and the deployment of multiple engineering tools.

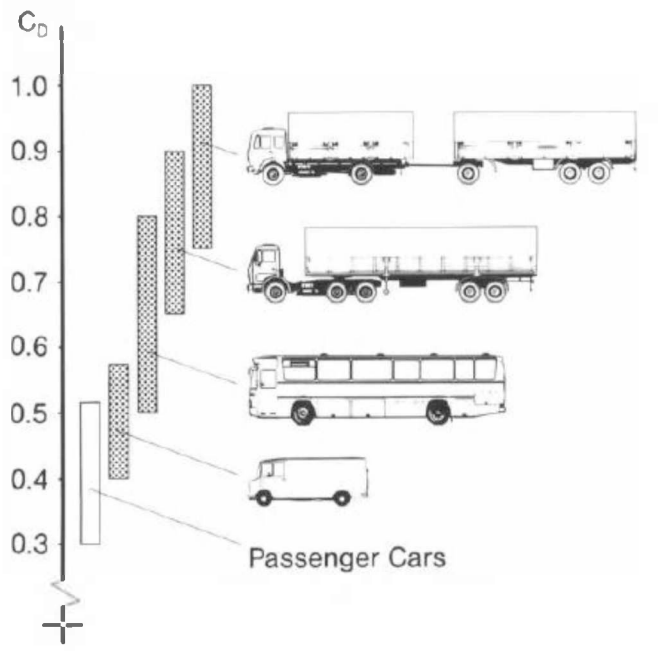

Figure 1.3 - Drag coefficients of different commercial vehicles (HUCHO, 1987).

The most common aerodynamic structures are the vortex formed on the cab and a big recirculation zone after the trunk. The wake and the recirculating zones are the principal sources of drag and must be modified in order to achieve less consumption. For trucks, the interaction between the tractor and the trailers are also a significant source of drag. Besides the global

geometric modifications, both passive and active flow control techniques can be used to reconfigure flow path, however, the second one must be proven to be energetically lucrative. Spoilers and flaps, for example, are used to drop the strength of recirculation bubbles, to extinguish or retard transition/separation points, reducing and modifying vortex positions, thus decreasing the pressure difference and the related forces. Figure 1.4 exemplifies the effect of a cab-spoiler attaching the flow to the top of the trailer.

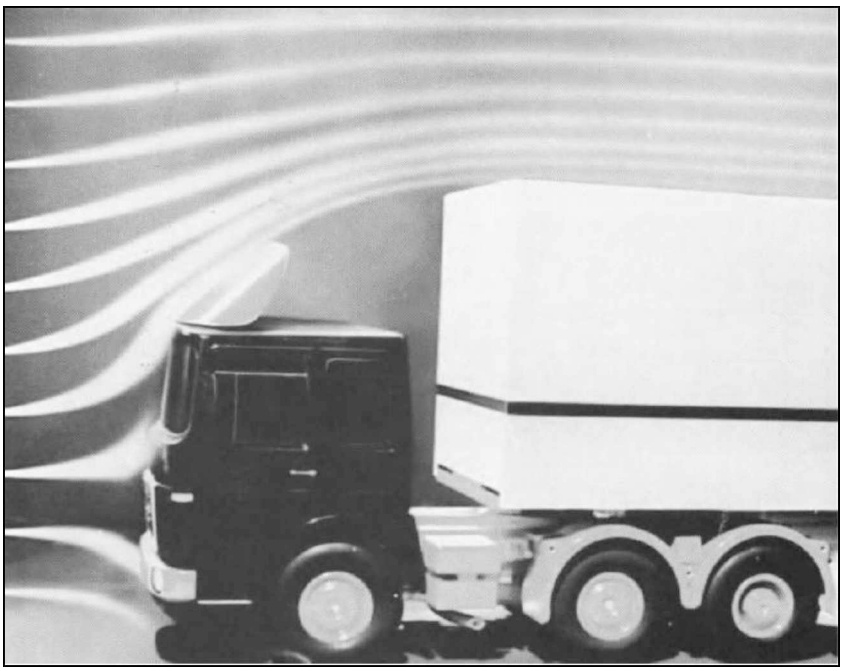

Figure 1.4 - Example of the effect of an aerodynamic add-on (cab-spoiler) in a truck (HUCHO, 1987).

Pickups are used as commercial and as passenger vehicles. Despite being similar to SUV's, the existence of the open trunk is unique in terms of airflow behavior and the fact that pickups presents a bigger drag coefficient is more appealing in terms of the pursuit of fuel saving.

The mix of passengers and cargo fills a specific demand but remains representative in the automotive market. In 2014, according to FENABRAVE (*Federação Nacional da Distribuição de Veículos*) they comprehend 83.11 % of the licensing for the light commercial subsegment (composed by pickups and vans) what represented 12.68 % of total brazilian automotive market

(including cars, trucks and buses). In November 2015, pick-ups represented 9% of auto sales in United States according to the Wall Street Journal.

Although the analysis of the external flow around pickups is mostly restrict to the manufactures, it attracts academic work for its complex tridimensional flow, even serving as test case for numerical algorithms. Experimental and numerical works discuss the subject, focused mostly in flow description and drag estimation/reduction techniques.

This study is aimed to the general description of the external flow around a pickup vehicle. A simplified model is prepared from averaged dimensions of the vehicles with the biggest market share in the brazilian light pickups market: Fiat Strada; Volkswagen Saveiro; Chevrolet Montana; Peugeot Hoogar; and Ford Courier. Baseline test article is composed by sharp edges and second version is prepared applying fillets to all external edges.

Analysis is performed numerically using averaged Navier Stokes equations (RANS) and experimentally in a subsonic wind-tunnel (hot-wire anemometry and wall tufts visualization). The experiments are performed with a 1:10 scale version and numerical analyses are done with in scale pickup and full model.

The second chapter is dedicated to the description of the fundamentals of automotive aerodynamics and of the flow around a pickup truck, summarizing the literature conclusions. A discussion of all the academic work on the matter is presented in the third chapter. Forth chapter is dedicated to present the definition of the pickup generic model and both numerical and experimental methods. Chapter five summarizes the results and discussions concerning wind tunnel tests and CFD validation, the effects of the prismatic boundary and geometric variation (rounded model) and the performed scale study.

CHAPTER II

Phenomenology

This chapter is dedicated to the description of the fundamentals of automotive aerodynamic analysis and to summarize previous conclusions on the flow present around a pickup.

2.1. Fundamentals of Automotive Aerodynamics

The study of automotive aerodynamics deals with both internal and external flow. Engine feeding, systems cooling, thermal and acoustics comfort are the main focus on the first domain. For the exterior of the car, most important aerodynamic quantities are the forces and momentums, directly influencers of the vehicle stability and consumption.

Lift and drag are the most discussed aerodynamic forces, especially when cross-wind is not considered. The first one is responsible for reducing adherence of the tires and the second one operates against the movement of the automobile. In order to compare forces with virtually any condition (flow velocity and density) and geometries, non-dimensioned coefficients are used, as descripted on the following equations:

$$C_D = \frac{Drag}{\frac{1}{2}\rho U_0^2 A} \tag{2.1}$$

$$C_L = \frac{Lift}{\frac{1}{2}\rho U_0^2 A} \tag{2.2}$$

where ρ is the air density, U_0 is the freestream velocity and A is a reference area.

Those forces are composed by pressure and shear efforts. For bluffy bodies such as a car, the main source of those efforts is the pressure difference created when the air contours such form. An important parameter to describe this phenomenon is the pressure coefficient, C_P, which measures the relation between a static pressure differential and the freestream dynamic pressure:

$$C_P = \frac{P - P_0}{\frac{1}{2}\rho U_0^2} \tag{2.3}$$

where P is local pressure and P_0 is pressure on the freestream. For incompressible flow, $C_p > 0$ indicates that flow is slower than U_0 and $C_p < 0$ means that local flow is faster than freestream and $C_P = 1$ represents a stagnation point. This parameter is largely used in experimental context because of simple application (use of pressure tabs on model's surfaces).

The complete description of any fluid dynamics problem has to account for viscous effects. It touches the dynamic of boundary layer detachments and turbulence structures formation. The quantification of those effects is accounted by the Reynolds number, a non-dimensional that compares inertial and viscous effects:

$$\mathrm{Re} = \frac{\rho U_0 L}{\mu} \tag{2.4}$$

where L is a reference dimension and μ is the dynamic viscosity of the flow. In automotive aerodynamics, reference dimension and surface are vehicle's length and frontal area, respectively.

Other important non-dimensional on the analysis of bluff bodies dynamics is the Strouhal number, that correlates vortex shedding frequency and freestream flow velocity:

$$\mathrm{St} = \frac{fL}{U_0} \tag{2.5}$$

where f is the vortex shedding frequency; and L is the reference dimension (models height for bluff bodies).

Efforts created due to vortex are remarkably influenced by viscosity and also a source of drag. Being highly tridimensional, streamwise vortexes and many smaller structures are

common around cars (HUCHO, 1987), as illustrated on Figure 2.1. The dynamics of vortexes on rear portion of the vehicle is of great interest and has been largely discussed. The use of simplified geometry, such as the Ahmed body, continues to be an important contribution to the comprehension of those structures and optimization of the automobiles aerodynamics.

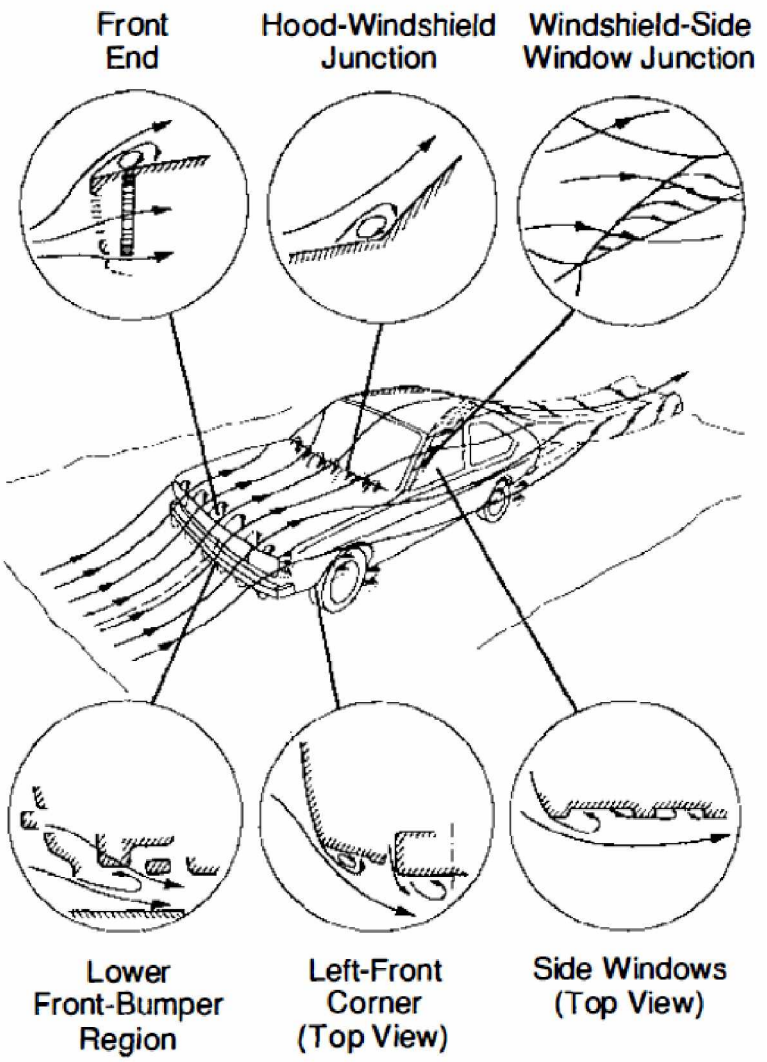

Figure 2.1- Flow around a car and major locations of flow separation (HUCHO; SOVRAN, 1993).

In this perspective, the use of a simplified pickup geometry is proposed on this work. To complement the notions of automotive aerodynamics, a general description present on the literature of flow for this particular type of vehicle is presented next.

2.2. Pickup aerodynamics

Ground vehicles aerodynamics is complex due to the influence of flow from the bottom, top and laterals of the body. The study of pickups has a differential caused by the presence of the open trunk that is impacted simultaneously by all three and its singular components.

The following description and the remaining discussions on this document are going to be presented according to the nomenclature proposed on Figure 2.2. Frontal part of the vehicle is the front end. The underbody is composed by the front overhang (region between front end and frontal wheelbase) and the rear overhang (between rear wheelbase and the end of the pickup). The cab is defined as the upper parts of the vehicle: hood, front-windshield and cabin superior surface. The defined trunk considers the rear surface of the cabin (cabin back surface); the trunk's interior (bed) and laterals walls and the tailgate. Reference dimension are the pickup overall length (L), the bed length (l) and the tailgate height (h).

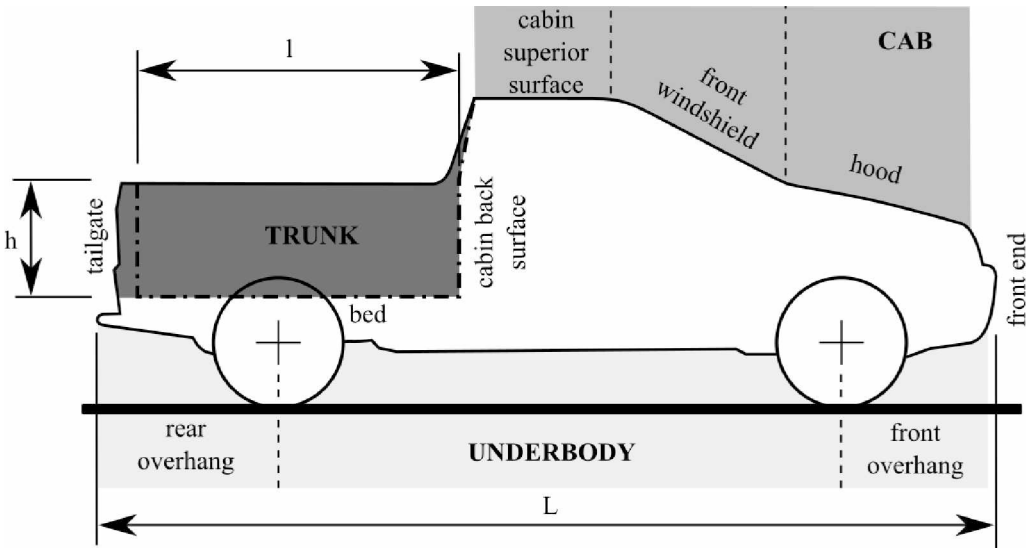

Figure 2.2 - Proposed nomenclature for pick-up parts.

The following description is based on results of Al-Garni et al. (2003, 2008, 2010) that experimentally investigated the flow around a simplified pickup using pressure tabs and PIV. The proposed geometry (Figure 2.3) and the found results are recurrent on the literature. Also, very similar flow topologies were obtained with different geometries (MOKHTAR; BRITCHER; CAMP, 2009 and HA; OBAYASHI; KOHAMA, 2009, for example).

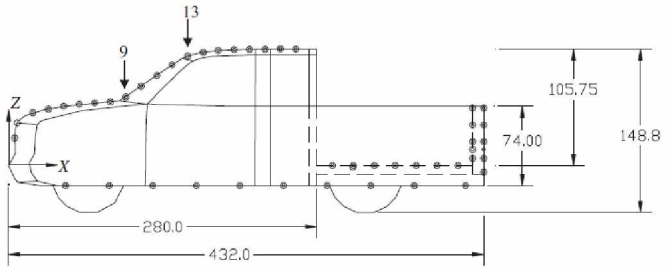

Figure 2.3 - Generic pickup model proposed by Al-Garni; Bernal; Khalighi (2003).

Results of the pressure measured on the model's symmetry plane are presented as the C_P evolution graph on Figure 2.4. There is a stagnation region on the front end of the vehicle followed by a slight acceleration until the frontal tip of hood. Flow decelerates until the joint with the frontal windshield, where it achieves a velocity minimum; next it is reaccelerated until a global C_P minimum on cab, gradually pressure coefficient is reduced until cabin back surface. On bed, all points present a depression. The acceleration of flow caused by the constriction under the vehicles creates a depression on the complete underbody.

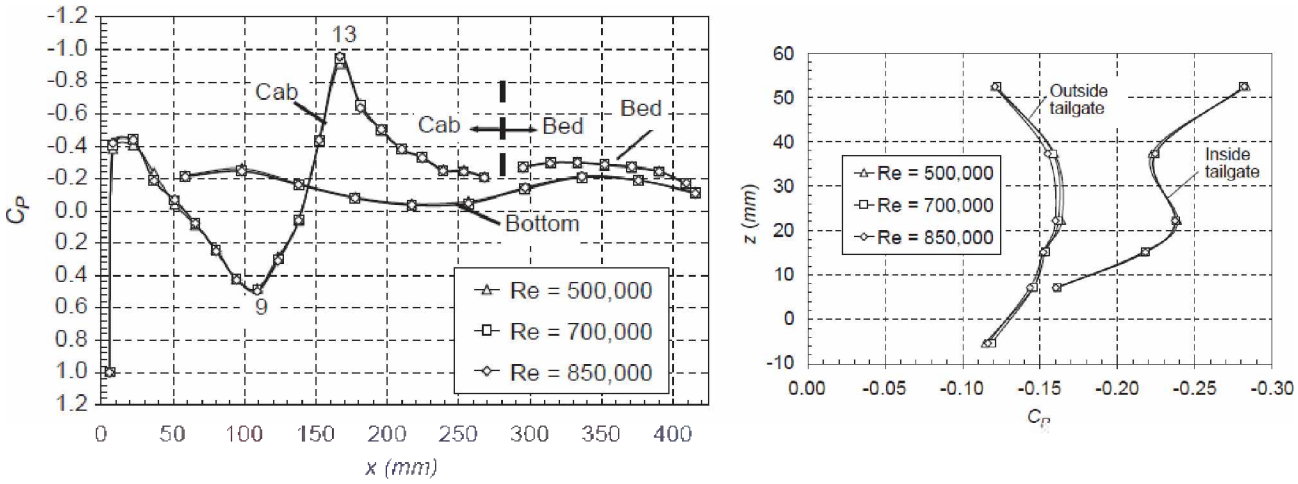

Figure 2.4 – Mean pressure coefficient distribution along the symmetry plane on the pickup truck (AL-GARNI; BERNAL 2010).

Inside the trunk there is a large recirculation zone formed by a main bubble with air deviated from the cabin's roof. Flow from the trunks lateral also deviates to the bed due to the depression, and important vortical structures are formed inside and outside the trunk. Flow that

is deviated from the recirculation bubble contacts the outside of the tailgate. On each lateral, counter rotating vortexes are formed by air from laterals and flow leaving the trunk, creating a downwash at the symmetry plane. Vortexes are also created at the end of cabin's roof.

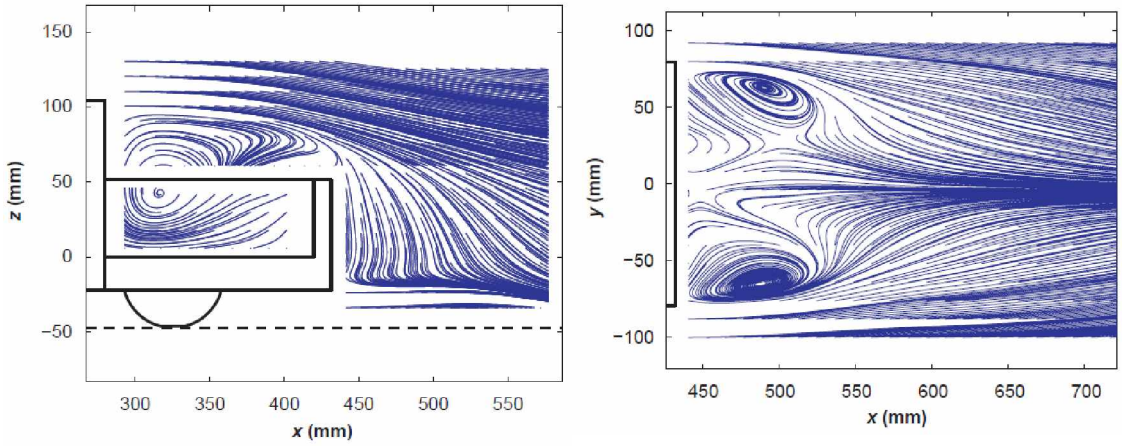

Figure 2.5 - Streamlines of the mean velocity field in the symmetry plane of the wake (left) and on the horizontal plane at z = 15 mm behind tailgate (right) of pickup truck (AL-GARNI; BERNAL 2010).

On back of trunk, pressure is proven to be smaller on the internal surface of the tailgate due to the pressure recovery promoted by the cited downwash. Therefore, a reduction of drag is associated with tailgate up configuration (COOPER, 2004). The results are summarized on the proposed vortex system on Figure 2.6.

Similar effects were obtained by Mokhtar; Britcher; Camp (2009) with a different geometry. A main recirculation bubble on trunk, vortexes on the sides of tailgate exterior and cab, downwash on tailgate are present; C_P distribution on symmetry plane is also very similar. Globally, flow follows the topology proposed by Al-Garni and Bernal (2010), as seen on the iso velocity surface representation of the wake (Figure 2.7).

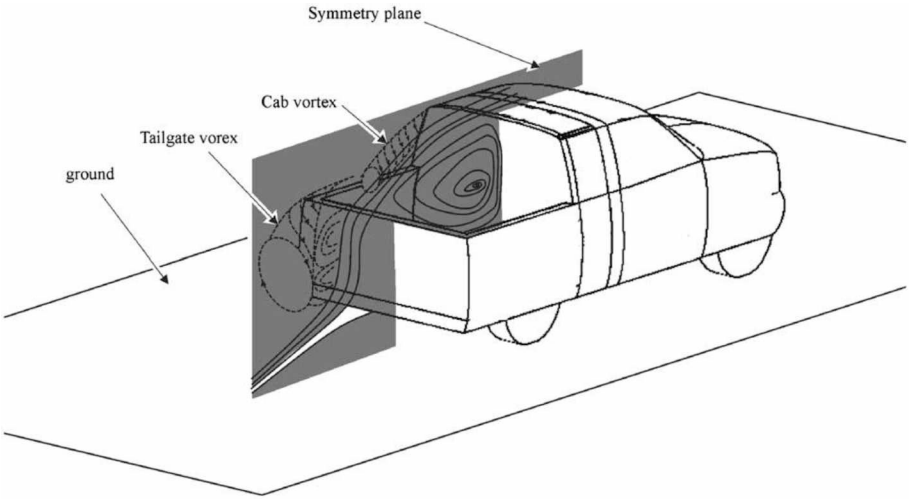

Figure 2.6 - Proposed vortex system of the flow around a pickup (AL-GARNI; BERNAL 2010).

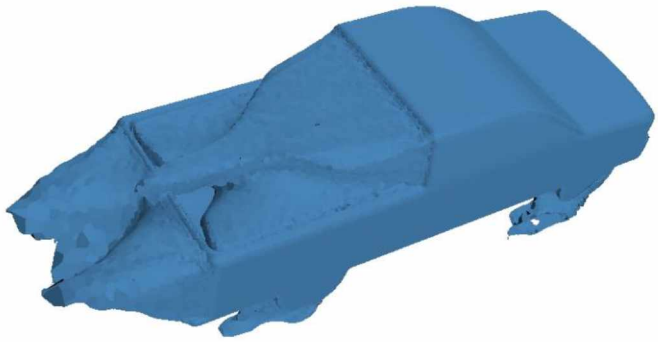

Figure 2.7 - Wake shape behind a pickup truck (MOKHTAR; BRITCHER; CAMP, 2009).

In terms of drag force, pickups are known to present higher drag coefficients than SUV's (HOLLOWAY et al. 2009). According to Chen and Khalighi (2015) 70% of the drag is due to pressure difference between front and rear of the pickup. An interest in predicting and reducing this restraining force is noticed on the literature.

Figure 2.8 presents the maximum and minimum C_D values encountered on some of the publications that are presented on bibliographic review (chapter 3). Most of the papers are aimed to study drag reduction techniques, objective that justifies the significant variation. Also, used test articles are not the same.

Besides the existence of such works, the presence of academic publications on this matter remains small. Numerical and experimental standards and methodologies are yet to be defined and specific versions of pickups have to be investigated. This work proposes the description of a light pickup, most common commercial vehicles on Brazilian automotive market. The numerous geometrical variables associated with a pickup have been proven to have complex effects on flow behavior and drag characteristics when varied. The use of simplified model strictly based on light models is aimed to question the geometry influence and to serve as a reference on future works.

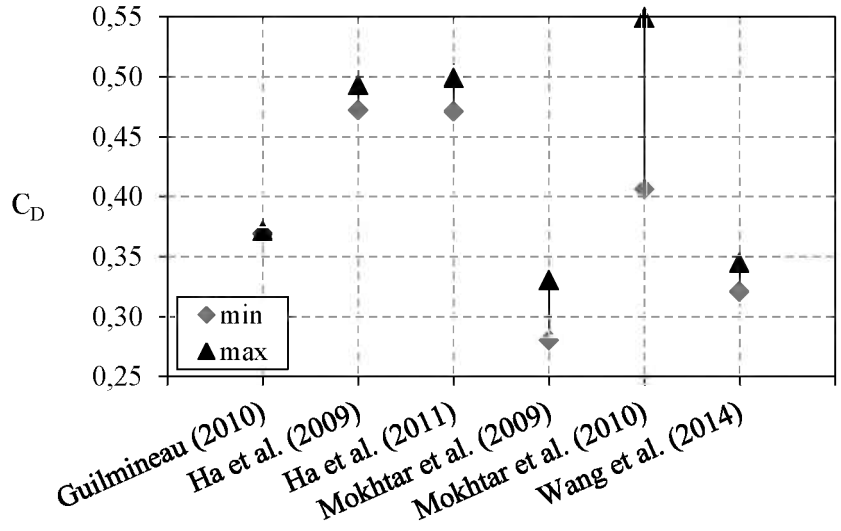

Figure 2.8 – Pickup drag coefficient range described on the literature.

CHAPTER III

Bibliographic review

The study of flow around pickups has been mostly performed in industrial context; therefore there are a small number of open articles on the subject. Even though, a general description can be found and a clear increase of related papers on the last decade is perceived.

The interest in aerodynamically optimize pickups is a longtime concern of the industry. Butz et al. (1987) performed a complete analysis for the development of the 1988 Chevrolet Pickup. A parametric study with ten geometric parameters (such as box length and height and ground clearance) was performed experimentally in a 1/4 scale modular clay model, in a total of 197 configurations. Refrigeration of the engine was considered in wind tunnel testing and acoustic tests were performed with an anechoic model. The effect of the tonneau cover was also discussed for a full tonneau cover and half tonneau, both contributed to the decrease of the drag but the last one was more efficient. Compared to the previous model, the 1987 Chevrolet Pickup, 8% drag and 5dB noise reductions are achieved. A total increase of 0.8 miles per gallon in efficiency was observed, where 75% is a consequence of the aerodynamic improvements.

In a more recent work, Wang et al (2014) used steady CFD analysis. Four design variables (bed length; bed height; cabin height and; ground clearance) were manipulated to achieve the smallest drag coefficient. It was proven that those parameters cannot be isolated in order to reduce drag what confirms the tridimensional aspect of the flow. Only ground clearance showed linear relation and relatively independence to the other variables for the proposed design space. A general conclusion was that a longer bed results in smaller drag. The optimized model has a C_D of 0.3163 (9.7% smaller than the original model); the contribution of the tailgate is not observed for the optimum bed geometry, however the increase of pressure inside bed (after cabin) results in a total drag reduction.

Furthermore, optimization routines were also performed for aerodynamic add-ons, such as the use of bumps on the rear of the cabin (MOUSSA; FISCHER; YADAV, 2015). The variables were the number and the dimensions of the proposed device equally distributed on cabin roof in the pursuit of a smallest drag. All the analyses were performed with average Reynolds equations (RANS) solver and a reduction of 10% of the drag coefficient was observed. The authors believe that the downward caused by the bumps reduced the strength of the wake thus there was an increase in pressure coefficients in the external face of tailgate.

The use of add-ons to reduce aerodynamic drag is a relatively cheap solution and can be easily design to not affect the functionality of the vehicle. Ha; Jeong; Obayashi (2011) studied the effects of a downward flap on the cab of the cabin. Numerical RANS simulation was performed and wind tunnel testing with a load cell for drag measurement, hot wire anemometer for acquiring the power spectrum density at the tailgate and oil paint on the upper surface of the tailgate for friction lines visualization. The use of the flap resulted in a displacement of the attachment point in the bed, causing more downwash inside the bed, thus reducing the wake strength and consequently the drag force. Another effect was the increase of the pressure coefficient at the cabin back, also contributing to the C_D reduction. The best results were observed for a 12° angle of the flap, with a drag reduction of 5.6% for CFD and 3.6% on experiments.

In 2014, Moussa et al. used the same concept of Ha; Jeong; Obayashi (2011) on a different pickup geometry and performed an optimization of the length and the angle of the flap using global and bounded Nelder-Mead Algorithm. Although using a different model, with completely different bed dimensions, the smallest C_D was achieved with the same 12° downward angle of the flap, and a similar behavior was noted for pressure distribution at the cabin back.

Another example is the numerical study of Chen and Khalighi (2015) of three drag reduction devices in a realistic pickup model: boat tail-like extended plates attached to the tailgate; mid-plate attached to the mid-section of the tailgate and; flat plates partially covering the truck bed. All simulations were performed in commercial software FLUENT with a 24 million of elements mesh. The add-ons are formed by non-thickness plates, that is only surfaces with wall conditions. For the 24 tested configurations, the best result (a reduction of 0,021 in C_D) was achieved with the partial cover and the top plat on tailgate. The changes in both the outside of the tailgate and at the rear surface of the cabin provoqued a decrease of pressure on the inner surface of the tailgate resulting in the drag reduction.

In a mix of add-ons and geometric modifications, Mokhtar et al. (2011) performed a study of two aerodynamic enhancements: a tailgate spoiler and a tapered roof. Numerical simulation is performed for both add-ons and for a generic pickup model using RANS approach. A drag reduction was seen for the two devices; however, the tapered roof was the most effective. A link between the flow behavior and the forces coefficients is observed, the reduction of the recirculation in the wake is related to drag reduction. The speed of the flow changed the degree of contribution of the tested enhancements.

An important aspect of the flow around a pickup is the bed. Many studies are aimed to understand and enhance the phenomenology related to it and find the best configuration in terms of drag reduction. Mokhtar; Britcher; Camp. (2009) tested numerically and experimentally four bed configurations (flat bed, tailgate-off, tailgate down and tailgate-up) in different velocities and yaw angles. The flow behavior was proven to be a function of the walls and boundaries seen in the bed, and the pressure distribution related to those topologies plays a major role in its drag characteristics. The best results were for the flat bed, however for the remaining models (more realistic for the purpose of the vehicle) the tailgate-up is the configuration with the smallest drag.

The same results are seen in the literature relating the smaller pressure in the bed when compared to the values after the force created by this pressure difference is opposite to the flow direction, thus is assumed to decrease the drag.

Conclusion on the influence of speed is also performed. No major differences are seen in flow behavior and a small increase in the drag coefficient is observed. For the yaw angle, the increase is also related to the drag increase. For both parameters, changing the configuration modifies the susceptibility of the force coefficients.

Another contribution of Mokhtar and Camp (2010) was the analysis of the box configuration influence in the drag. For three configurations (open-box, tonneau cover and cap), numerical RANS simulation were performed. For the front of the vehicle (before trunk), there are no variations of the flow. The tonneau cover resulted in a smaller and weaker wake due to the smaller recirculation in bed. For the cap, the wake is larger and even with no separation in cap, a bigger drag is observed.

Ha; Obayashi; Kohama (2009) discussed the influence of the bed geometry (height and length) in the drag characteristic of a generic pickup truck via numerical and experimental approaches. Both dimensions are proven to influence in flow topology, resulting in different

combinations of bed flow, reverse flow in wake. The smallest drag coefficient is achieved for the short and long bed, geometry in which there is no separation between the recirculation in bed and the tailgate flow. The same behavior is encountered by Al-Garni; Bernal; Khalighi (2003).

A major contribution to the academic study of pickups was made by Al-Garni and Bernal (2003, 2008, 2010). For a proposed generic model, scale 1/12, PIV and pressure measurements (steady and unsteady were performed in wind tunnel for a complete description of flow behavior. The proposed vortex system consists of small counter rotating cab vortex and two bigger structures created at the tailgate. Those two elements create an attachment of the flow in the tailgate, producing a pressure difference between the inner bed and outer bed regions helping to reduce drag, as observed by Cooper (2004). The Reynolds influence on the pressure distribution is considered negligible. Theirs results were used for simulation validation and techniques testing in later works.

Jindal; Khalighi; Iaccarino (2005), performed a RANS analysis of the flow around the model proposed by Al-Garni, using immersive body approach, local grid refinement and adaptive mesh refinement. The domain used for the simulation mimics wind-tunnel boundary condition (no-slip walls) and is formed by 2.1×10^6 cells. The same behavior for the streamlines and velocities distribution is observed, most significant variation are seen in the underbody and at tailgate vicinity. Limitations of the turbulence method, unsteady effects and the poor refinement of the mesh under the vehicle are pointed as possible sources. The drag coefficient for the simulation showed a 6% deviation from the experimental value.

A study of turbulence models was performed by Holloway; Leylek; York (2009). The calculation setup is based on RANS for 3 different turbulence models: k-ε; EVU (unsteady simulation); and SDSM (semi-deterministic stress model). All simulations presented simultaneously very similar results and significant deviations when compared to the wind tunnel values. The authors suggest that the unsteadiness of the problem is not well represented in an averaged approach and even macroscopic parameters such as the drag coefficient are not well predicted.

Using the same geometry, Guilmineau (2010) performed a numerical analysis for two turbulence models: Explicit Algebraic Reynolds Stress Model (EARSM), and Detached Eddy Simulation (DES). The domain is a replica of the wind tunnel setup and the solver is ISIS-CFD, with the incompressible unsteady Reynolds-averaged Navier Stokes equations (URANS). The complete pickup is simulated, with a total of 16.6 million of cells. The obtained results are very

close to the experimental values for the velocity and correlation profiles, the same behavior is achieved for the pressure distribution and flow topology. The friction lines are presented and a recirculation in the base of the windshield was notices. Both turbulence models gave similar results, that way the use of EARSM turbulence model is proven more advantageous for its smaller CPU time. A study scale is suggested.

For a more simplified model, Lee and Parameswaran (2006) performed a transient analysis with the k-ε turbulence model under the Launder-Kato modification. The mesh was produced in ICEM CFD HEXA, no slip condition is assumed for all the walls. No quantitative data is presented, only velocity contours for the symmetry plane and in the truck bed. The flow behavior is reasonable compared to the results presented in literature; however the small amount of data is not representative for more conclusions.

The use of simplified geometry in order to understand the major structures is much disseminated in automotive aerodynamics, being the Ahmed body one expressive example. The same trend can also be seen for pickup inspired geometries. Agelin-Chaab (2014) performed experimental analysis of a 2D bluff-body inspired by pickup trucks geometry. The experiments were made on a water tunnel for different ground clearances and "bed" lengths and heights, PIV and proper orthogonal decomposition (POD) was performed. The description of the flow is similar to the results of Al-Garni (2003) for the 3D generic pickup analysis; however the tri-dimensionality of the flow must be taken in account for that analysis. For the tested model, the contribution of the small scale structures (higher order modes) was proven to be the most significant.

For the present work, the study is also based in a simplified pickup model with realistic dimensions based on light pickups of the Brazilian market. A general flow description is presented numerically and experimentally and a study of the influence of the mesh prismatic layer, model geometry, flow velocity and experiment scale is presented.

CHAPTER IV

Methodology

This chapter is designated for the presentation and definition of the proposed pickup model, and the numerical and experimental setups used on this study.

4.1. Test Article

In order to have a geometry that characterized real vehicles, the used geometry is based upon the most typical models in the light pickups market in Brazil. Table 4.1 presents the number of licensing for this category in July 2014. For the six most licensed models, the Hafei Mini is not considered due to its peculiar geometry; Peugeot Hoggar and Ford Courier are no longer produced, however there are still representative in the fleet.

Table 4.1 – Brazilian Light pickups licensing in July 2014 (FENABRAVE, 2014).

POS.	MODEL	JULY	MARKET JULY	JUNE	MARKET JUNE
1°	Fiat STRADA	12 585	56,28%	10 559	53,78%
2°	Volkswagen SAVEIRO	7 294	32,62%	6 721	34,23%
3°	Chevrolet MONTANA	2 446	10,94%	2 319	11,81%
4°	PEUGEOT HOGGAR	23	0,10%	23	0,12%
5°	HAFEI MINI	11	0,05%	13	0,07%
6°	Ford COURIER	1	0,00%	-	0,00%
	TOTAL	22 360	100,00%	19 635	100,00%

Figure 4.1 presents the photographs of the five considered models. The simplest version of 2016 was considered for all the models (and the latest available for the Peugeot Hoggar and

the Ford Courier). It's observed that the geometrical variations between versions of the same vehicle are small and possible mistakes regarding the considered variety are negligible.

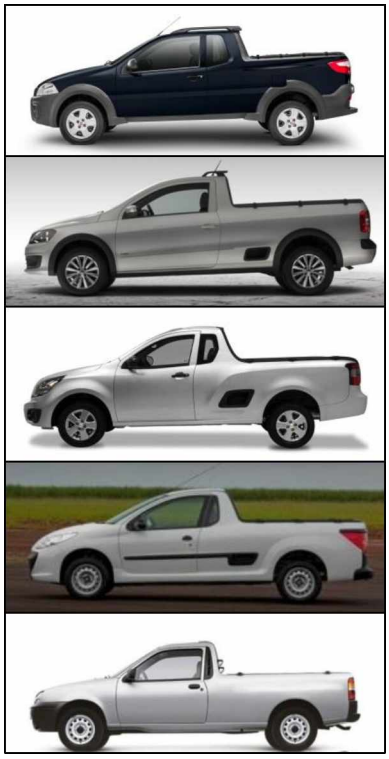

Figure 4.1 – Reference pickup vehicles.

Total of 26 external dimensions are obtained from manufactures website, customer manuals and from photographs analyzing using the software ImageJ. For the image processing, one known dimension (total length or total width) is used to set the scale of the photo in pixels/mm and the scale is confirmed for another known dimension (total height). A total of 10 images encountered on manufacturer's websites and publications on specialized media were used: two for the Fiat Strada; two for the Volkswagen Saveiro; one for the Chevrolet Montana; three for the Peugeot Hoggar; and two for the Ford Courier. A mean error of 4.5% is observed for all the scale tests. The acquired dimensions are presented on Figure 4.2 and Table 4.2.

All the dimensions are defined for at least one of the reference vehicles and the proposed model is defined only from those dimensions. Grey cells represent values obtained via image analyzing and red values are the ones corresponding to previous versions of the pickup. Empty cells are dimensions that could not be defined for all the proposed methodologies. The

overall length of the bed of the Ford Courier was not considered due to its discrepancy of the values presented for other models.

Table 4.2 – Pickup models dimensions

		MODEL				
LABEL	**DESCRIPTION**	**Fiat STRADA**	**VW SAVEIRO**	**Chevrolet MONTANA**	**Peugeot HOGGAR**	**Ford COURIER**
A	track front [mm]	1,425		1,429		1,550.124
B	track-rear [mm]	1,390	1,490.71	1,439	1,396.631	
C	windshield front height [mm]	1,094.033			995.319	1,078.657
D1	overall height [mm]	1,402.433	1,550	1,578	1,524	1,477
D2	overall height (with cab rack) [mm]	1,525	1,497	1,630	1,577.886	
E	ground clearance [mm]	170	231.381	264.286	203.052	265.281
F	hood front height [mm]	839.401		861.571	877.176	821.207
G1	overall width [mm]	1,664	1,708	1,700	1,668	1,793
G2	overall width (with mirrors) [mm]	1,906	1,893	1,918		2,020.399
H	cabin lateral angle [deg]	62.152	66.371		57.995	62.808
I	hood angle [deg]	11.725	9.951	10.305	12.799	9.039
J1	approach angle [deg]	25.849	32.59	24.109	20.925	25.769
J2	departure angle [deg]	26.743	27.77	25.322	21.915	25.755
K	windshield angle [deg]	31.858	30.669	30.196	29.403	31.855
L	rear of cabin angle [deg]	23.039	12.45	23.374	27.512	9.866
M	front overhang [mm]	790	744.893	844	792.59	679.998
N	wheelbase [mm]	2,718	2,750	2,669	2,745	2,893.417
O	rear overhang [mm]	901	872.091	1,001	883.325	884.271
P	overall lenght [mm]	4,409	4,493	4,514	4,526	4,457
Q1	box height [mm]	1,249.249	1,228.855	1,195.558	1,143.976	1,058.722
Q2	box interior height [mm]			525		464
R	box lenght [mm]	1,685	1,615.461	1,737.357	1,706.814	1,760.316
S	width between wheelhouses [mm]	1,090	920	1,119		1,100
T1	box interior width [mm]		1,230	1,340		1,240
T2	box width [mm]	1,350				
V	overral lenght at box [mm]		1,640	1,680		1,816+

LEGEND

1,000	data from manufacturer and specialized publications
1,000	data from images analysing
1,000	dimension of previous models

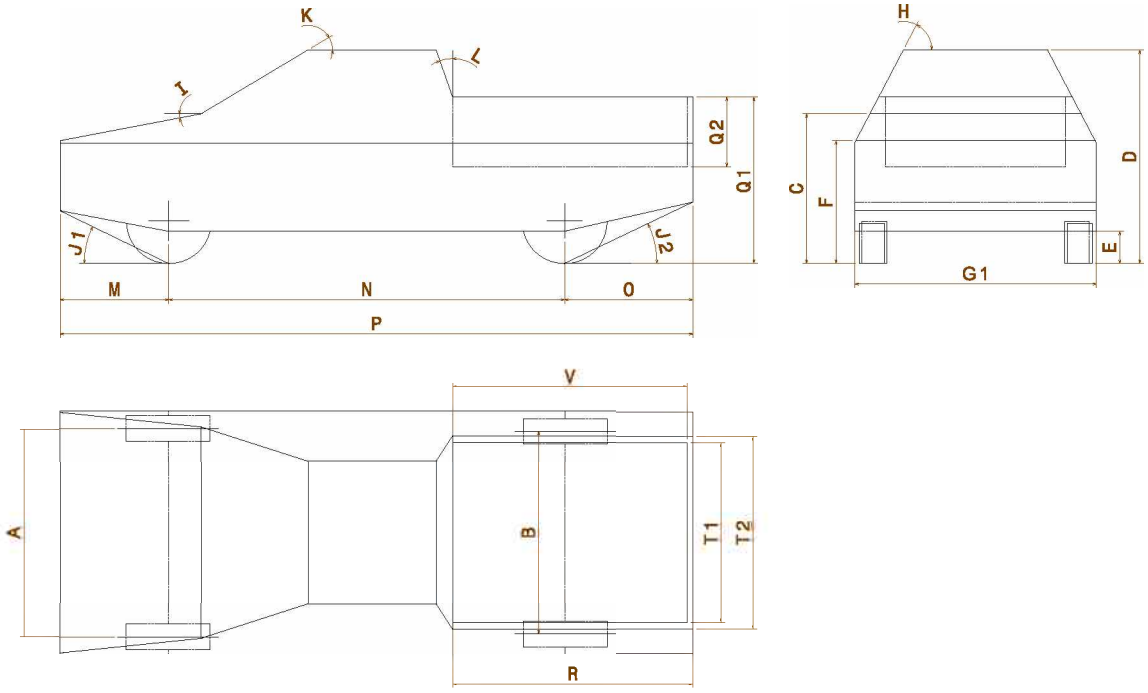

Figure 4.2 – Test article composing dimensions.

To achieve an understanding of the general flow around a pickup, the model is simplified: no air inlets or outlets are modeled; underbody is simplified; there are no rear viewers, wheels housing or any attachments in the model, thus dimensions labelled as ‘D2’, ‘G2’ and ‘S’ are not considered on this study. The simplified design (sharp edges and plan surfaces) does not reproduces any of the original vehicles; however the use of a more generic body is aimed to clarified macroscopic effects seen in outside flow of a pickup, especially in bed, and ignores the design choices of the manufactures.

For each dimension, a simple mean operation is applied in order to achieve a geometry that represents in general the pickups on the road; values are presented on Table 4.3. The maximum and minimum values of the dimensions and the standard deviation and coefficient of variation are also presented. As seen in Ha; Obayashi; Kohama (2009), the bed geometry plays a key factor in the produced aerodynamic structures and consequently in the drag of the vehicle, the use of five references could represent a more global geometry with could be seen as more illustrative.

The small variation of the measured dimensions confirms the similarity and validates the use of a simplified model in the proposed aerodynamic study. The biggest fluctuations are

observed for the angular values and are due to the difficult of the image analyzing, especially for the rear of cabin angle (L). The geometry of the wheels is based on the standard tire of four of the reference pickups: the 175/70 R14 (18 cm wide and external diameter of 60 cm).

Table 4.3 – Statistics of dimensions analysis.

LABEL	MAXIMUN	MINIMUN	MEAN	STANDARD DEVIATION	COEF. OF VARIATION
A	1,550.12	1,425.00	1,468.04	71.11	4.8%
B	1,490.71	1,390.00	1,429.09	46.46	3.3%
C	1,094.03	995.32	1,056.00	53.11	5.0%
D1	1,578.00	1,402.43	1,506.29	68.94	4.6%
D2	1,630.00	1,497.00	1,557.47	58.85	3.8%
E	265.28	170.00	226.80	40.92	18.0%
F	877.18	821.21	849.84	24.59	2.9%
G1	1,793.00	1,664.00	1,706.60	52.00	3.0%
G2	2,020.40	1,893.00	1,934.35	58.27	3,0%
H	66.37	58.00	62.33	3.43	5.5%
I	12.80	9.04	10.76	1.49	13.9%
J1	32.59	20.93	25.85	4.26	16.5%
J2	27.77	21.92	25.50	2.22	8,7%
K	31.86	29.40	30.80	1.07	3.5%
L	27.51	9.87	19.25	7.65	39.7%
M	844.00	680.00	770.30	61.47	8.0%
N	2,893.42	2,669.00	2,755.08	83.74	3.0%
O	1,001.00	872.09	908.34	52.82	5.8%
P	4,526.00	4,409.00	4,479.80	47.46	1.1%
Q1	1,249.25	1,058.72	1,175.27	76.35	6.5%
Q2	525.00	464.00	494.50	43.13	8.7%
R	1,760.32	1,615.46	1,700.99	55.78	3.3%
S	1,119.00	920.00	1,057.25	92.29	8.7%
T1	1,340.00	1,230.00	1,270.00	60.83	4.8%
T2	1,350.00	1,350.00	1,350.00	-	-
V	1,680.00	1,640.00	1,660.00	28.28	1.7%

The contact of the wheel with the ground is modeled by a chamfer that removed 1% of the diameter parallel to the ground. This modification is closer to reality than the line contact present if the wheels were completely round and more reasonable for later process of meshing and CFD calculation.

The overall dimensions are of the same magnitude of previous works, as presented in Table 4.4, however specific dimensions (such as bed height and length) and the proportions of the models are not the same and comparisons between results must be made with care in regard of those differences. In order to achieve a convenient blockage factor on experimental testing, 5 % according to Hucho (1987), 1/10 scale is adopted. The model presents 205.58 cm^2 of frontal area that equals a blockage ratio of 5.71 % on wind tunnel.

Table 4.4 - Overall dimensions and blockage ratio of generic pickup models in the literature.

	MODEL	Al-Garni (2003)	Ha (2009)	Mokhtar* (2010)	Lee (2006)
lenght [mm]	447.98	432	407.4-528.6	5,300	432
height [mm]	150.63	148.8	167	1,900	123
width [mm]	170.66	152	183.5	1,780	152
frontal area [m^2]	0.0206	0.019	-	2.545	-
blockage ratio	5.71 %	6%	-	0.78 %	-

*numerical simulation

The model is designed in the software CATIA V5R20 using the dimensions presented on Table 4.3 and the cited tire diameter. The model is made entirely composed by sharp edges and flat surfaces; the three views plan is presented on Appendix I. Later on this work it is referenced as “baseline”. In order to comprehend the effects of the sharp edges, a second version of the model (“rounded” version) is prepared by adding a fillet of 15 mm on all the external edges and a fillet of 6 mm on the exterior of the bed; the bed interior is the same for the baseline model. Both models are illustrated on Figure 4.3.

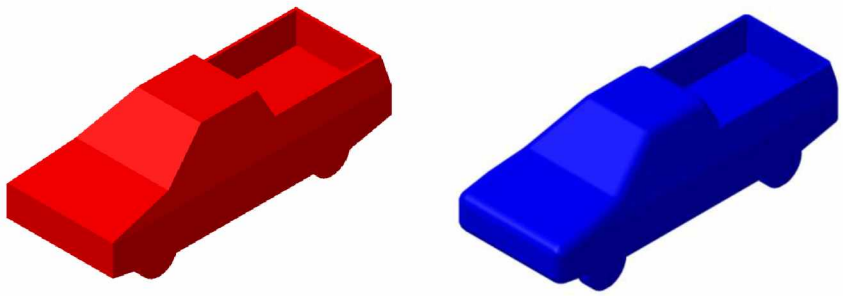

Figure 4.3 – Pickup models: baseline (left) and rounded (right).

4.2. Numerical

4.2.1. Numerical Domain and Mesh

The mesh is prepared in software ANSYS ICEM CFD 16.0, meshing software that allows the use of CAD exported geometry from multiple software; capable of structured and unstructured meshing; and to export them for a number of solvers such as ANSYS FLUENT; Star-CCM+, CFD++ and OpenFOAM. The relative high controllability of shell and volumetric elements parameters allows the creation of sophisticated domain discretization.

The complete domain surfaces (model and boundaries) are prepared on CATIA using both generic pickups presented on section 4.1. The files must be converted to an older file format of CATIA (.MODEL, from CATIA V4) in order to be imported on ICEM CFD.

The numerical domain dimensions are based on the car length L and follow the proportions used by Ha; Jeong; Obayashi (2011). As summarized on Figure 4.4, the inlet is placed forward the model at a distance of 10L, the outlet is located 20L downstream the model, the superior limit of the domain is at 10L (instead of 30L) of the ground and the lateral limit is placed after 7.5L the model. Only half of the model is simulated with 0.06 % blockage ratio.

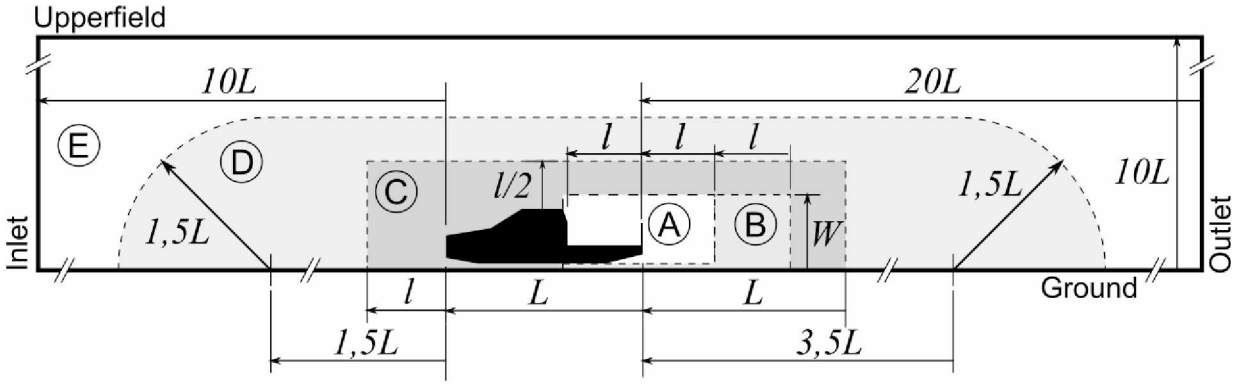

Figure 4.4 – Refinement regions on symmetry plan (L is the pickup length; l is the trunk length; and W is the pickup width)

For better accuracy for flow representation, the elements of the mesh are refined in specific regions, especially in the trunk and in the wake. Six volumetric regions, defined by the software as “densities”, are used to delimit the size of the elements in representative regions and are listed next.

- trunk density: element size of 2 mm, corresponds to the trunk and the closer portion of the wake. It starts at the end of the rear surface of the cabin; therefore it is bigger for the rounded geometry. Labelled as (A) on diagram;
- wake density: element size of 5 mm, comprehends both the later wake and the underbody of the model; (B) on diagram;
- inner density: size of 10 mm, englobes all the pickup and affects both before and after the model; (C) on diagram;
- outer density: size of 40 mm, an expansion of the previous density; (D) on diagram.
- wheel density: variable size, minimum of 0,5 mm on the contact with the ground; one for each wheel, not represented in the diagram.

On the rest of the domain – represented as (E) - the element size is defined as the length of the pickup (447 mm).

Wheels and trunk surface mesh is defined using the blocking feature of the software for triangular elements and are illustrated on Figure 4.5. The pre-mesh is later converted for unstructured mesh.

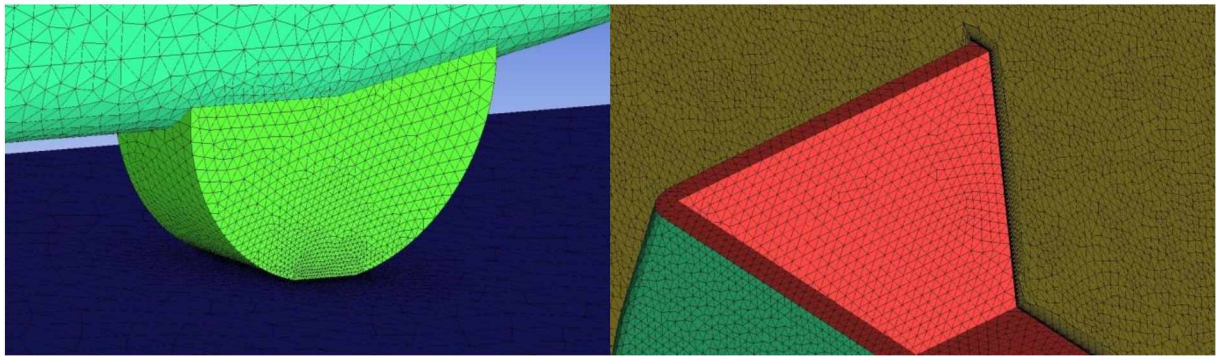

Figure 4.5 - Surface mesh of wheel (right) and trunk (left).

A total of three final meshes (corresponding to the two tested geometries) are used in all numerical simulations. In order to evaluate the influence of the boundary layer in the results, the study of the baseline model is made initially with mesh composed only by tetrahedrical elements (later on this work this mesh is referenced as TETRA); later simulations were performed with the same geometry with a 4 mm high prismatic boundary (20 layers with exponential grown, first

layer is 0.05 mm height - y+ ≈ 3.5 for Schlichting skin-friction formula, U_0 = 25 m/s) on the ground and on the vehicle (labelled BASELINE); mesh is redone for a better numerical convergence (in order to reduce shrunken and distorted pyramidal elements), however all the domain definitions presented on Figure 4.4 are maintained to grant a reasonable comparison between results. The same study was intended to be performed for the rounded geometry, but numerical convergence was not reached for the mesh with no prismatic boundary and all preliminary results are not presented. Thus, the ROUNDED mesh contains also tetra and prismatic elements (same size and distribution cited previously).

The main refinement regions and the boundary elements are depicted on Figure 4.6, with represents the surface mesh on the symmetry plane and the pickup model for the three meshes.

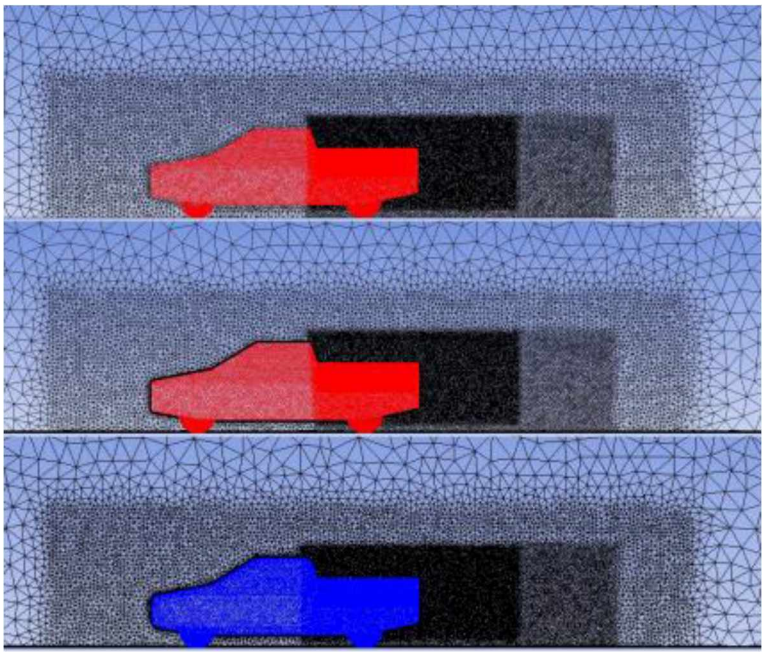

Figure 4.6 – Numerical surface mesh on symmetry plane and pickup (from top to bottom: TETRA, BASELINE and ROUNDED).

The meshes present an average of 8 million elements. Previous works used for RANS simulations: Mokhtar; Britcher; Camp (2009), 700 thousand, and Moussa; Fischer; Yadav (2015), 3 million cells, for half domain (symmetry); Guilmineau (2010), 16.6 millions, Ha; Jeong; Obayashi (2011), 3 million, Holloway; Leylek; York (2009), 26 million, and Chen and Khalighi (2015), 39 million, for the complete vehicle. In comparison to previous work and due to the main

focus of describing the mean flow structures, meshes are considered reasonable, especially for the available computational capacity.

The tested flow velocities (16.67 m/s; 25 m/s and 33.33 m/s) are constrained to wind tunnel performance and correspond (in terms of Reynolds number) to a very slow pickup speed (6 to 12 km/h). For the chosen scale, dynamic correlation is achieved for a ten times bigger velocity (166.7 to 333.3 m/s) within would consist in an important Mach value and level of compressibility.

To question the validity of the use of in scale model for the description of the flow around the real size pickup, both the baseline and the rounded model are tested at the same freestream velocity with an enlarged geometry: a simple scale transform is performed for the mesh, extending the size of the elements for a factor of 10 in all three directions, maintaining for each individual case (TETRA, BASELINE and ROUNDED) the same elements geometry and distribution.

4.2.2. Boundary Conditions and Solver

All the numerical analyses are performed using the steady Reynolds Averaged Navier Stokes equation (RANS) in commercial software STAR-CCM+, distributed by CD Adapco Inc.

The turbulence model is SST k-ω, proposed by Menter in 1994, with the standard coefficients. It presents good behavior in adverse pressure gradients and separating flow conditions (HA; JEONG; OBAYASHI, 2011). Solution is based on the segregated flow model (2nd order upwind convection scheme), with all y+ wall treatment. Fluid is incompressible air (standard properties: 1.18415 kg/m^3 density and 1.85508×10^{-5} Pa.s dynamic viscosity); reference pressure is also let on standard (P = 101,325 kPa).

In order to mimic wind tunnel set-up, the ground is fixed and wheels are also static, both surfaces with non-slip condition. The far field (both upper field and side field) is defined as walls with slip condition. Inlet presents constant velocity (16.667; 25.000; 33.333 m/s), turbulent intensity is set to 1% and the turbulent velocity scale is fixed at 10% of the free stream velocity. Turbulence viscosity ratio is fixed as 10. Outlet is defined as a pressure outlet of 0 Pa (barometric). Pickup is completely stationary, composed by non-slip surfaces.

For the proposed discussions, a total of 18 simulations are performed, considering: three freestream velocities; three meshes (corresponding to the two geometries) and two scales (full size and in scale), as summarized on Table 4.5.

Table 4.5 - Simulations Matrix.

	MODEL	baseline				rounded	
	MESH	TETRA		BASELINE		ROUNDED	
	SIZE	Full	Scale	Full	Scale	Full	Scale
U_0 [m/s]	16.667	x	x	x	x	x	x
	25.000	x	x	x	x	x	x
	33.333	x	x	x	x	x	x

The CFD calculations are done in a workstation with an Intel Core i7-3930K (3.20 GHz) processor with twelve cores (six physical) and 48.0 GB RAM memory. For the presented meshes, mean iteration time is of 12 seconds when all cores are used.

Simulations for the in scale baseline model are redone with wind tunnel air properties for validation.

4.3. Experimental setup

This section presents all experimental assets and techniques used on this work.

4.3.1. Wind tunnel Facility and Model

The facility is an open wind tunnel with a test section of 60 x 60 cm of the External Aerodynamics Research Center (CPAERO) of the Federal University of Uberlândia, presented on Figure 4.7. Flow momentum is created by a rotor of 12 blades driven by a 25 HP electrical engine on the upstream of the wind tunnel. Air velocity is driven by an electrical inverter (output from 0 to 60 Hz).

It is instrumented with pressure tabs and an analogic manometer. A Pitot tube and a digital manometer can also be used for calibration.

Figure 4.7 - Wind tunnel facility.

In order to perform the experiments presented on this work, improvements were made on the wind tunnel. The concerning results and general wind tunnel flow description procedures are presented on Appendix II.

The baseline model is printed using a MakerBot 3D printer, model Replicator 2x, with an ABS filament of 1.5 mm diameter. The geometry is prepared under the same CATIA model that generated the meshes for CFD analysis, thus the chamfer in wheels is also present. The generation of STL files (for the printer) follows the standard exportation parameters and the tessellation is prepared on printer manufacturer's software (MakerBot Desktop). Due to limitations regarding the printer size, the model is printed in four parts, as presented in Figure 4.8. Printer resolution is 0.5 mm and the level of infill density is 10%.

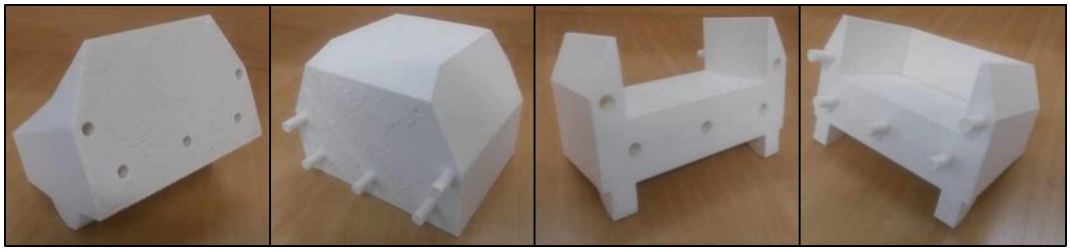

Figure 4.8 – Pickup model parts.

Superficial texture and distortions observed on the largest pieces required later preparation for assembling the parts and smoothing the external surfaces and the contacts. The finalized model, presented on Figure 4.9, is painted black to achieve better contrast on the qualitative flow visualization tests.

Figure 4.9 - Finalized pickup model.

The model is fixed directly on the ground of the wind tunnel test section. Influences of the existing boundary layer, inexistent for real life vehicles once the air is stationary, are considered irrelevant.

4.3.2. Quantitative method - Hot-wire Anemometry

This technique uses the magnitude of heat that is transferred from a thin wire to a passing flow in order to measure it speed. Electric current is applied to the wire, generating electrical power (P) proportional to the current magnitude (I) and the wire resistance (R_w): $P = I^2R_w$. Once temperature of the wire is steady, it means that the amount of energy given to the wire equals what is being dissipated to the flow, thus, convective energy is measured. With access to the voltage difference that created the current, we are able to the monitor the amount energy.

Dissipated energy via convection can be related to the flow velocity using a power law correlation for the Nusselt non-dimensional number. The following equation was proposed by King on 1914, known as King's law:

$$I^2R_w^2 = E^2 = (T_w - T_0)(A + BU^n) \tag{4.1}$$

where E is the voltage; T_w is wire temperature; T_0 is a reference temperature; U is the velocity of the flow and A, B and n are coefficients obtained on calibration. With measured voltages, those coefficients can be obtained using equipment such as a Pitot tube or another hot-wire anemometer system placed at the same flow or a calibration nozzle.

Measured voltages are commonly related to flow velocity using two different equations presented next:

- Power law (based on King's law):

$$U = \left(\frac{E_c^2}{B} - A\right)^{\frac{1}{n}} \tag{4.2}$$

- 4^{th} degree polynomial equation:

$$U = C_0 + C_1E_c + C_2E_c^2 + C_3E_c^3 + C_3E_c^4 \tag{4.3}$$

where A, B, n, and C_0 to C_5 are the calibration constants and E_c is a corrected voltage.

Being this method based on convection, it's susceptible to all properties that are related to this heat change mechanism such as temperature variations (errors of approximately 2% per

Celsius degree change) and fluid compressibility. When low speeds are considered, natural convection also influences. More details on the technique itself can be seen on DANTEC documentation (JØRGENSEN, 2004), where this short description is based.

Important features of the flow can be analyzed using the signals obtained with hot wire anemometry. Besides mean velocity, U_0, two interesting parameters when describing turbulence can be derived: the standard deviation of the velocity, U_{RMS}, and the turbulence intensity, I_{turb} (its adimensionalized version). All formulations are presented on following equation:

$$U_0 = \frac{1}{N}\sum_{i=1}^{N} U_i \; ; \quad U_{RMS} = \left(\frac{1}{N-1}\sum_{i=1}^{N}(U_i - U_0)^2\right)^{1/2} \; ; \quad I_{turb} = \frac{U_{RMS}}{U_0} \tag{4.4}$$

where U_i is a acquired velocity; and N is the total number of acquired values.

Global distribution of turbulent scales and vortex shedding frequency can be defined with spectra of the recorded signal using Fourier Transform for a discrete signal:

$$DSP(k) = \sum_{j=1}^{N} x(j)\exp(-2\pi i/N)^{(j-1)(k-1)} \tag{4.5}$$

Values can be presented in the decibels scale using a reference value (E_{ref}):

$$DPS_{dB} = 20\log_{10}\left(\frac{DSP}{E_{ref}}\right) \tag{4.6}$$

The hot-wire anemometry is used to produce velocity profiles upstream and downstream the model. All measurements are performed using DANTEC Dynamics StreamLine Pro Anemometer System. A 1D hot-wire probe (55P11) is attached to a 90° support and connected to one of the constant temperature anemometer (CTA) modules of the StreamLine Pro frame. The acquisition module is connected to a National Instruments A/D converter which sends data to the computer via a USB port. The system control and data exporting is done with the manufacturer's software, StreamWare Pro. Figure 4.10 illustrates the experimental setup.

The pickup is placed on the floor of the wind tunnel test section and the probe is positioned on three different axes at the symmetry plane of the pickup: 78 mm – bed's length l -

before the model (P1); 50 mm and 92.57 mm – approximately tailgate height h and its first multiple - after the model (P2 and P3, respectively).

Measurements of the stream wise velocity with a 1D hot-wire probe are performed for a distance of the ground from 5 mm to 170 mm, each 5 mm (total of 34 measurements points per position).

The sampling frequency is 2 kHz (acquisition period of Δt = 0,5 ms) for a total of N = 32,768 sample points (acquisition time of T = 16.383 seconds). A Pitot tube is placed on the roof of the test section and a digital manometer displays the free stream velocity. This indication is used to define global freestream flow stagnation and start anemometer acquisition.

Calibration is performed using the StreamLine Pro Automatic Calibrator for 20 velocities between 1 to 27 m/s, logarithmic spaced. Indicated pressure and temperature are P = 91.85 kPa and T_{abs} = 27.30 °C. The 4th degree polynomial function is chosen as the calibration law and temperature correction is not applied. All unmentioned parameters are set default on the acquisition software and the post processing is performed on software MATLAB.

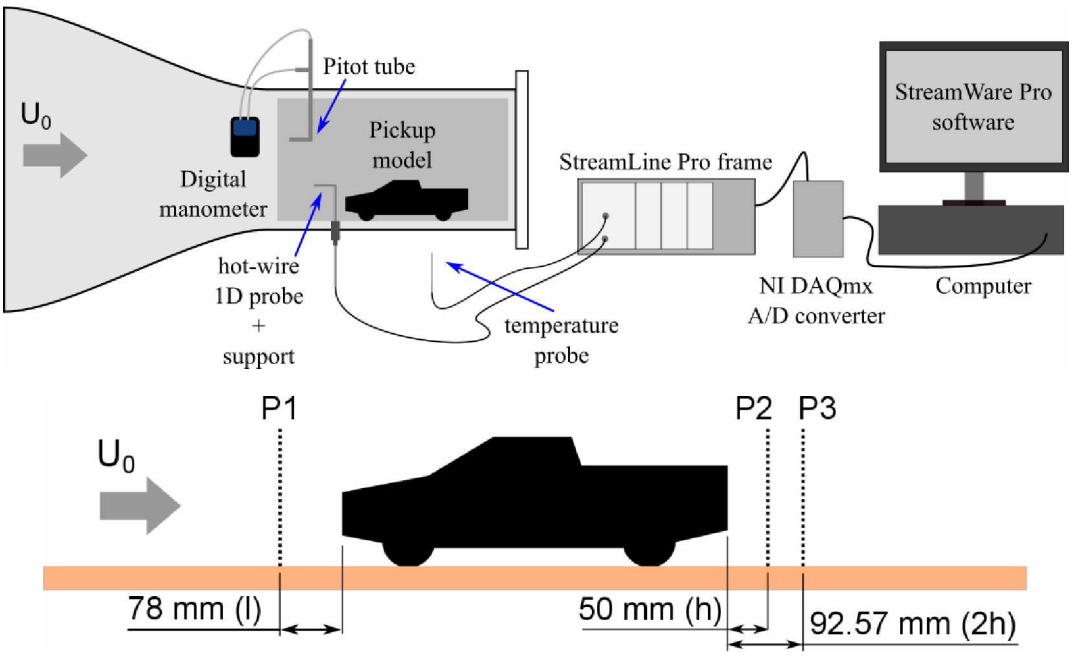

Figure 4.10 - Experimental setup.

Figure 4.11 - Experimental setup (left). On detail (right) the hot-wire support and probe on position P1 and Pitot tube on test section roof.

4.3.3. Qualitative method - Wall Tufts

In order to describe flow direction and detached/recirculation zones close to model's surface, wall tufts technique is applied. Important features of close surface flow can be easily pointed with this technique: when flow is laminar, tufts are aligned with flow direction and describe a relatively steady dynamics; on turbulent/unsteady regions, the movement of tufts is highly oscillating; zones where tufts are elevated are the ones within separated/adverse flow (MERZKIRCH, 1987). Disturbances caused by the presence of the tuffs and theirs attachments assets (tape or glue) must be accounted. This method is largely applied in both aeronautical and automotive domains (example presented on Figure 4.12).

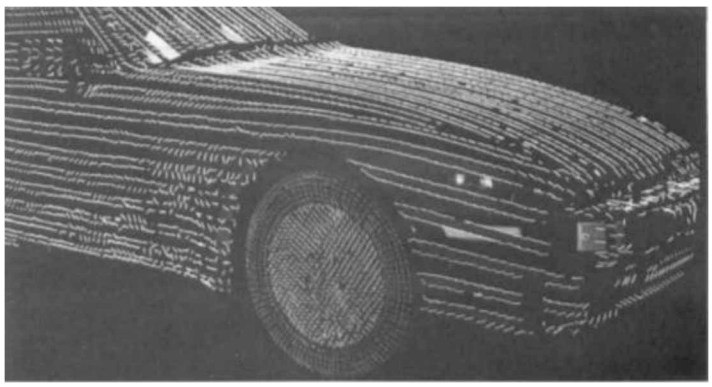

Figure 4.12 – Fluorescent minitufts on car moving at 160 km/h past stationary camera (MERZKIRCH, 1987).

For this study, 15 mm long wool tufts are attached on pickup walls. Tufts are not placed on the front end; on the underbody, only the wheels and the final part of the trunk (rear overhang) are discretized. An average distance of 5 mm is considered between the lines of tufts. Figure 4.13 presents the model with the tufts.

Figure 4.13 - Model with wool tufts.

The tests are recorded with a high definition camera posed on a tripod, as seen on Figure 4.14. The effects on the trunk are also registered from the top via a hole on test section roof using a cell phone camera. Recording are made on three flow velocities: 10.0, 16.7 and 25.0 m/s. On this document, representative frames of those videos are presented.

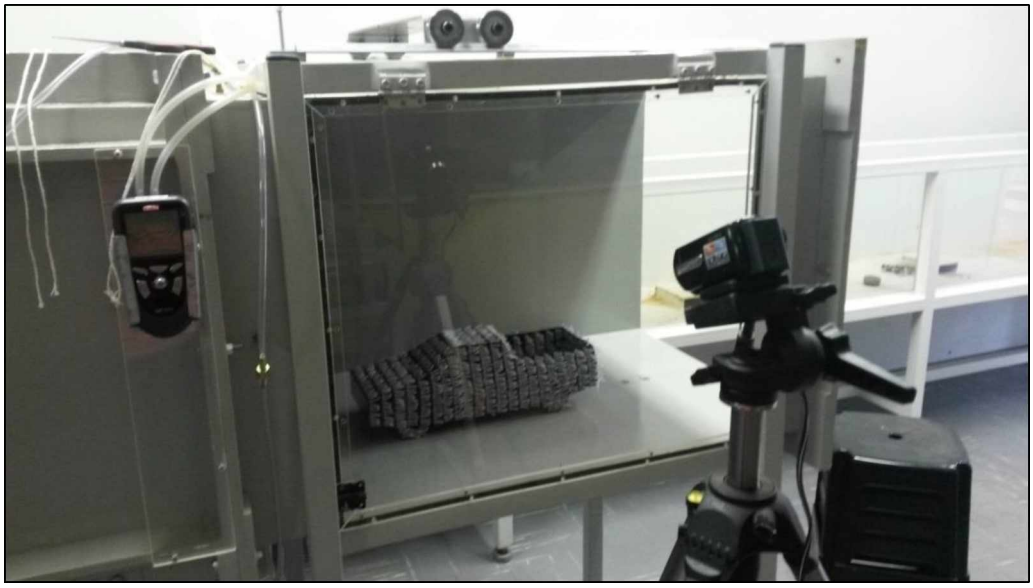

Figure 4.14 - Experimental setup for wall tufts test.

CHAPTER V

Results and Discussions

This section is dedicated to the presentation and discussion of both experimental and numerical results.

5.1. Numerical Solution Properties and Validation

First chapter is dedicated to present the simulation characteristics and the influence of boundary layer discretization for the baseline model, numerical results and the validation of CFD solution. The flow around both geometries is discussed next. Final part contains the results of the performed scale study.

5.1.1. Numerical Solution Properties

This section is dedicated to present the aspects of numerical solution and to describe the proposed convergence criteria. If not settled contrary, the results presented on this section are for the in scale model, freestream at U_0 = 25 m/s and meshes with and without prismatic boundary.

Due to the complexity of the problem and its transient behavior (HOLLOWAY et al., 2009), relatively high order residuals are achieved for all considered quantities, as seen on Figure 5.1. Also, mesh quality is highly restricted by the elements at the contacts of the wheel with the ground, especially for BASELINE mesh, leading to the existent residuals fluctuations. According to the solver's help manual, it's often recommended to ignore those instabilities; therefore other properties are considered for defining convergence.

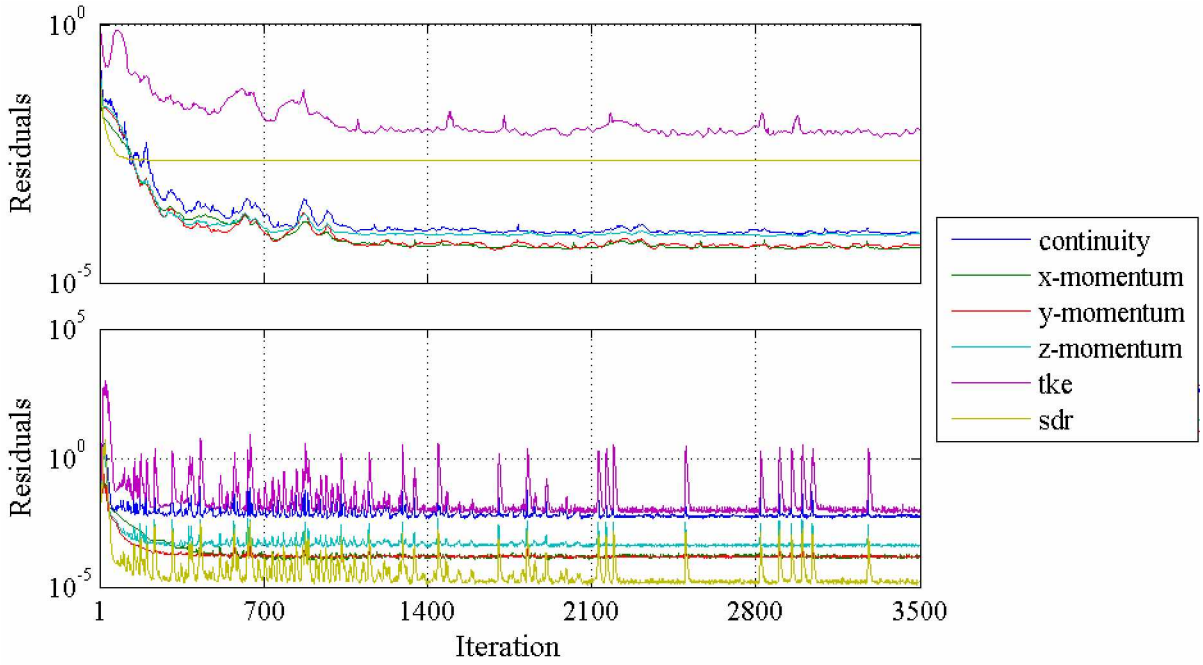

Figure 5.1 - Residuals monitor for simulation with the TETRA (top) and BASELINE (bottom) meshes (in scale, U_0 = 25 m/s).

In order to define a number of minimum iterations to obtain a representative solution, velocity field on symmetry plane and force coefficients are monitored. Figure 5.2 presents the evolution of C_D and C_L for the two meshes.

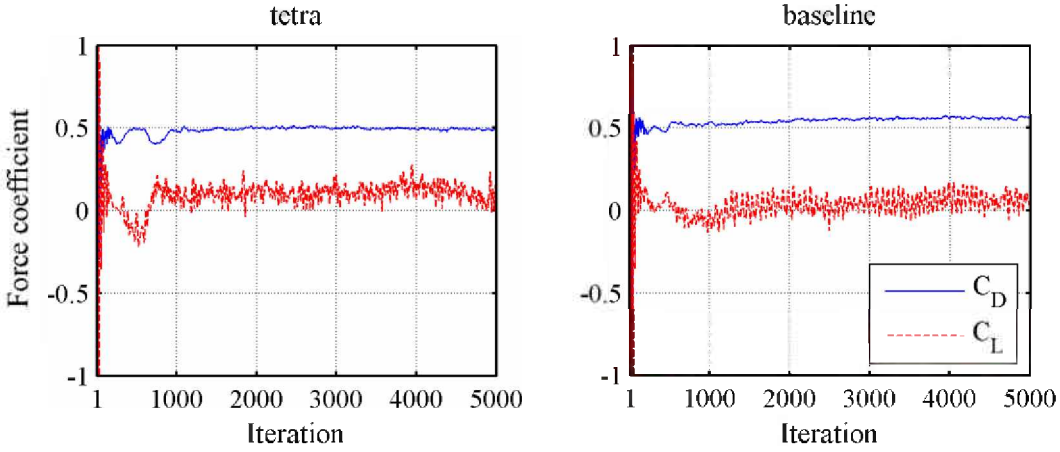

Figure 5.2 - Evolution of numerical force coefficients for in scale TETRA (left) and BASELINE (right) meshes, U_0 = 25 m/s.

Stopping criteria is defined based on drag coefficient convergence. A sequence $I = \{C_{D,i}\ ;\ i = 1,2,3,...\}$, where i represents a iteration, is statistically convergent if and only if its sequence of partial averages, μ(n), converges and its sequence of partial standard deviations, σ(n), converges to 0 (BURGIN; DUMAN, 2006). Figure 5.3 shows the evolution of the mean and standard deviation of the numerically obtained C_D sequences, starting at iteration 5. For both geometries, convergence is defined visually within 3,000 iterations.

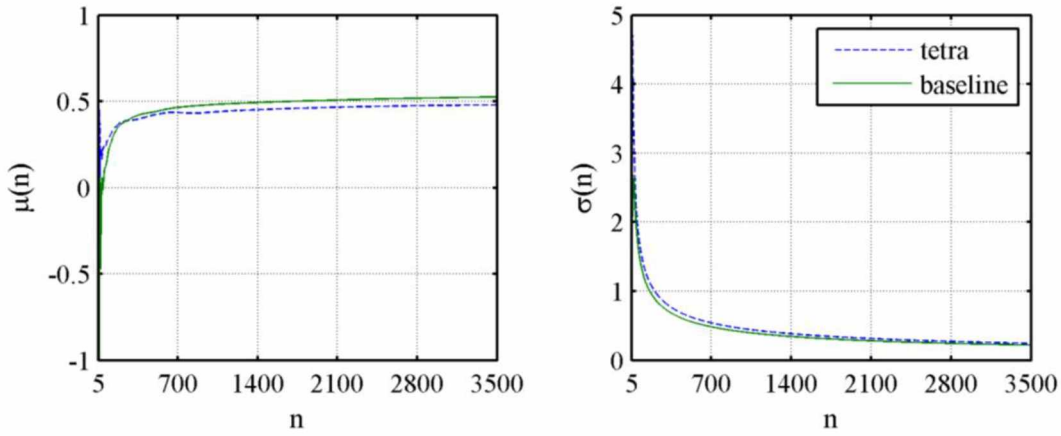

Figure 5.3 – Evolution of partial average (left) and standard deviation (right) of drag coefficient sequence for baseline and rounded in scale model, U_0 = 25 m/s.

Similar behavior is observed in all calculations and the simulations are stopped with 3,500 iterations; the additional 500 are used for force coefficients prediction. Standard deviation of the considered C_D values (from iteration 3000 to 3500) is on the order of 0.005. At the last iteration mass imbalance for the complete domain is around 1×10^{-4} %.

For the proposed number of iterations, convergence is not well defined for the lift coefficient with the TETRA mesh. According to Guilmineau (2010), poor discretization of the underbody may lead to poor C_L prediction, but this aspect alone does not invalidate the solution. For BASELINE mesh, 40 elements are added between the ground and the model (the two prismatic boundaries) and convergence is similar to the observed for drag coefficient.

The same analyses are performed for the ROUNDED mesh and the results are similar to those of the mesh with prismatic boundary. For this reason they are not presented on this document.

5.1.2. Mesh study

For the baseline model, simulations are performed for two different meshes: TETRA with no prismatic layers; and BASELINE with 4 mm boundary layer discretization. The influence of the proposed refinement is discussed next. Simulations for in scale, 25 m/s flow are used for the comparison.

Figure 5.4 presents the normalized velocity field for both meshes. The coarse mesh (TETRA) has globally a similar velocity field, with a big recirculation bubble on the trunk and above the hood. However, the poor modeling of the flow contact with the surfaces (minimum element size of 2 mm) of the geometry caused a simpler reproduction of the smaller structures and their effects. For the BASELINE mesh, the ground detachment and the shear layer on pickups underbody is more well-defined. Also, a recirculation region on front overhang and a boundary layer growth on cabin top are present and a higher wake is existent.

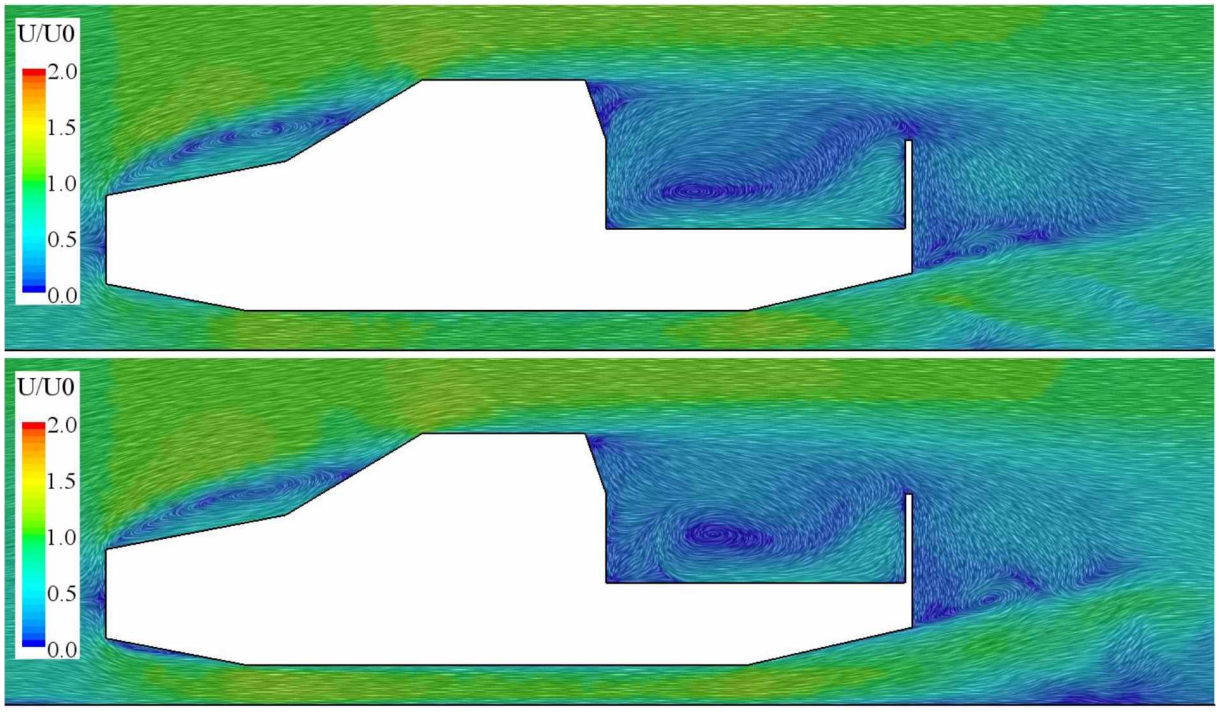

Figure 5.4 - Normalized velocity field on symmetry plane, baseline model for TETRA (top) and BASELINE (bottom) meshes (in scale, U_0 = 25 m/s).

On trunk, the use of the prismatic elements influenced the recirculation bubble size and position. Patterns that are unnoticed for the TETRA mesh solution are responsible for pushing

the recirculation center downstream, as showed on Figure 5.5. The detachment on trunk is placed at 24% of bed's length for the refined mesh and at 2% of *l* for the TETRA mesh. The smaller vortexes formed on lower exterior part of tailgate are numerically instable and vary in position and shape for a relatively low number of iterations and cannot be accountable for comparing the meshes.

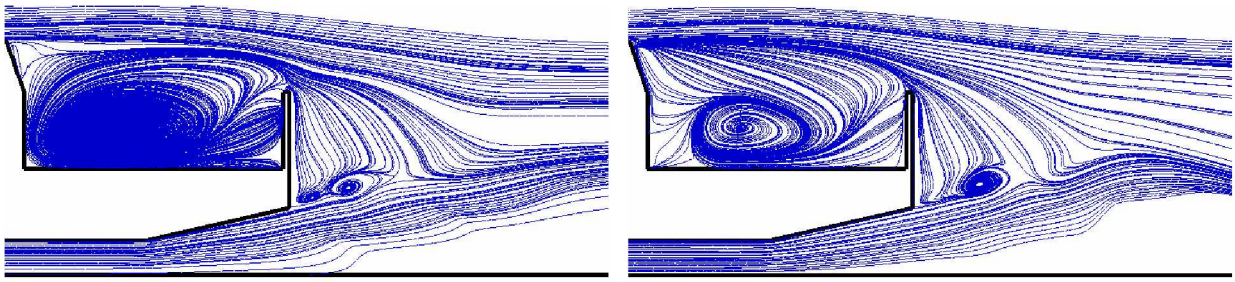

Figure 5.5 - Streamline on symmetry plane for TETRA (left) and BASELINE (right) mesh (in scale, U_0 = 25 m/s).

Inside the trunk, a different behavior is present. Figure 5.6 has the streamlines for both meshes on the center of the trunk horizontal plane. The central recirculation is much smaller due to the presence of a more important vortex on the cabin back surface, at the center of the trunk. On wake, there are no significant changes on the streamlines distribution.

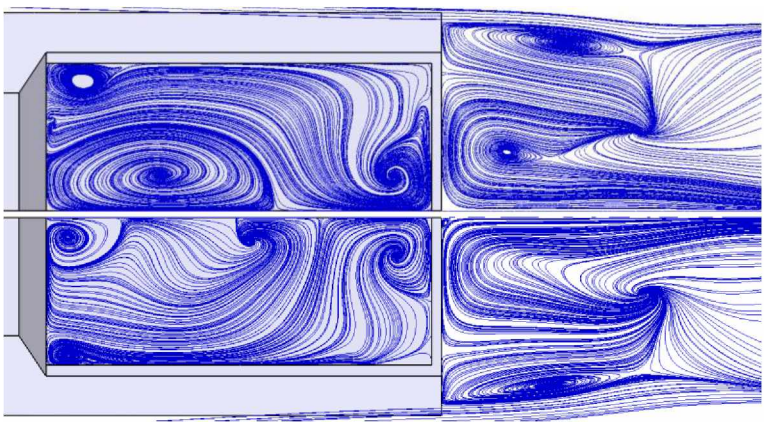

Figure 5.6 - Streamline on center of trunk for TETRA (top) and BASELINE (bottom) meshes (in scale, U_0 = 25 m/s).

Solution for the BASELINE mesh contained a more energetic wake (Figure 5.7). The vortex on cab is more developed for the chosen scale and a slower dissipation is achieved; turbulent energy is also more prominent close to the ground.

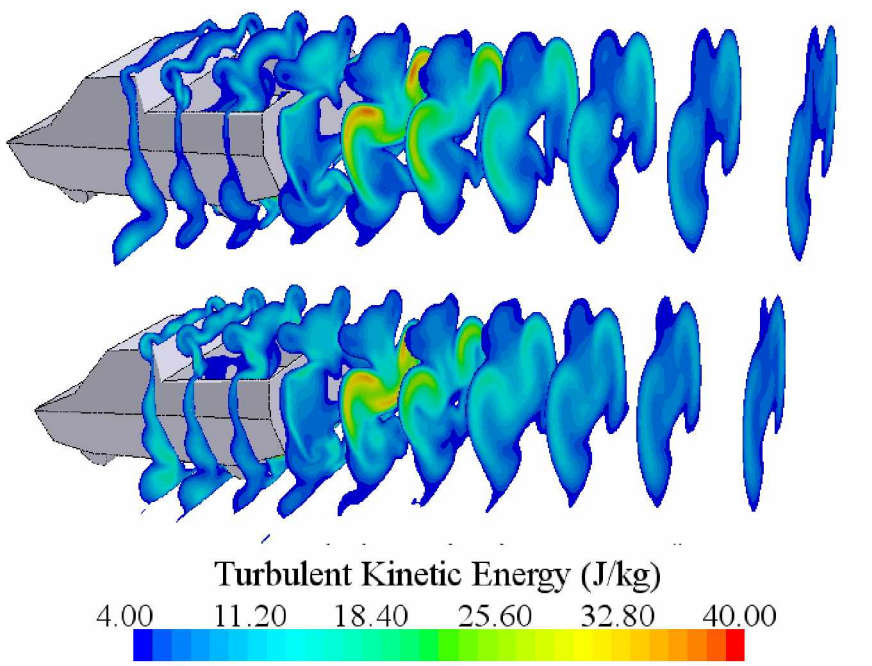

Figure 5.7 – Evolution of Turbulent Kinetic Energy on pickup trunk and wake for TETRA (top) and BASELINE mesh (bottom).

The discretization of the boundary layer caused variations of the pressure evolution on symmetry plane of the model. The differences are going to be commented on the following paragraphs and a discussion on the structures themselves is presented on the section 5.2. Results are presented following the axis system on Figure 5.8 and are adimensionalized using the model overall length (L), bed length (l) and tailgate height (h).

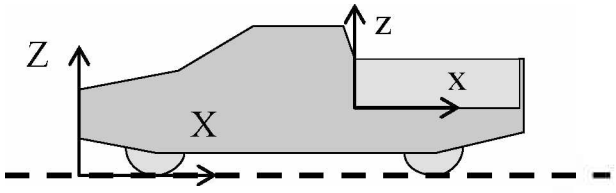

Figure 5.8 - Axis system.

Figure 5.9 presents C_P evolution for the cab, bed and underbody. For the cab, C_P graphs are very similar for both meshes and follow the same behavior observed by Al-Garni and Bernal (2010): depression on hood and cabin top and global maximum on front windshield. Comparable behavior is noted on bed, where there is a decrease of pressure until about 40% of the bed followed by an increase up to tailgate. However, for BASELINE mesh, the first 20% of bed presents a plateau of C_P = -0.2 formed by the structures located between the cabin back surface and the recirculation bubble. On underbody, there is a depression caused by the recirculation of flow on front overhang, only noted on the solution with the more refined discretization (BASELINE). A stagnation point is formed on the front end and a parabolic C_P evolution is observed for both solutions, which is not presented on graph.

Differences are more visible on the cabin back surface and the tailgate, see Figure 5.10. Phenomenology on trunk that caused the variations observed on bed also produced a higher C_P on cabin back for the TETRA mesh. On internal face of the tailgate, curve follows the same pattern and oscillations are in order of 10% (from -0.10 to -0.11). Outside tailgate, the behavior is similar for both meshes, but a C_P difference of 0.07 is observed on tailgate root. It is noted at all the parts that TETRA mesh C_P curves present oscillations, when BASELINE graphs are smooth.

All discrepancies are a reflection of the different vortex distribution obtained with the two meshes. The use of boundary description is extremely important to simulate flow detachment and turbulent flow, and the similarity between TETRA and BASELINE meshes can be associated with the existence of only sharp edges, which have a distinguish detachment point. For the rounded model, convergence could not be achieved without prismatic boundary. The use of a much refined mesh altered the topology of the flow in both the front and the back of the geometry. Thus, a study of the prismatic boundary itself is recommended.

Variations in flow behavior affected force coefficients. The differences resulted in 6.79% increase of drag coefficient: from C_D^T = 0.5034 for TETRA mesh to C_D^B = 0.5376 for BASELINE mesh. Both the values are the same in terms of distribution of drag, being 96% caused by pressure differences and only 4% by shear forces. In terms of lift coefficient, the TETRA mesh presented a much more important fluctuation (the standard deviation for last 500 predicted values reduced from 0.0432 to 0.0220), however the results are not representative when compared to commonly found on automotive aerodynamics (C_L^T = 0.0980 and C_L^B = 0.0158). Guimineau (2010) obtained lift coefficients in the order of 0.3.

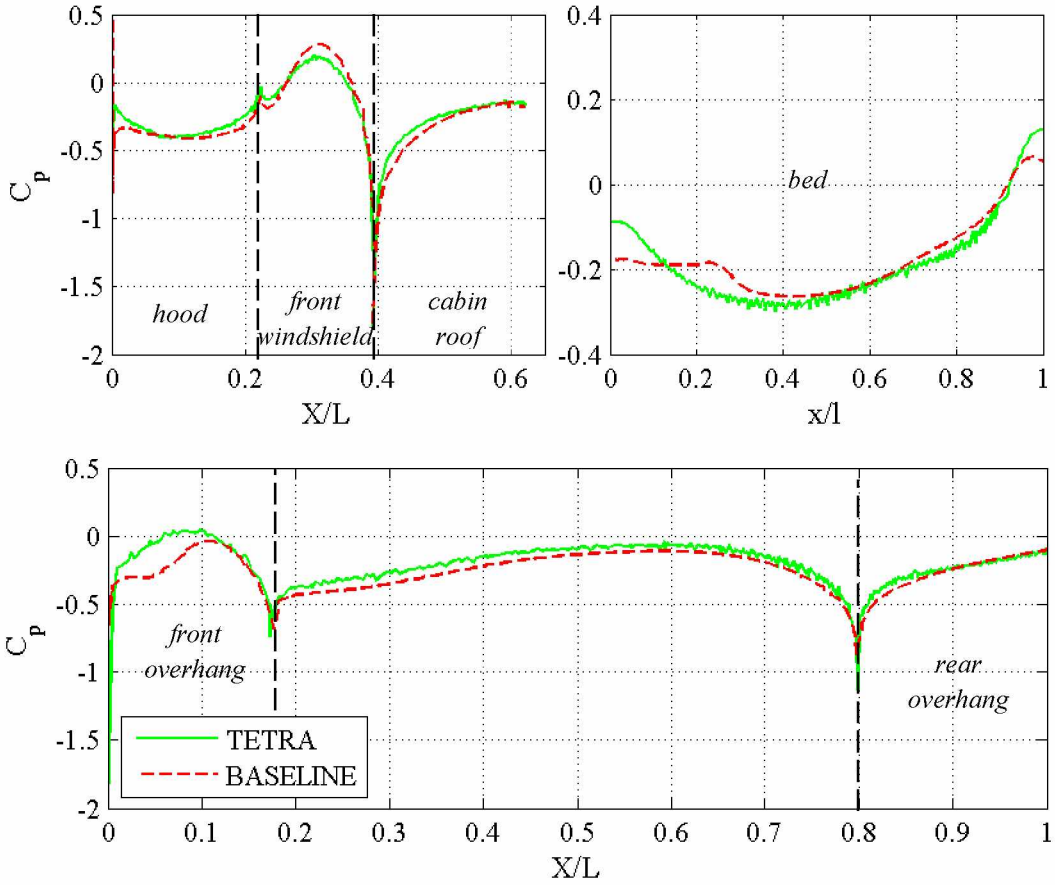

Figure 5.9 - Pressure coefficient on symmetry plane of the cab, bed and underbody for TETRA and BASELINE meshes (in scale, U_0 = 25 m/s).

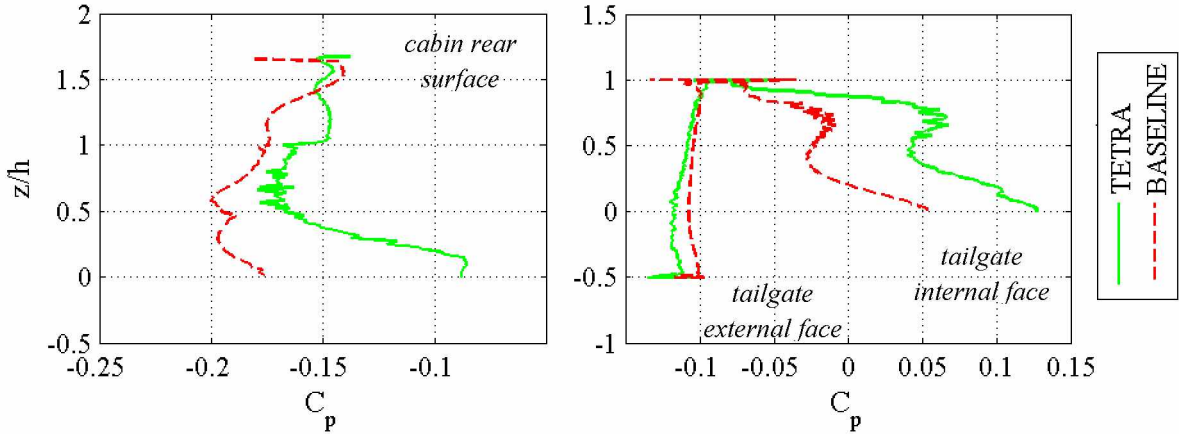

Figure 5.10 - Pressure coefficient on symmetry plane of the cabin rear surface and tailgate for TETRA and BASELINE meshes (in scale, U_0 = 25 m/s).

5.1.3. Experimental Results and Validation

Qualitative and quantitative experimental techniques are used to validate numerical computations. On this section, velocity profile and surface topology results produced on wind tunnel are presented and compared to CFD solutions for baseline geometry.

5.1.3.1. Quantitative – Velocity Profiles

Velocity profiles on symmetry plane, upstream (P1) and downstream (P2 and P3) the printed model are produced in wind tunnel with a hot-wire anemometer. Tests were performed for two freestream velocities: U_0 = 16.7 and U_0 = 25.0 m/s.

In order to perform numerical validation, simulations with TETRA and BASELINE meshes are relaunched for additional 1,000 iterations in experimental conditions: P = {91.85; 101.60} kPa, U_0 = {16.9029; 25.00} m/s; ρ = {1.055; 1.222} kg/m^3 (using perfect gas equation with average temperature between the start and the end of the data acquisition); and turbulence intensity on inlet I_{turb} = {0.8; 1.0} %. All remaining parameters are unaltered.

The numerical results are exemplified on the velocity field on Figure 5.11. The vectors are placed at the experimentally tested locations. On the first position (P1), we see the influence of the model on upstream flow. On wake (P2 and P3), boundary layer evolution, accelerated flow from underbody and sequential shear boundary are noticed.

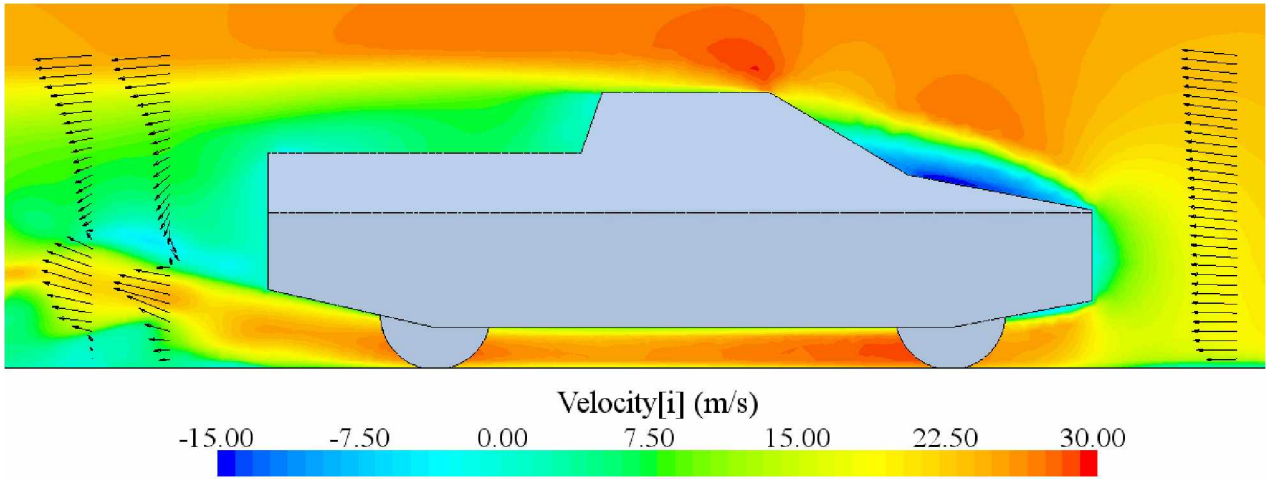

Figure 5.11 – Streamwise velocity field in symmetry plane and vectors on tested points for BASELINE mesh at wind tunnel conditions (in scale, U_0 = 25.0 m/s).

Compared to the CFD results, the same behavior is observed for the 3 positions (velocity profiles on Figure 5.12). On P1 (before the model) boundary layer is defined between 0 to 10 mm, deviation outside the boundary layer region is of the order of 1%. For P2, outside boundary layer, there is an increase of velocity until 40 mm that can be associated to underbody flow acceleration, followed by a rapid decrease. The recirculation encountered after the trunk is represented by a plateau of 6 m/s for U_0 = 16.7 m/s and 9 m/s for U_0 = 25.0 m/s from around 60 to 90 mm on the rear profiles. The wake continues until the higher point considered. At the last position, the obtained curve is the same that the one observed in the previous acquisition plane, however the structures are dislocated in position and velocity magnitude (higher and slower).

For the first profile, the 4 numerical solutions reproduced the numerical curve. On the wake, profile structure is the same: accelerated flow at Z = 40-60 mm, minimum velocity at 60-80 mm and gradual acceleration until reaching freestream velocity at last point (Z = 170 mm). However, the solutions vary above 40 mm. For BASELINE mesh, the developing boundary layer presented on section 5.1.2 is closer to the experimental results; solution with the TETRA mesh have an abrupt velocity increase that created a velocity profile very distinct from hot-wire results.

When analyzing the profiles acquired on the wake (P2 and P3), it's noticed that the experimental curves are smother and the minimum speed is around 5 m/s, despite the expected negative magnitudes on the recirculation zones. This result can be associated to the limitations of the measuring technique, once values outside the calibration region (including negative velocities) are not correctly acquired. On Figure 5.13, the limits of the acquired data are showed at each point; for the four profiles placed on the models wake, the minimum velocity for almost all points is fixed around 1 m/s (the calibration inferior limit).

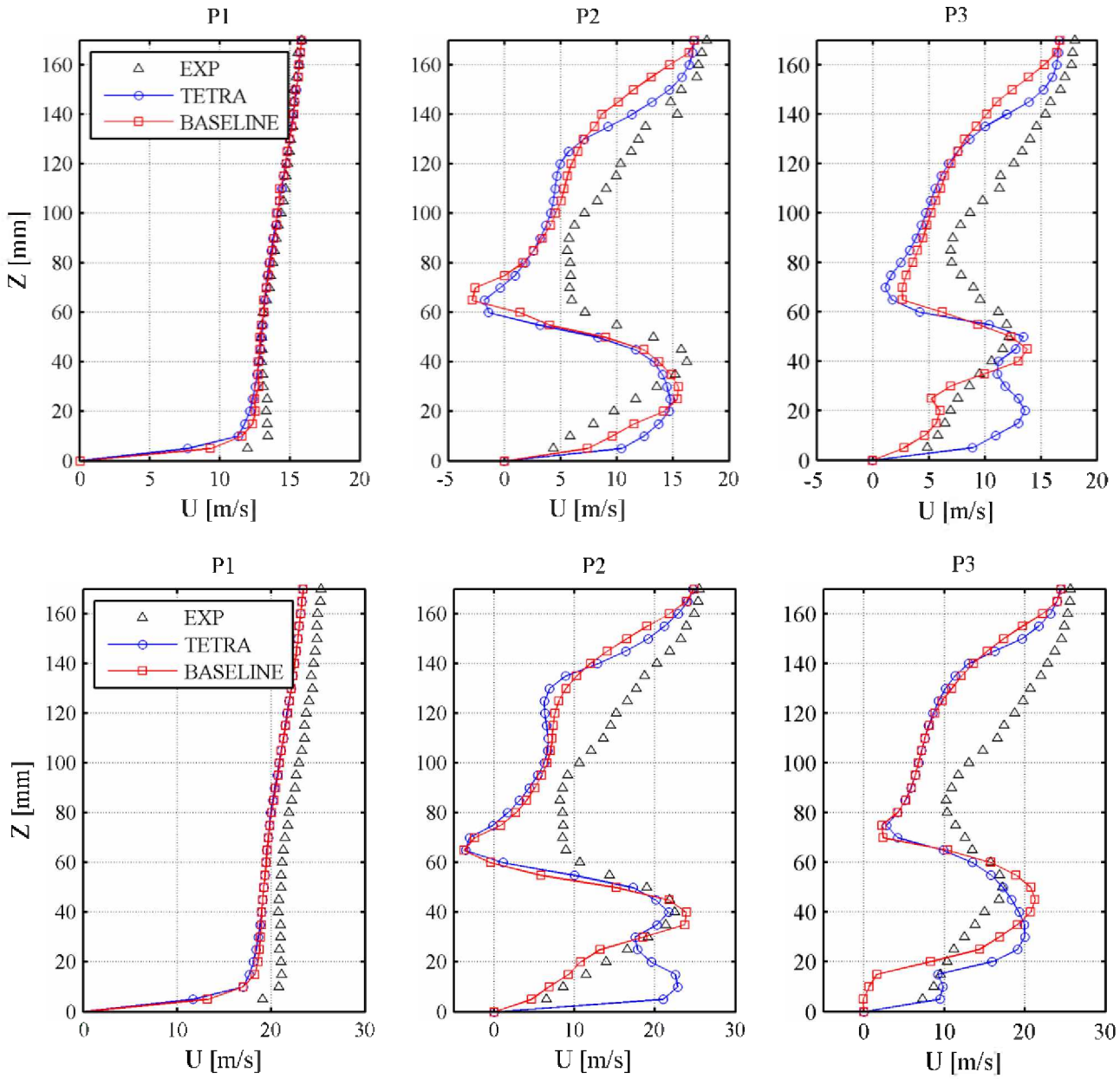

Figure 5.12 - Numerical and experimental velocity profiles at U_0 = 16.7 m/s (top) and U_0 = 25.0 m/s (bottom).

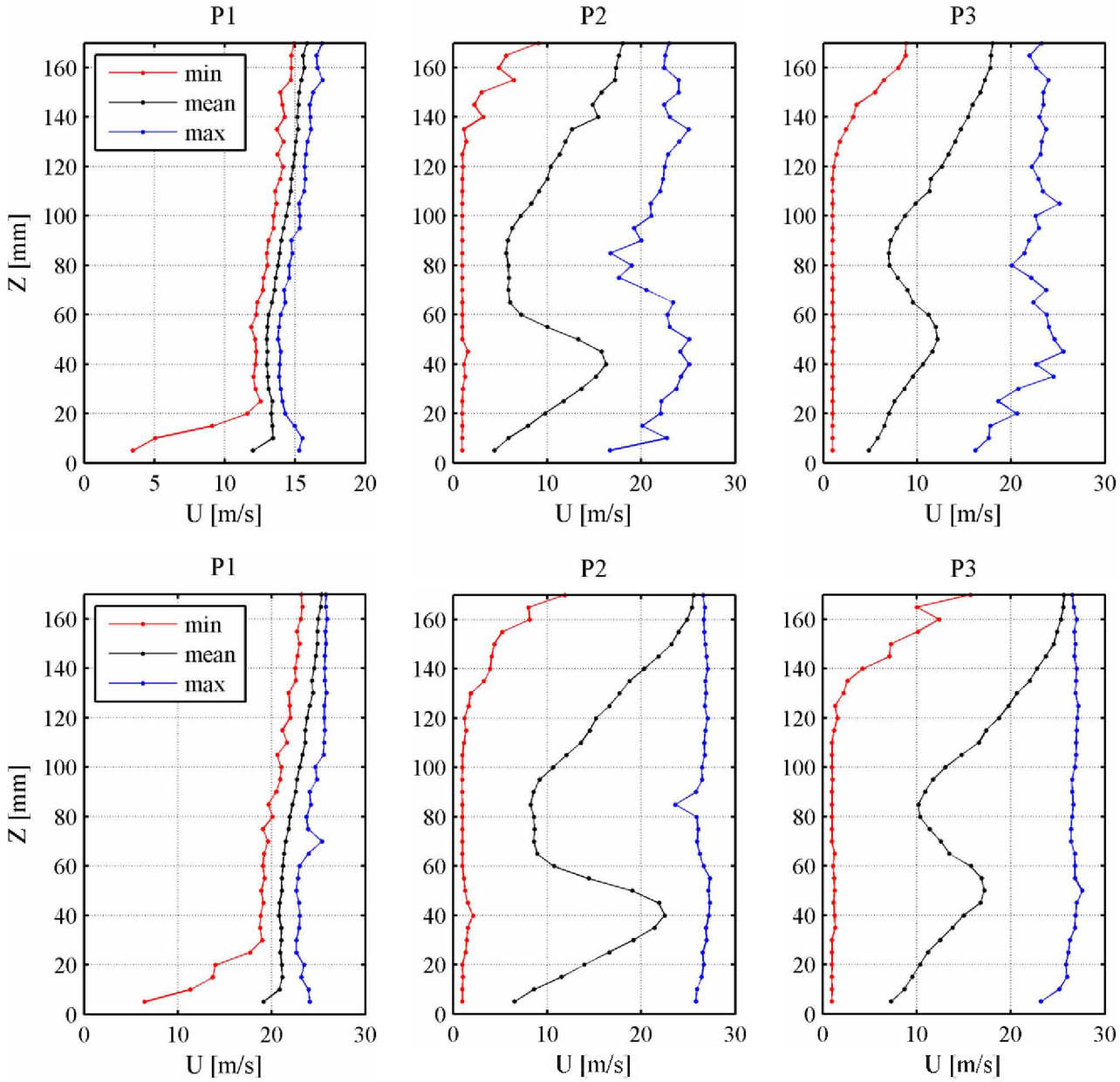

Figure 5.13 - Experimental velocity profiles limits for U_0 = 16.7 m/s (top) and U_0 = 25 m/s (bottom).

Vortex shedding frequency can be obtained using spectral analysis of the velocity signals recorded on the wake. Simulations being steady (RANS) on present work limits the study to experimental data, therefore the following discussion is prepared to serve as validation for future works.

Spectral study of the acquired signals is performed using MATLAB fast Fourier transform function. Figure 5.14 illustrates energy distribution for signal acquired at Z = 55 mm on P2 and P3. For the portrayed example, a global peak is noted around 45 Hz, however, it is clear that many scales are excited on the wake of the tested geometry, what denotes that the flow is completely developed.

Energy distribution on frequency scale for all tested positions on wake is presented on Figure 5.15. Each column of the grid is the spectral distribution of the signal obtained with the probe on the position represented on the abscissa axis for the two positions on symmetry plane (P2 and P3). For clarity, spectra presented on the grid representation are performed for 1024 points; higher discretization is used for vortex shedding frequency determination.

For U_0 = 16.7 m/s, higher magnitudes are seen for a frequency bandwidth of [40; 60] Hz, and on the same level of the negative velocities in the numerical profiles (Z = 40-60 mm). The other tested velocity presented more intense values on the vicinity of 60 Hz for Z = 60 mm.

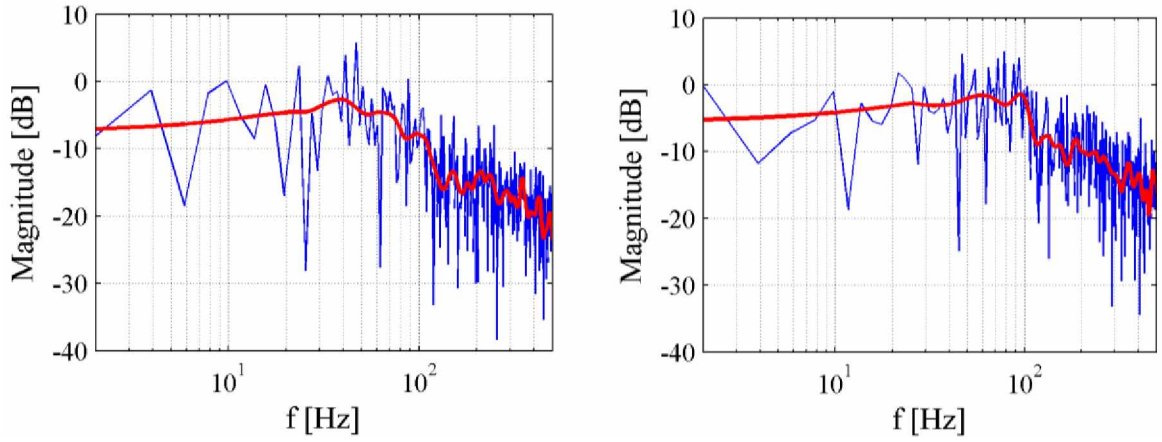

Figure 5.14 – Spectral energy distribution for velocity signal acquired at P2 (left) and P3 (right), Z = 55 mm (U_0 = 25 m/s), using unity as reference for decibels (smoothed curve in red).

Both locations of higher energy can be associated with the shear boundary formed on the rear-overhang of the pickup. Frequencies that corresponded to the global energy peak and the corresponding Strouhal number (the height of the model is used as characteristic dimension) are listed on Table 5.1. Mean is 0.378; For a hot-wire probe placed 15 mm behind the tailgate, Ha et al. (2011) observed a peak around f = 30 Hz, that corresponds to St = 0.167.

Table 5.1 – Positions and frequencies of maximum spectral energy peaks on pickup wake.

POSITION	U_0 [m/s]	Z [mm]	f [Hz]	St
P2	16.9	55	41.634	0.370
P3		65	43.594	0.387
P2	25.0	55	64.827	0.389
P3		65	61.012	0.366
			mean St	0.378

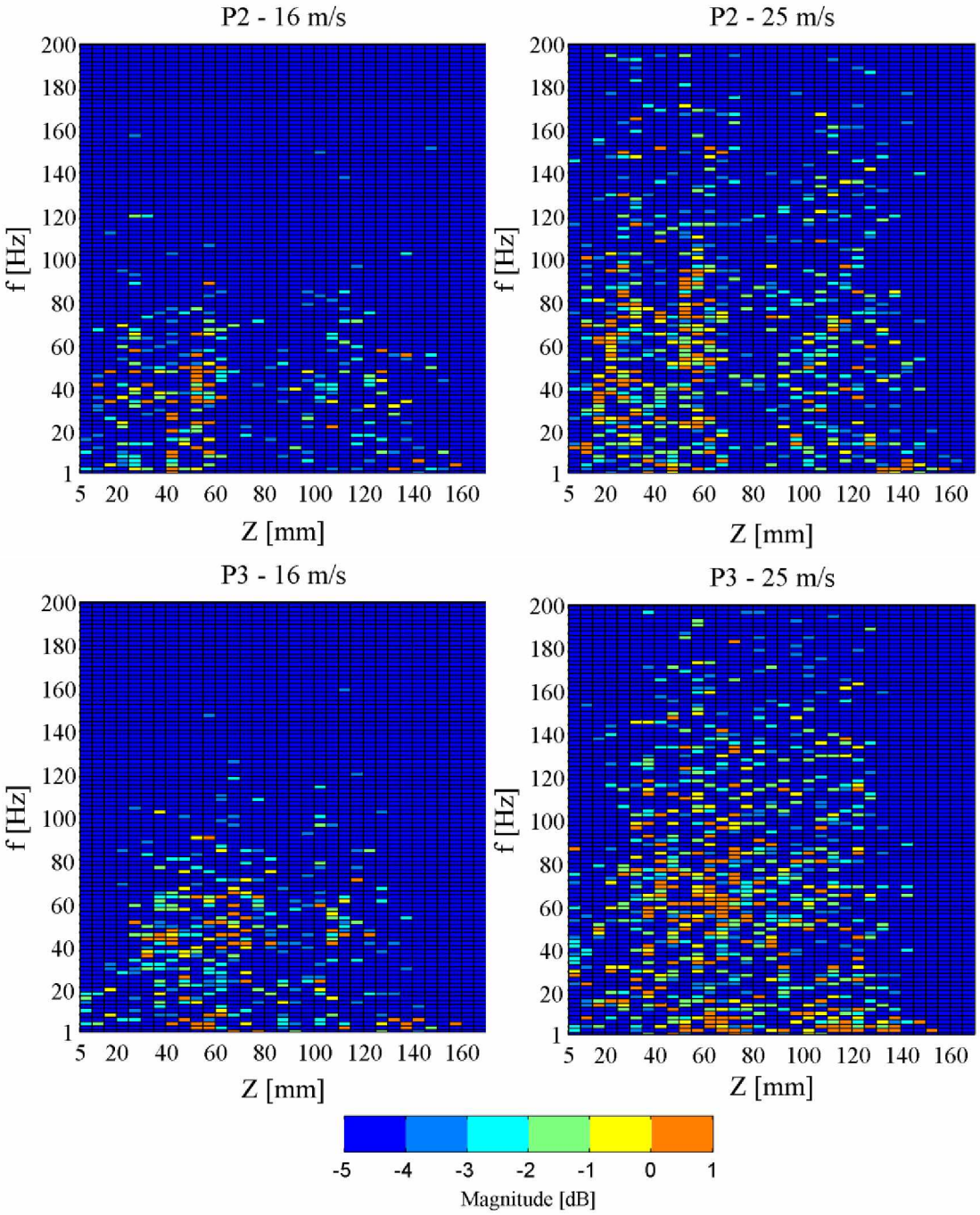

Figure 5.15 - Spectral energy distribution of measured velocities on pickup wake at P2 (top line) and P3 (bottom line) for U_0 = 16.7 m/s (left column) and U_0 = 25.0 m/s (right column), using unity as reference for decibels.

5.1.3.2. Qualitative – Wall Tufts Visualization

For flow tendency visualization, wool tufts are placed on model wall. Wind tunnel testing is performed with three velocities: U_0 = {10.0; 16.7; 25.0} m/s. Videos are recorded from lateral of the pickup and above trunk.

Figure 5.16 presents frames of the recorded videos of the trunk and Figure 5.17 illustrates images registered laterally. No clear distinction is observed from one velocity to another. Therefore, comparison with numerical results are only made with the fastest velocity (U_0 = 25 m/s), which is the one that has more discrepancy between zones.

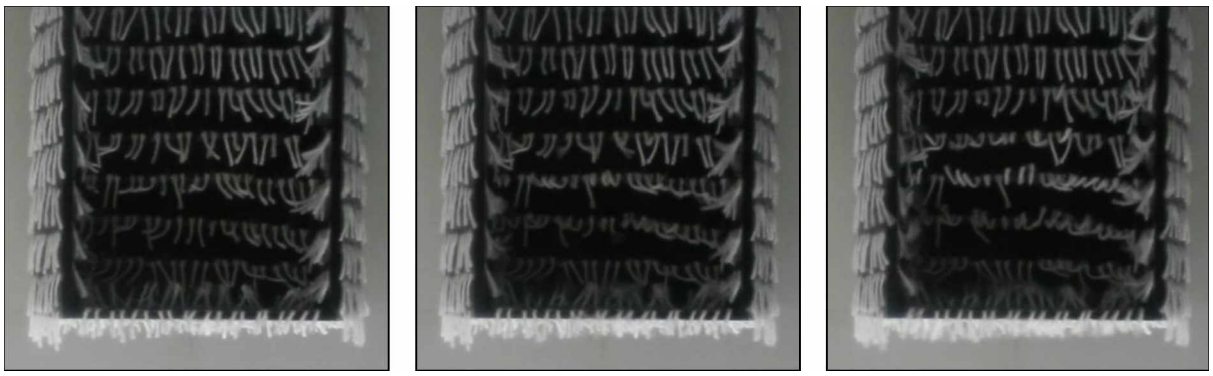

Figure 5.16 – Wall tufts on trunk for U_0 = 10.0 m/s (left), U_0 = 16.7 m/s (center) and U_0 = 25.0 m/s (right).

To compare these results with CFD flow, shear stress streamlines are presented at the surfaces of the model for both meshes.

Tufts on downstream of the trunk are elevated due to the presence of a recirculation bubble also predicted on numerical simulations. This behavior is noted only after the third line of tufts, thus, the recirculation does not occupies the entire trunk. Simulations for the BASELINE mesh reproduce this topology while TETRA solutions have the recirculation bubble starting at 2% of the bed length, as seen on Figure 5.18.

Structures that are observed on overall model are illustrated on Figure 5.19. Important features are highlighted and labelled sequentially

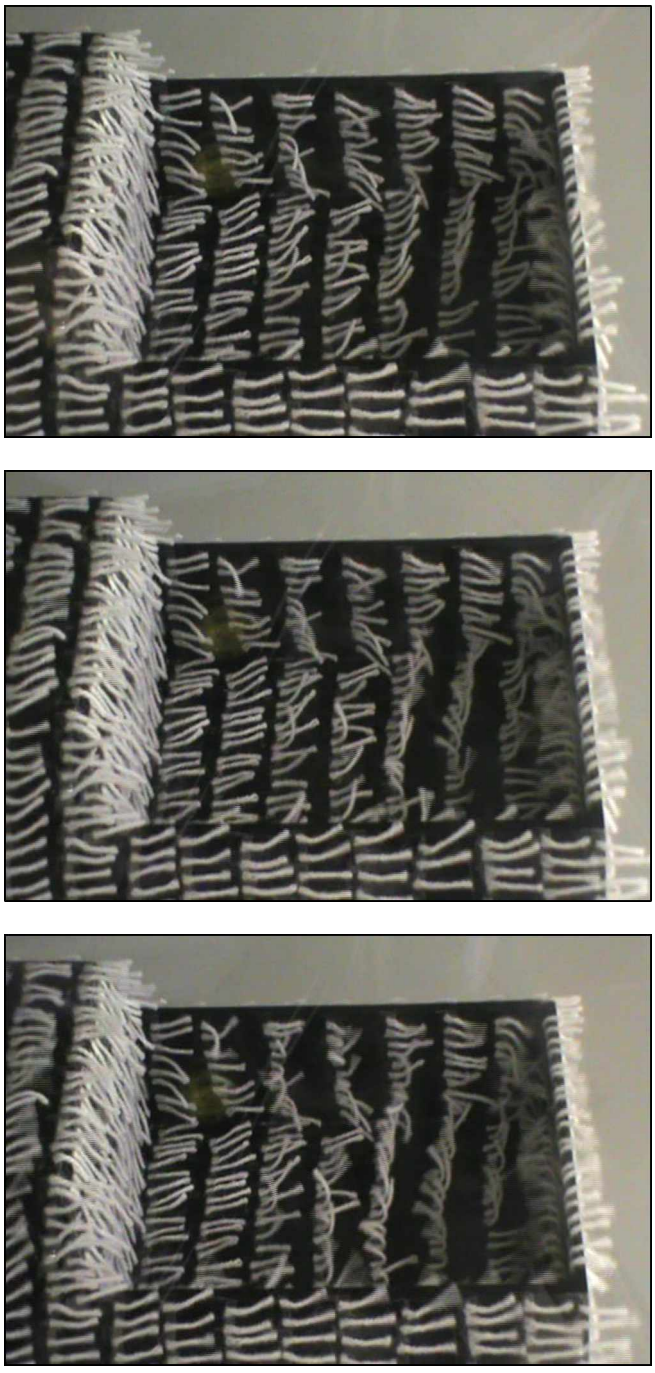

Figure 5.17 – Wall tufts on trunk for U_0 = 10 m/s (top), U_0 = 16.7 m/s (center) and U_0 = 25.0 m/s (bottom).

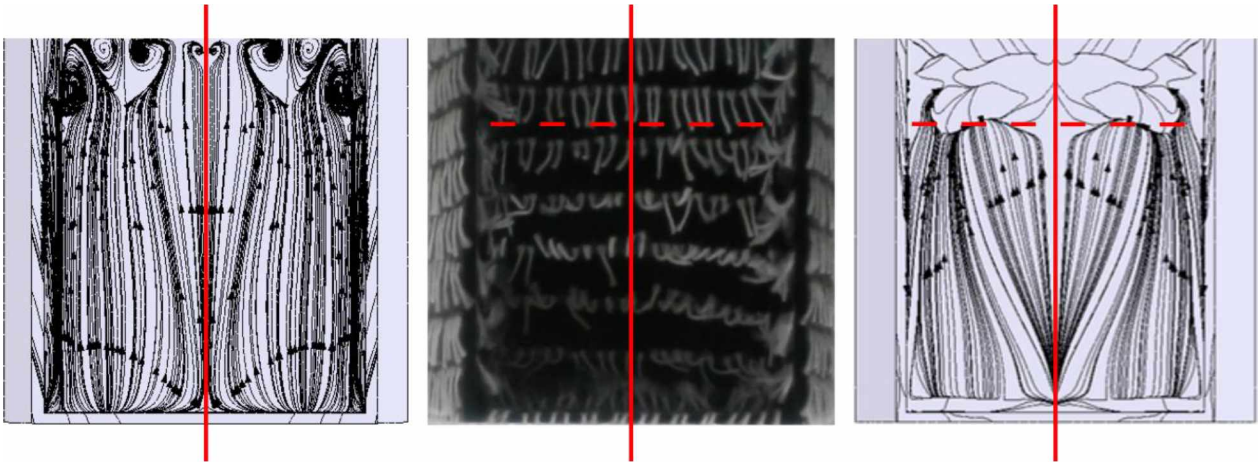

Figure 5.18 – Trunk close wall flow topology for wall tufts test (center) and shear stress streamlines on trunk surface for TETRA (left) and BASELINE (right) mesh (U_0 = 25.0 m/s).

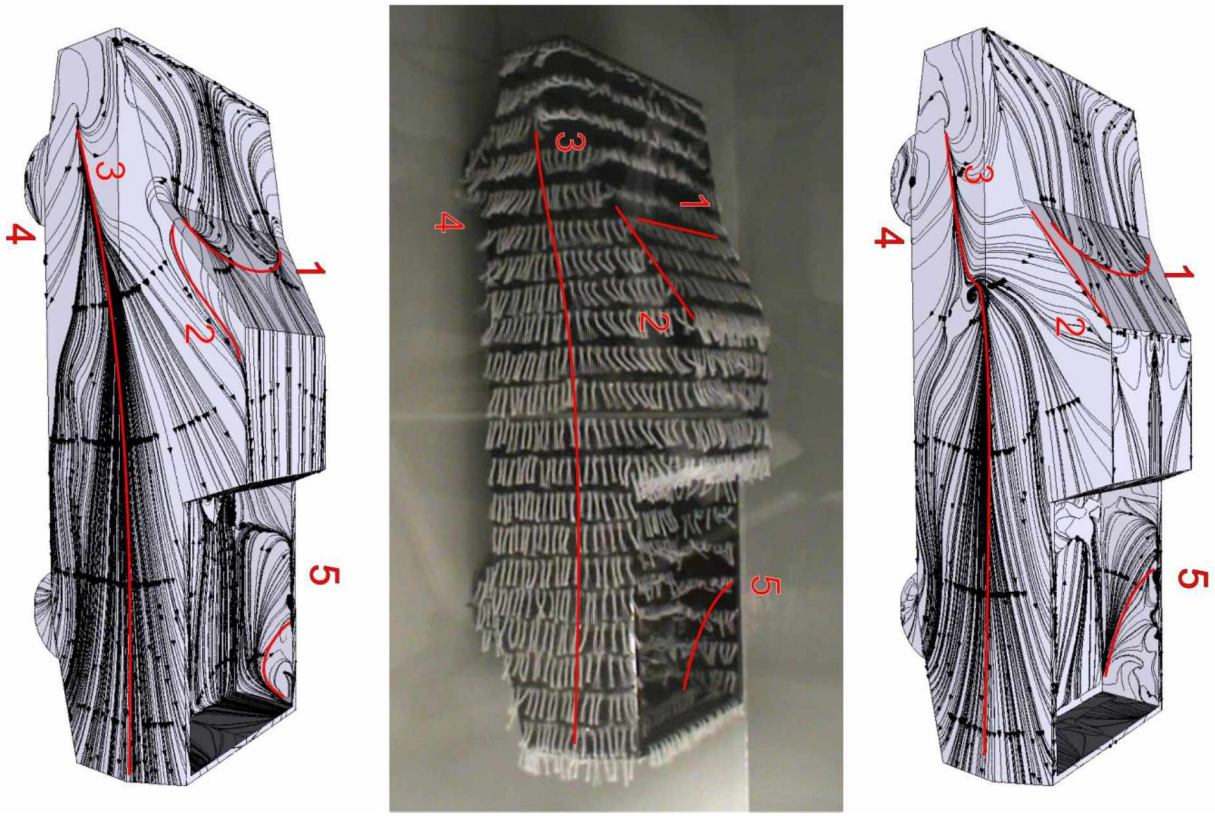

Figure 5.19 – Wall tufts (center) and numerical shear streamlines for TETRA (left) and BASELINE (right) mesh (U_0 = 25 m/s).

As on experimental visualization, flow recirculates above the hood. The limit of the recirculation zone is marked on curve (1) for both results; however, on experiments the recirculation is limited BY the hood-front windshield joint. Perturbed tufts at the vicinity of the curve (2) mark the presence of C-pillar vortex, convergence with experiments is observed for BASELINE mesh, and dislocated upstream for TETRA solution. The curve (3) delimitates tufts that are deviated up (above the curve) and down (under the curve), this separation can also be noted on CFD solution; also, the vortex at the tip of the curve proposed on both solutions is present on experiments. The disturbance of flow downstream the front wheel (4) is also predicted on both numerical solutions. A zone with no adverse flow is delimited above curve (5); it's very similar for BASELINE solution and reduced on the streamlines obtained with the TETRA mesh.

The use of wall tufts permitted the clarification of flow behavior close to the model, especially for zones under adverse pressure or flow recirculation. Even so, the produced images are very subjective and susceptible to erroneous interpretations. Combining these results with surface oil visualization methods are recommended for the oncoming.

For the qualitative and quantitative techniques deployed to describe the flow around the generic pickup model, significant deviations are noticed with CFD. Once they are also believed to be influenced by experimental conditions, and that global behavior is predicted numerically, the RANS simulations are considered physically consistent. Thus, numerical setup and domain discretization characteristics are considered validate. An important aspect that must be considered on next steps is experimental quantification of drag coefficient that may endorse this conclusion.

Although both numerical solutions present numerous similarities with wind-tunnel testing, the BASELINE mesh is closer to the experimental description of the flow and to previous analysis on literature. All the presented conclusions about the pertinence of the chosen discretization scheme for the considered problem are extended to the ROUNDED mesh, which is conceived using the same refinement. Next section is dedicated to the study of the two proposed geometries based on computational simulations performed on these two meshes.

5.2. Model study

Comparison of flow around the two proposed geometries (baseline and rounded) is presented on this section. All results are restricted to in scale simulations, freestream at U_0 = 25.0 m/s, meshes with prismatic boundaries. Discussion about meshes is presented on section 5.1.2 and velocity and scale effects are summarized on section 5.3.

Figure 5.20 presents the normalized velocity field on the symmetry plane for the baseline model. Freestream air forms a stagnation zone on pickups front end. A detachment zone on the hood front leads to an important recirculation bubble that extends to the front windshield. As noticed on previous works, a recirculation bubble is formed inside the trunk. For the proposed geometry, the bubble does not comprehend the entire trunk, smaller turbulent structures are formed on first 20% portion of the box, pushing the center of the bubble to the tailgate.

There is no recirculation outside the tailgate and a shear boundary is formed when the flow is encountered with accelerated air from underbody. A downwash on tailgate external surface is also present, as proposed on the literature (see section 2.2).

Globally, the flow follows same behavior for the rounded geometry, see Figure 5.21. Most important variations are caused by the absence of sharp edges: no recirculation above the hood and on the front overhang and no detachment above the cabin. It's plausible to admit that those effects, associated with the inclination of the contact between the cab and cabin rear surface, caused a flow deviation resulting In the presence of a smaller wake.

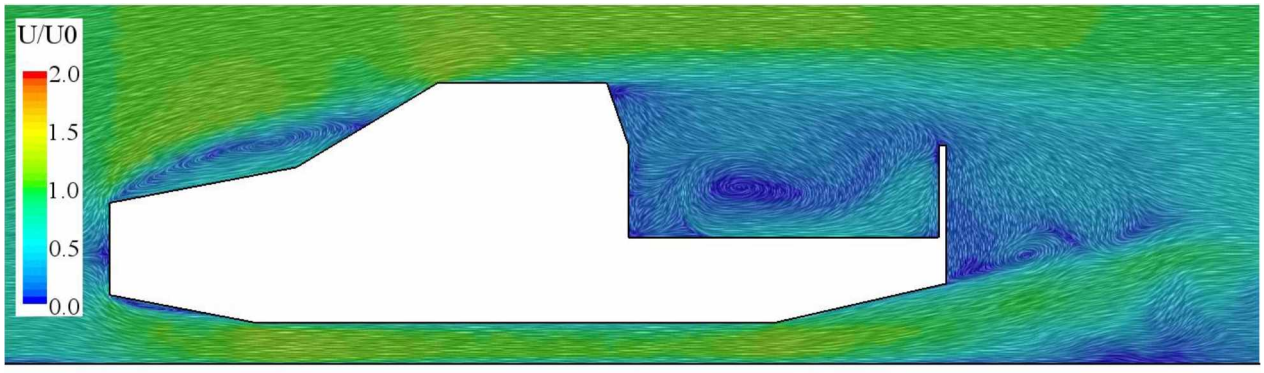

Figure 5.20 – Normalized velocity field on symmetry plane, baseline model U_0 = 25 m/s.

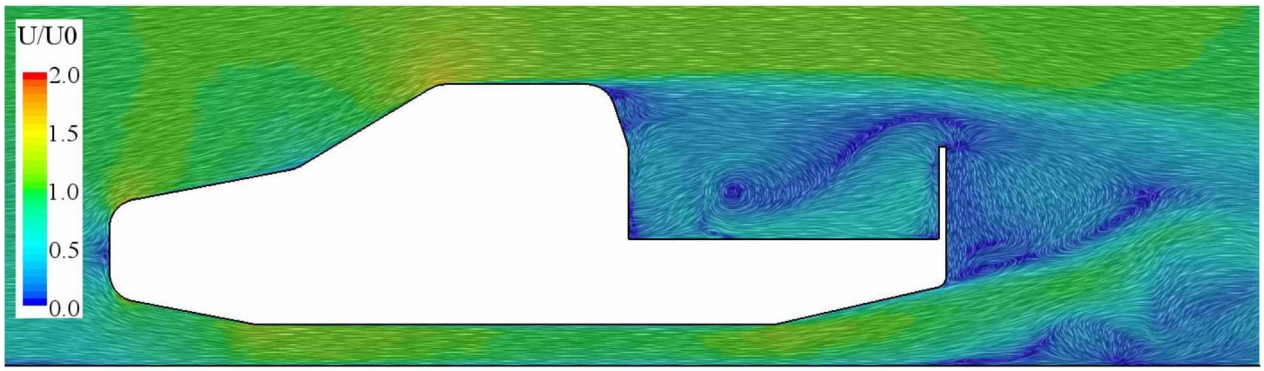

Figure 5.21 – Normalized velocity field on symmetry plane, rounded model U_0 = 25 m/s.

Differences are visible on flow on trunk. Figure 5.22 illustrates the streamlines at the trunk mid-plane for both geometries. The same vortex distribution is noted; however they vary in core location and in sizes. Secondary structures next to cabin rear surface and on tailgate are bigger for the rounded version. This behavior echoes the presence of a smaller recirculation bubble on trunk and the smaller wake.

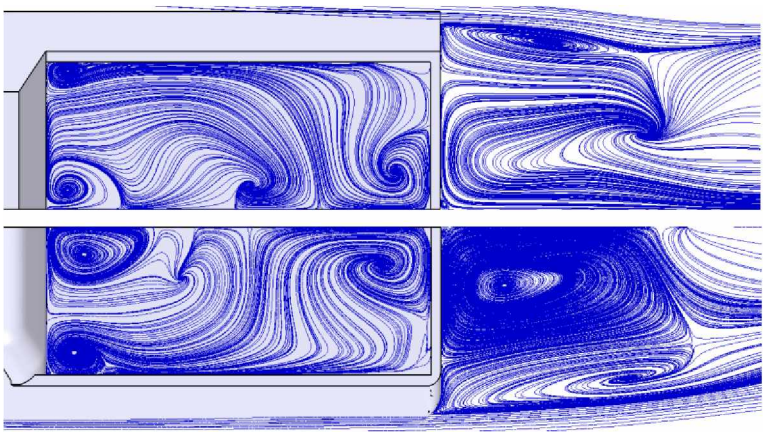

Figure 5.22 - Streamline on center of trunk for baseline (top) and rounded (bottom) models (in scale, U_0 = 25 m/s).

Figure 5.23 summarizes the evolution of surface pressure coefficient at the symmetry plane for both geometries. Besides the depression on front overhang caused by a recirculation for the baseline model, a very similar behavior is present on the remaining parts of the underbody. The same phenomenon is perceived on pickup hood: the absence of recirculation for

the rounded model and the associated pressure deviation between the tested geometries. For rounded model, maximum C_P is perceived at hood-windshield joint, dislocated by 10% of the pickup length for the baseline geometry. There is a similar evolution on the cabin roof.

The most important variations are noticed on the trunk, as evidenced on pressure coefficient graphics of Figure 5.24. The rear cabin surface and the tailgate exterior of the baseline model present both a decrease of pressure when compared to the same regions of the rounded version; opposite behavior is present on tailgate exterior part. Regarding bed region, the results are smoother for the baseline model, especially upstream the bubble, which also creates a smaller depression for this geometry (see Figure 5.23).

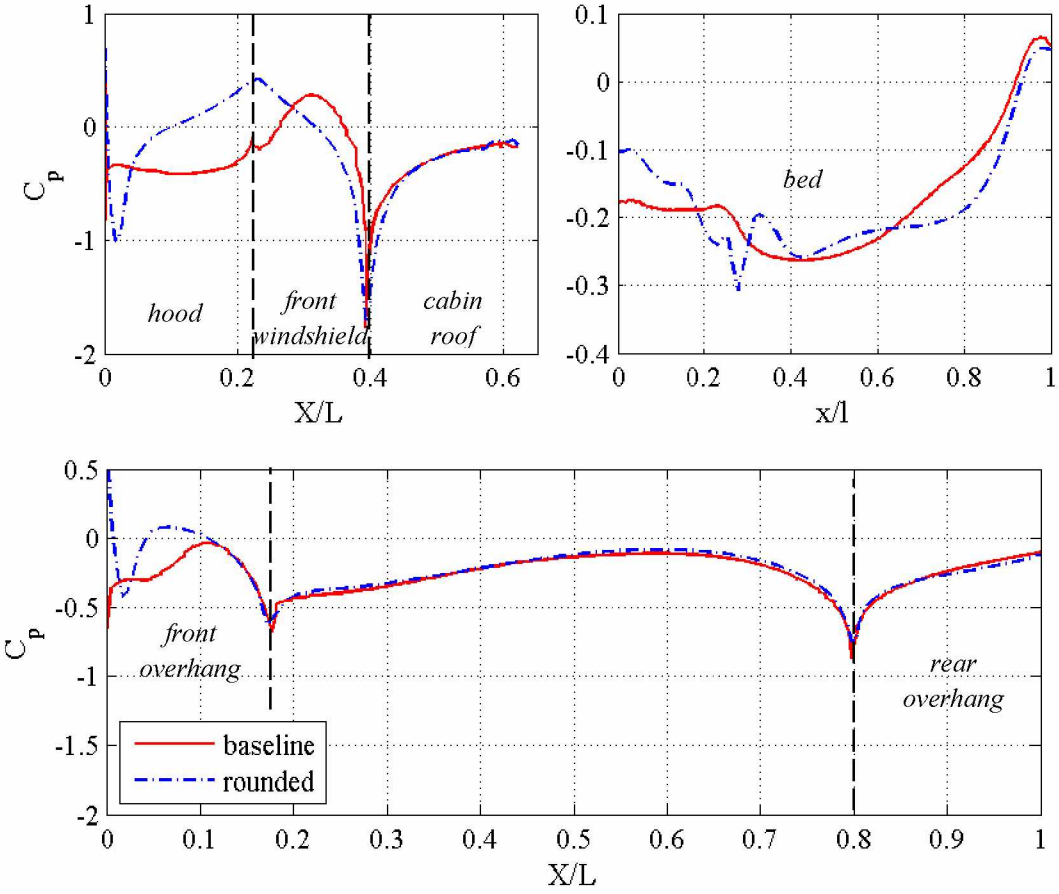

Figure 5.23 - Pressure coefficient on symmetry plane of the cab, bed and underbody for baseline and rounded models (in scale, U_0 = 25 m/s).

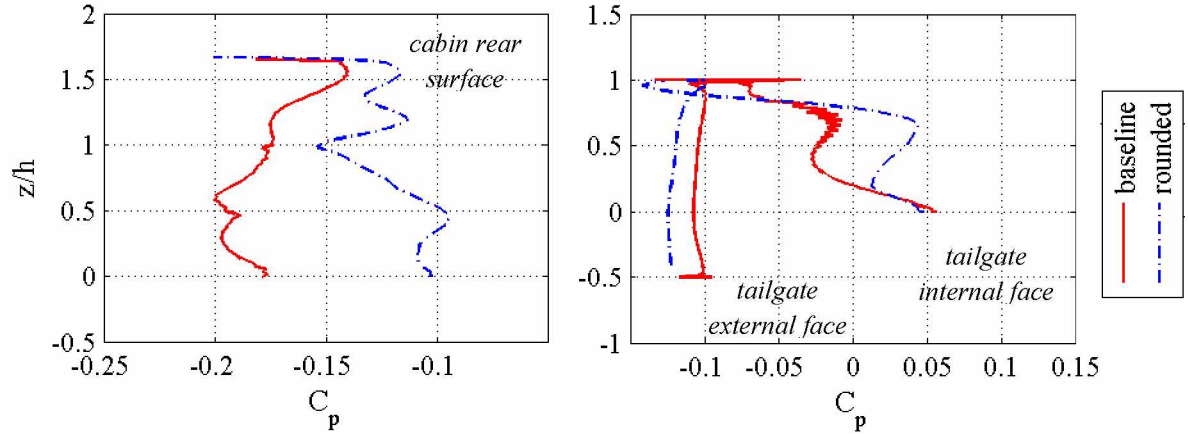

Figure 5.24 – Pressure coefficient on symmetry plane of the cabin rear surface and tailgate for baseline and rounded models (in scale, U_0 = 25 m/s).

Previous results presented a different behavior regarding the tailgate (AL-GARNI and BERNAL, 2010): the pressure on the outside is smaller than on the internal face, thus a contribution to drag can be deduced. The use of a different model with different trunk dimensions and proportions and the fact that the rear overhang is not parallel to the ground, as in previous works, may lead to a variation of the pressure distribution on tailgate. As noted by Ha et al. (2009), the relation of height and length of the trunk plays an important factor on flow behavior.

The pressure coefficient distribution on trunks surface, showed on Figure 5.25, confirms that flow follows the same behavior for both geometries; however, the magnitude of depression is smaller for the rounded pickup. The existence of a pressure depression on the side of the tailgate exterior face is caused by a recirculation promoted by flow from the pickup lateral and trunk. Many levels of C_P are perceived on cabin back face and can be related to the many structures found on this region (upstream the recirculation bubble).

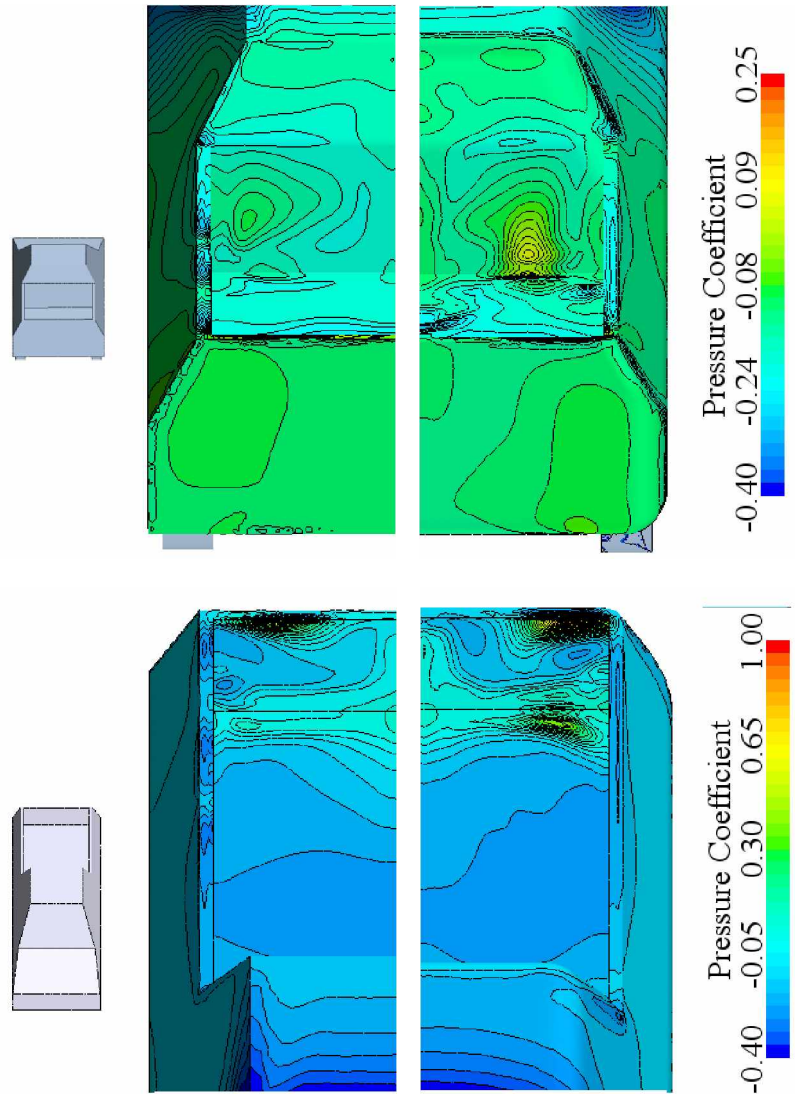

Figure 5.25 – Surface pressure coefficient on rear cabin and tailgate exterior (top) and on bed and tailgate interior (bottom) for baseline (left) and rounded (right) models (in scale, U_0 = 25 m/s).

Tridimensional visualization is possible on Figure 5.26. As mentioned earlier, solution is performed for only half model and results are mirrored for clarity. The front wheels are responsible for the formation of a significant number of vortical structures and a smaller density appears on rear wheels. As proposed by Al-Garni and Bernal (2010), cab vortex is noticed and no clear vortical behavior is noted on the symmetry plane of the model. As mentioned earlier, two vortexes, supposedly counter rotating, are formed by the interaction of air from the laterals

and flow leaving the trunk (“tailgate vortex”). The center of that vortex is not on center of the tailgate;

Flow is much less perturbed by the rounded model, as seen on Figure 5.27. The cab vortex is unnoticed on the chosen iso-surface magnitude but the structure is still present. This behavior confirms the mentioned characteristics of the derived geometry when regarding the baseline model. There is no recirculation on the hood and A-pillar structures are not present either.

Figure 5.26 – Iso-surface of λ_2 =-4.0 × 10^4 s^{-2} for baseline model, in scale U_0 = 25 m/s.

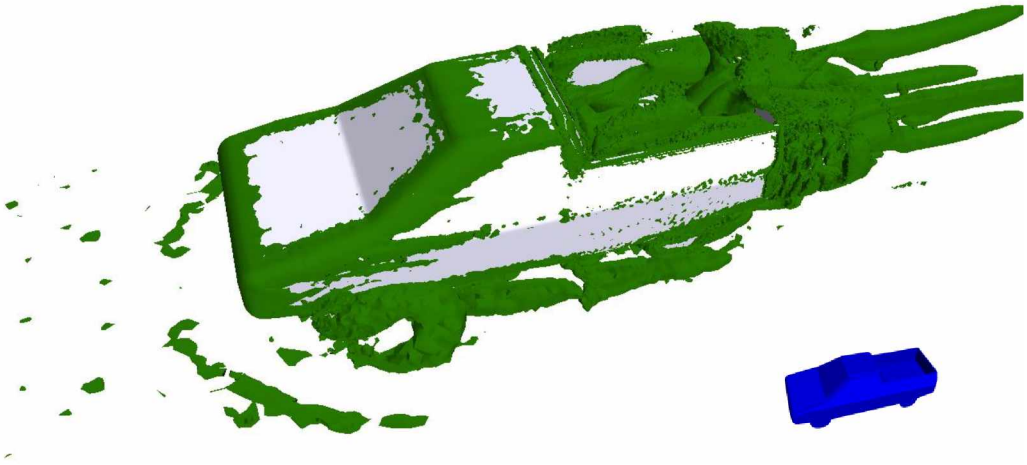

Figure 5.27 – Iso-surface of λ_2 =-4.0 × 10^4 s^{-2} for rounded model, in scale U_0 = 25 m/s.

All those variations have an influence on the predicted drag for the two pickup models: the in scale baseline model presented for the chosen velocity a drag coefficient of C_D^B = 0.5376; for the rounded model, C_D^R =0.3607 (33% smaller). Lift is not well predicted for both simulations.

Previous considerations are focused on only one velocity and model scale. The influence of variating the scale (Re) of the flow is discussed next.

5.3. Scale study

For both models, simulations are performed for three freestream velocities U_0 = {16.667; 25.000; 33.333} m/s that correspond to typical highway speeds U = {60; 90; 120} km/h. The use of in scale model subjected to the same freestream velocity is not dynamic similar to the original problem. According to Hucho (1987), once main source of drag is pressure difference, Reynolds may not influence on force coefficients. However, the mechanisms of boundary layer detachment are highly influenced by it. To question the correlation of mechanically un-similar flows around pickups, a scale study is performed numerically.

The simulations are executed for both in scale and real size pickup, so a total of 6 scales are tested for each model. Using the solver standard air properties of density and viscosity, the correspondent Reynolds numbers are listed on the following table.

Table 5.2 – Tested scales

#	Scale	U_0 [m/s]	L [m]	Re
1	1:10	16.667	0.447	4.76×10^5
2		25.000	0.447	7.13×10^5
3		33.333	0.447	9.51×10^5
4	1:1	16.667	4.470	4.76×10^6
5		25.000	4.470	7.13×10^6
6		33.333	4.470	9.51×10^6

When solving equations for the flow around a specific geometry, baseline or rounded, the same mesh is used. A scale factor of 10 in applied on each directions. Thus, the same elements are considered but they are 10 times bigger. Results are for meshes with prismatic boundaries (BASELINE and ROUNDED).

Velocity iso-surface of 1/3 of the freestream speed at the wake of the pickup is presented for the first three tested scales for baseline and rounded pickups on Figure 5.28. Flow disturbance upstream the pickup is unchanged for each model. Cab and tailgate vortex are visible; structures formed on frontal wheel vary on size but maintain shape. Although discrepancies can be pointed for both models, the solutions for the rounded version deviates

more one from the other. The same behavior is repeated on pressure distribution graphs presented next.

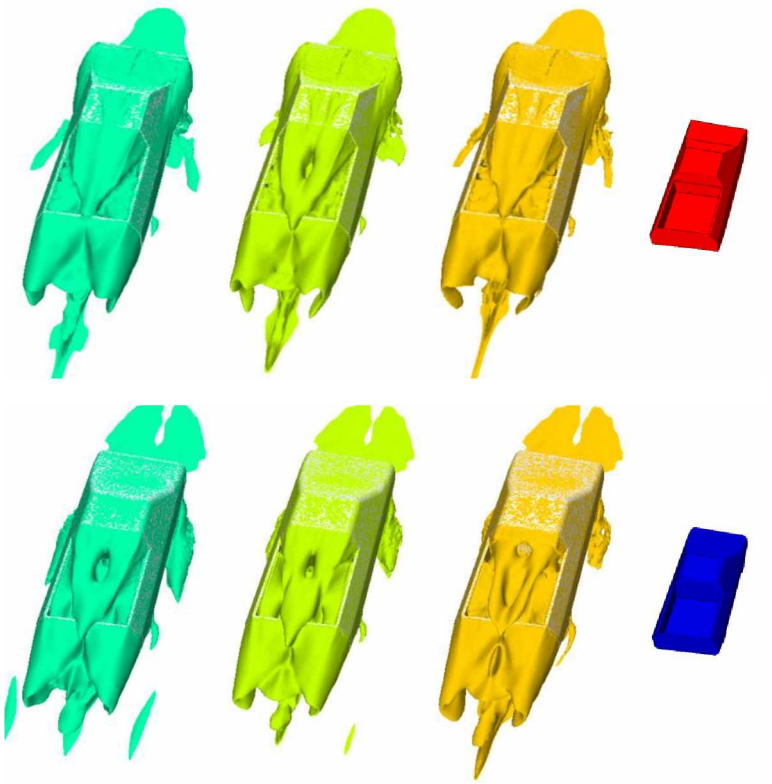

Figure 5.28 – Iso-velocity surface for 1/3 of freestream velocity: U_0 = 16.67 m/s (left column), U_0 = 25.00 (center column) and U_0 = 33.33 m/s (right column), for baseline(top line) and rounded (bottom line) in scale models.

As indicated on Figure 5.29 and Figure 5.31, there is no significant variation for the C_P on both the underbody and the superior part of the vehicle (hood and front windshield) on symmetry plane of both geometries. A different behavior is noticed for the trunk.

For baseline mode, pressure coefficient evolution on bed, cabin back and tailgate, follow same behavior discussed on previous section. Variations are of low order and are considered to be of the same magnitude of numerical solution instabilities. Variations are in a more important scale for rounded pickup simulations. The increase of velocity resulted in bigger recirculation bubble on trunk (C_p plateau on bed's tip pushed upstream) and smaller pressure depression on bed. Pressure increases gradually with Reynolds number for all points at the cabin rear surface; on tailgate exterior face, the increase is abrupt and important variations are noticed.

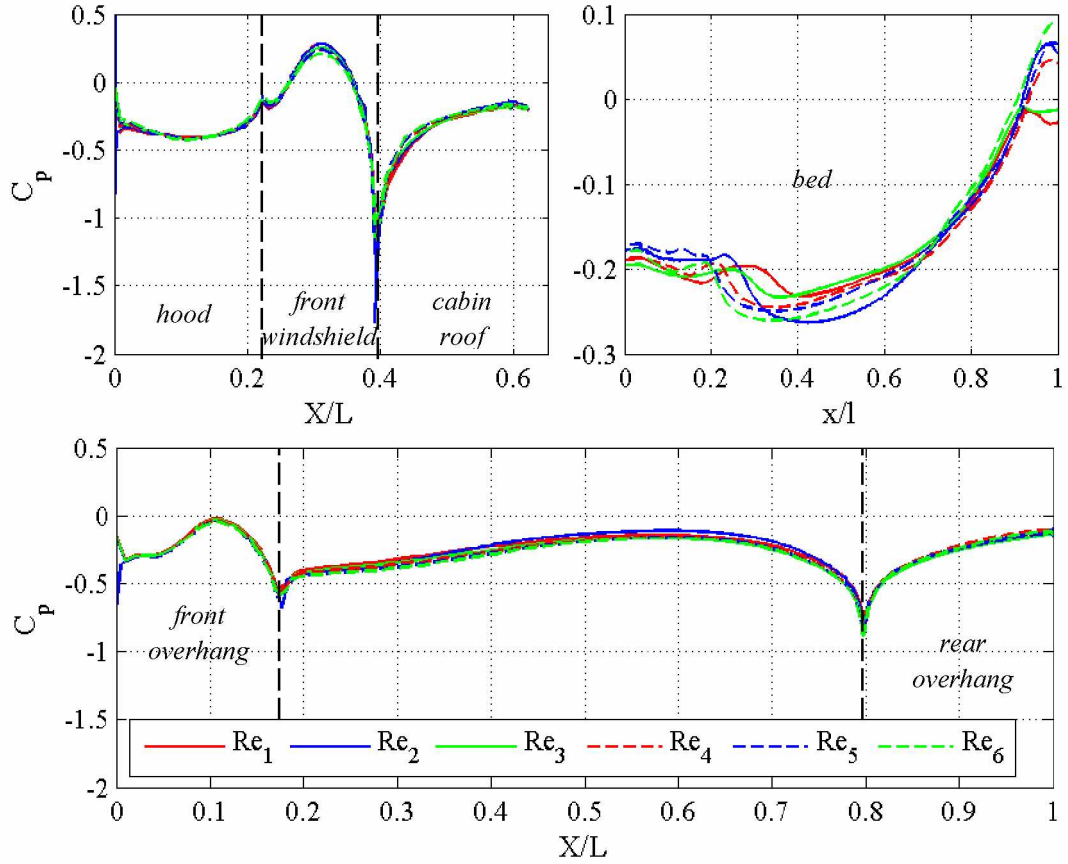

Figure 5.29 - Pressure coefficient on symmetry plane of the cab, bed and underbody of the baseline model in all scales.

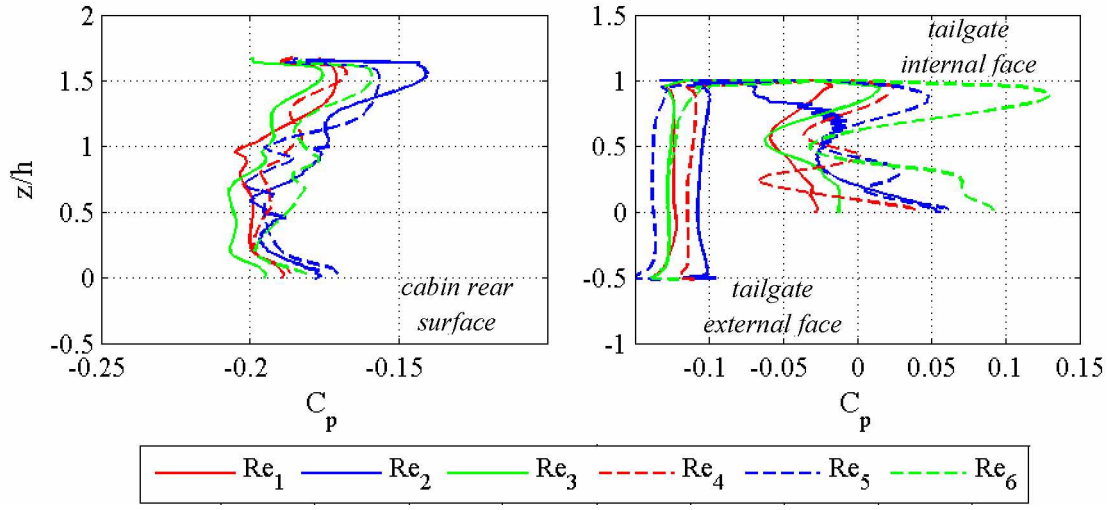

Figure 5.30 – Pressure coefficient on symmetry plane of the cabin rear surface and tailgate of the baseline model in all scales.

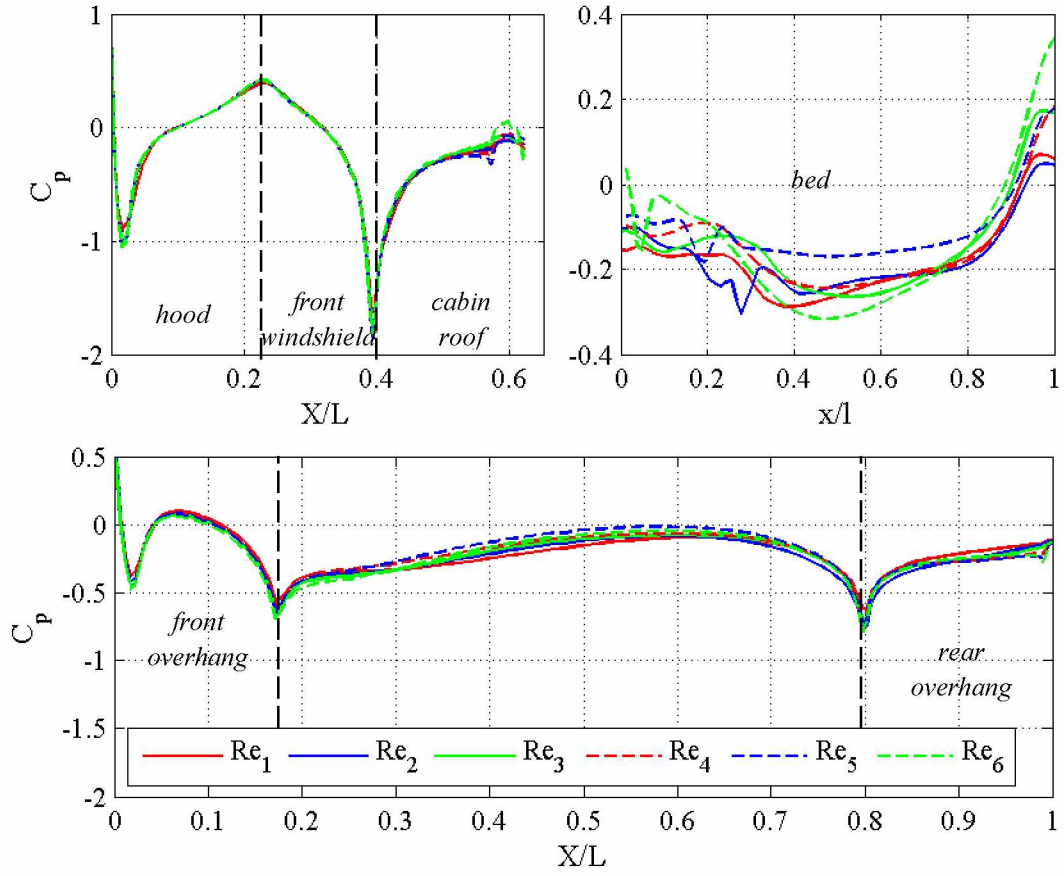

Figure 5.31 - Pressure coefficient on symmetry plane of the cab, bed and underbody of the rounded model in all scales.

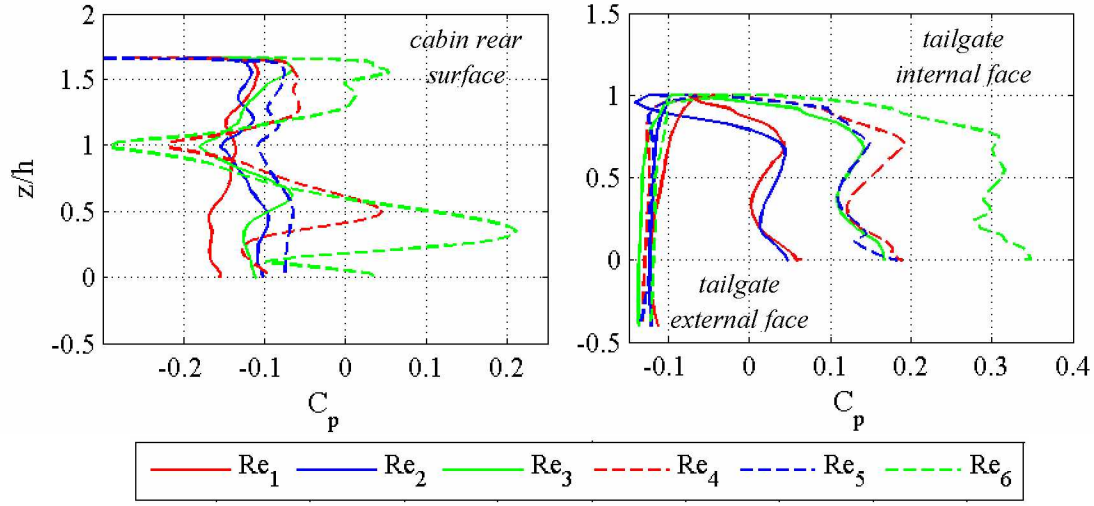

Figure 5.32 – Pressure coefficient on symmetry plane of the cabin rear surface and tailgate of the rounded model in all scales

The biggest divergences are present between the solutions for the rounded model. On the streamlines at the symmetry plane, presented on Figure 5.33, it's visible that the velocity alone plays a role in shaping the structures on the wake. However, there is a clear distinction when the size of the model (variation in scale) is considered. When the same analysis is done for the solutions of the baseline geometry, variations are smaller and thus omitted on this document.

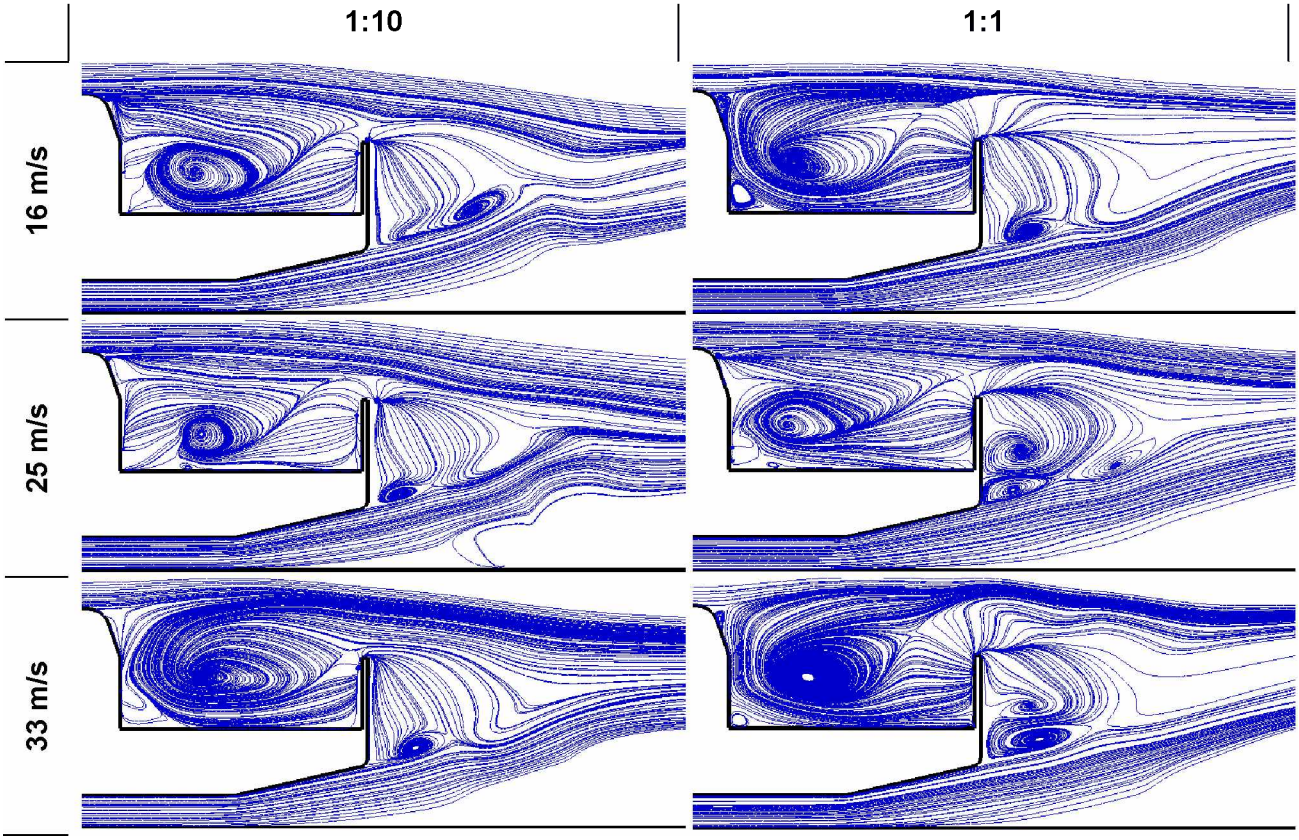

Figure 5.33 - Streamline on symmetry plane for rounded model in scale (left) and full size (right) for U_0 = 16 m/s (top), U_0 = 25 m/s (center) and U_0 = 33 m/s (bottom).

Those observed differences are going to be discussed for the two extremum of the tested Reynolds range: in scale, U_0 = 16.667 m/s (Re1); and full size for U_0 = 33.333 m/s (Re6).

Normalized velocity fields on symmetry plane are presented on Figure 5.32 for both solution samples. On front part of the vehicule, the solution is the same for both conditions (stagnation point and decellaration on hood-front windshield joint). For trunk and wake, the solution for the in scale geometry is very similar to the result discussed on section 5.2: recirculation bubble starting at about 20% of bed's length; shear boundary on both cab and underbody, and detachement downstream the pickup. The Re6 simulation has a reciruclattion bubble that corresponds the entire trunk, and the presence of small vortex on tailgate exterior, leading to an elevation of shear layer formed on the cab and consequentely a bigger wake.

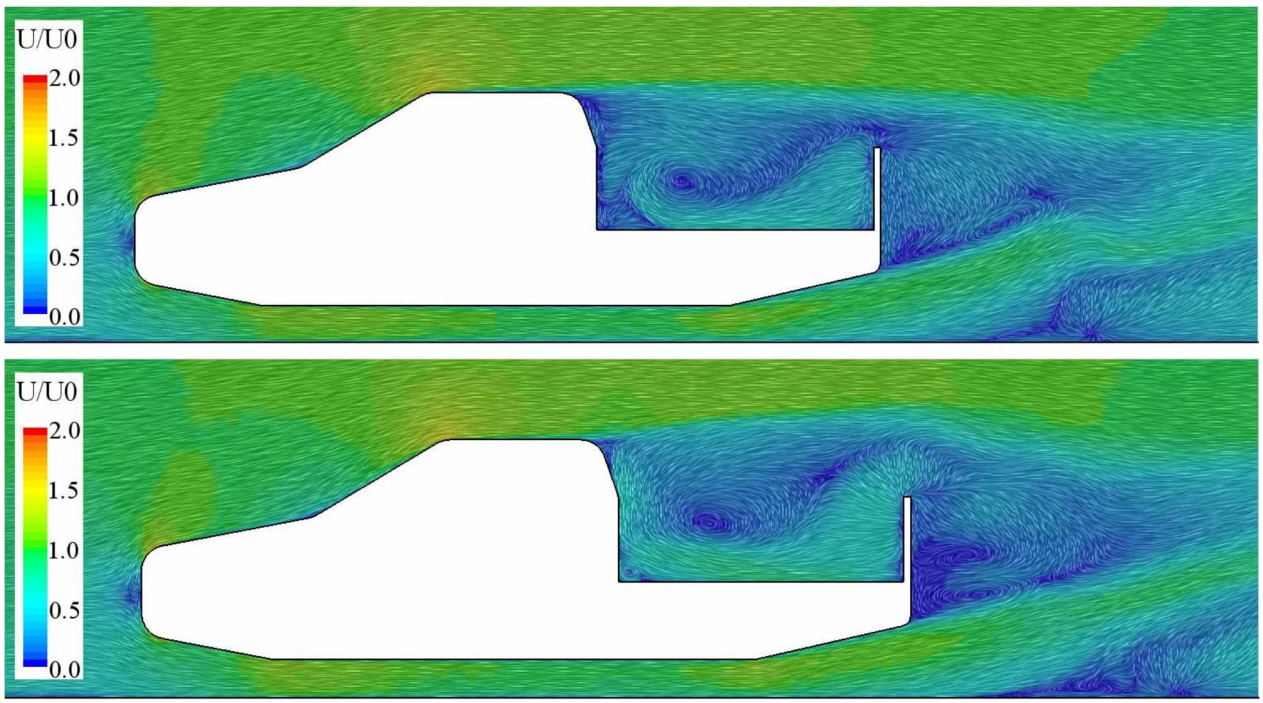

Figure 5.34 - Normalized velocity field on symmetry plane at Re1 (top) and Re6 (bottom) for rounded model.

Similar behavior is noted on streamline on horizontal plane at the center of the trunk (Figure 5.35). Smaller structures are present after cabin back surface on the center of trunk only for the smallest Reynolds, but overall flow is maintained.

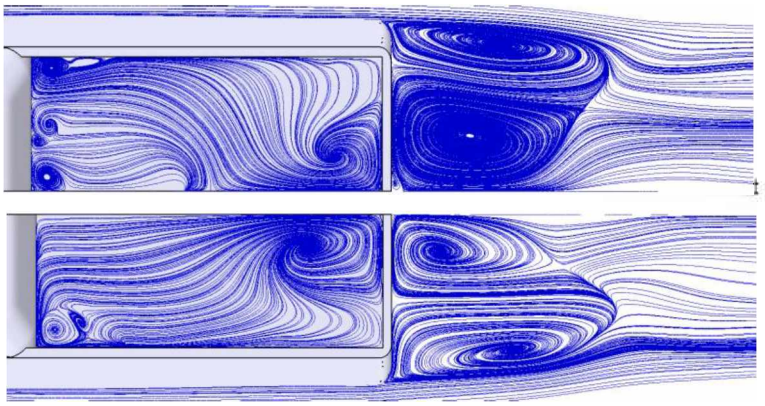

Figure 5.35 - Streamline on center of trunk for rounded model for two scales: Re1 (top) and Re6 (bottom).

It's noted on the symmetry plane and at the trunk that structures are similar but there is a variation in size and distibution of flow topology downstream the cab. Figure 5.36 ilustrate with iso-velocity surfaces that both results have tailgate vortex and the downwash proposed by Al-Garni and Bernal (2010). However, evolution of cab votex is more defined for the first scale as well as the disturbance provoqued by the front wheel.

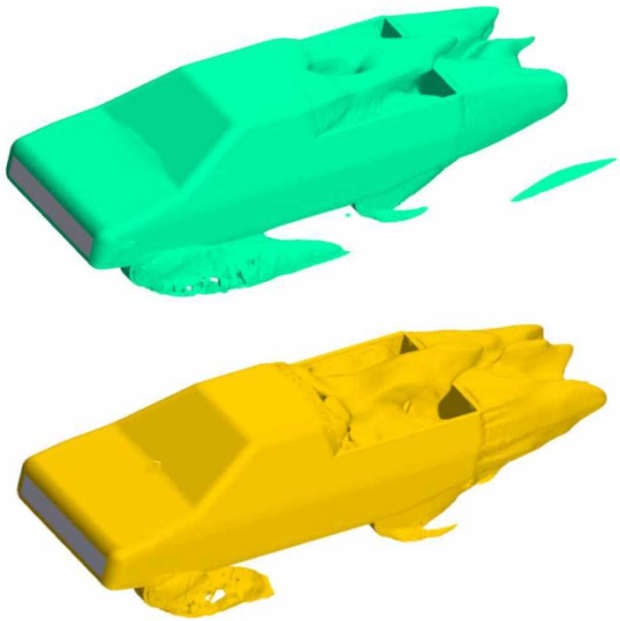

Figure 5.36 – Iso-velocity surface for 1/3 of freestream velocity for Re1 (top) and Re6 (bottom) for rounded model (structures on upstream of the model are omitted).

In conclusion, smaller structures are not represented, therefore the vortex distribution on the wake and the flow at trunk variates. This behavior is not as critical for the baseline model once detachment zones are well defined for sharp edges.

Discrepancies are believed to be also caused by poor modeling of the physics of the flow, reflected on the difficulty to achieve consistent convergence. This conclusion applies especially with the extended mesh, once all phenomena are limited to volumetric elements with a minimum size of 20 mm and a prismatic boundary ten times higher.

In terms of drag coefficient, rounded model presents a 30% smaller C_D than baseline's for all scales. Global trend is the same as on previous works on generic pickups (AL-GARNI; BERNAL, 2010; MOKHTAR et al. 2009): for the tested speeds, with the increase of the velocity there is an increase of drag. Figure 5.37 illustrates the evolution of the drag coefficient for both models; C_D varies from 0.5334 to 0.5498 for baseline pickup and from 0.3411 to 0.3815 for the rounded version.

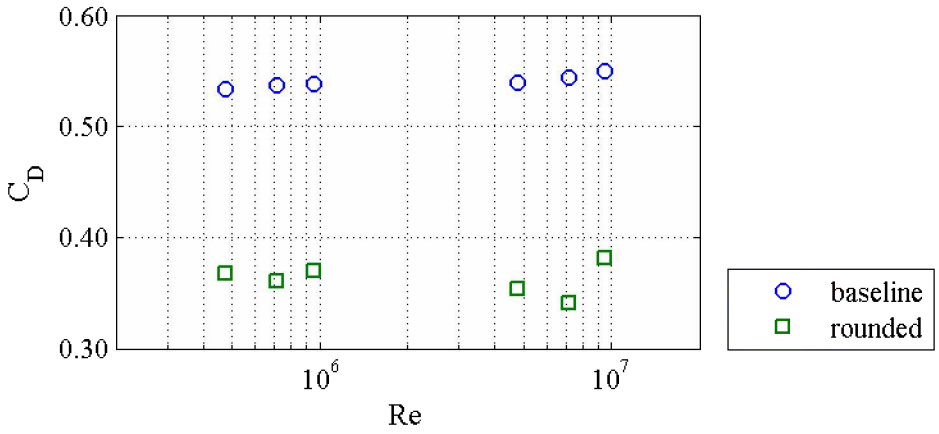

Figure 5.37 - Drag coefficient for all on scales.

For all scales, average drag coefficient are CDB = 0.5405 and CDR = 0.3624 for baseline and rounded models, respectively. When comparing to the local values, maximum deviation is around 5%, as represented at Figure 5.38. The linear evolution of the drag observed for baseline pickup is not reproduced for rounded model.

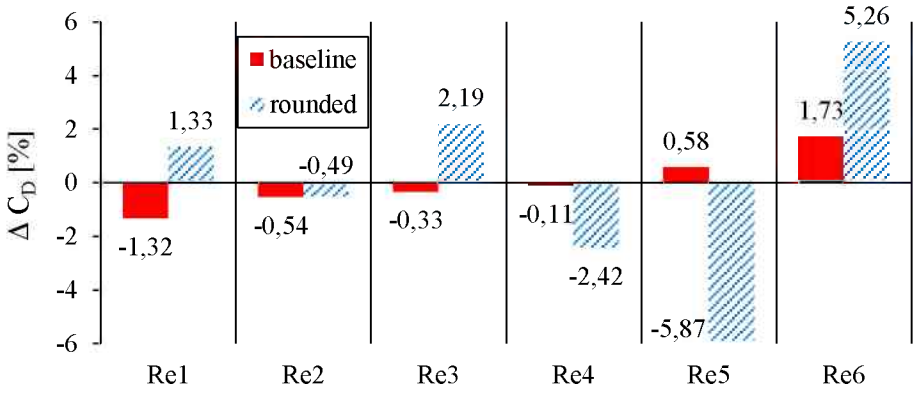

Figure 5.38- Percentage C_D oscillation from all scales average value for baseline and rounded models.

The scale study for the rounded geometry repeats the results of the comparison between meshes. For TETRA mesh, global behavior is also achieved, but the poor representation of smaller scales resonates in a different vortex distribution. When in scale, the flow is very similar to the experiments and well correlates with descriptions on the literature; the use of the extended meshes is very similar to the mesh with no boundary discretization: recirculation bubble comprehends the entire trunk; and absence of smaller scales.

Solutions of the flow fields around the baseline model are considered invariant for the tested range of Reynolds. Observed disparities are of small order and are considered to be a due to numerical instabilities. This phenomenon may be related to the fact that separation will occur in the same way for all Reynolds numbers for bodies with sharp edges (HUCHO, 1987), and a coarse discretization has consequently minor influence. For simulations with the TETRA mesh, the influence of changing scales is also small.

Even though CFD results have disparities, preliminary conclusion indicates that the problem is independent of Reynolds number from 4.76×10^5 to 9.51×10^6. The use of more refined meshes for the real size model must be performed and the use of different numerical setups is necessary to confirm this conclusion.

CHAPTER VI

Conclusion

A numerical and experimental study of the aerodynamics of a generic pickup was performed. Studied geometry was established on the dimensions of the most representative models of the light pickup fleet in Brazil. Baseline model is composed only by sharp edges and flat surfaces; a second version was prepared filleting those edges (rounded model). Numerical steady simulations (RANS) were performed on commercial software Star-CCM+ using the SST k-ω turbulence model; tetraedrical meshes have an average of 8 million elements. All simulations were prepared on an i7 processor with 12 cores, 48 GB of RAM. For wind-tunnel testing, model was 3D printed in 1:10 scale. On experimental procedures, qualitative (wall tufts visualization) and quantitative (hot-wire anemometry velocity profiles) tests revealed main structures on wake and on the close wall.

Even though a new geometry is studied, obtained solution is similar to what is described on the literature. Rounded version presented a drag coefficient 30% smaller than baseline's.

For the velocity profiles, acceleration due to the underbody constriction and the shear boundary formed on the cab were well defined. However, the use of hot-wire anemometry technique was unable to capture the small and negative velocities. The wall tufts defined recirculation regions and detached parts of vehicle's surfaces. The main structures were reproduced on numerical results for the refined mesh (with prismatic boundary).

For the performed scale study, first impression implicate that the problem is independent of Reynolds for the tested range. Although results are limited to the many simplifications of the model (no lateral rear mirrors, simplified underbody and wheels compartment, no air inlets and outlets) and of the solver (incompressible flow, stationary equations, and stationary wheels), the in scale study of a generic pickup is an important step to comprehending and optimizing real models aerodynamics.

Refinement of numerical calculation with the test of different turbulence models and the use of unsteady simulation is essential on the continuation of this work. The use of other experimental procedures such as force coefficients quantification and oil visualization methods is crucial to validate and extend the results. A study of drag reducing devices and different pickups configurations and geometries is recommended as next step.

REFERENCES

AGELIN-CHAAB, M. Structure of turbulent flows over two-dimensional bluff bodies inspired. **International Journal of Heat and Fluid Flow**, p. 417–430, 2014.

AL-GARNI, A. M.; BERNAL, L. P. Experimental study of a pickup truck near wake. **Journal of Wind Engineering and Industrial Aerodynamics**, p. 100-112, 2010.

AL-GARNI, A. M.; BERNAL, L. P.; KHALIGHI, B. Experimental Investigation of the Near Wake of a Pick-up Truck. **SAE Paper 2003-01-0651**, 2003.

BURGIN, M.; DUMAN, O. Statistical Convergence and Convergence in Statistics. arXiv preprint math/0612179, 2006.

BUTZ, L. A.; DONAVAN, P. R.; GONDERT, T. R.; MACDONALD, R. A.; WOOD, D. H. 1988 Chevroletl/GMC Full-Size Pickup Truck Aerodynamics. **SAE Technical Paper 872274**. 1987.

CHEN, K.-H.; KHALIGHI, B. A CFD Study of Drag Reduction Devices for a Full Size Production Pickup Truck. **SAE Technical Paper 2015-01-1541**, 2015.

COOPER, K. Pickup Truck Aerodynamics - Keep Yout Tailgate Up. **SAE Technical Paper 2004-01-1146**, 2004.

FENABRAVE. Varejo Nacional. Retrieved December 29, 2015, from <http://www3.fenabrave.org.br:8082/plus/modulos/conteudo/?tac=dados-regionais-dados>

GUILMINEAU, E. Numerical Simulation of Flow Around a Generic Pickup with ISIS-CFD. In: Proceedings of ASME 2010 3rd Joint US-European Fluids Engineering Summer Meeting. Montreal: ASME, 2010.

HA, J.; JEONG, S.; OBAYASHI, S. Drag Reduction of a Pickup Truck by a Rear Downward Flap. International Journal of Automotive Technology, 12, p. 369-374, 2011.

HA, J.; OBAYASHI, S.; KOHAMA, Y. Drag Characteristics of a Pickup Truck according to the Bed Geometry. In: PROCEEDINGS OF THE 7TH IASME/WSEAS INTERNATIONAL CONFERENCE ON FLUID MECHANICS AND AERODYNAMICS, 7, pp. 122-127, 2009.

HOLLOWAY, S.; LEYLEK, J. H.; YORK, W. D. Aerodynamics of a Pickup Truck: Combined CFD and Experimental Study. **SAE Int. J. Commer. Veh. 2(1),** p. 88-100, 2009.

HUCHO, W.-H. **Aerodynamics of Road Vehicles**: From Fluid Mechanics to Vehicle Engineering. 1st ed. London: Butterworth-Heinemann, 1987.

HUCHO, W-H; SOVRAN, G. Aerodynamics of road vehicles. **Annu. Rev. Fluid Mech.**, vol. 25, no 1, p. 485-537, 1993.

INOVAR AUTO, Conheça o INOVAR-AUTO. Retrieved December 29, 2015, from <http://www.inovarauto.mdic.gov.br/InovarAuto/public/inovar.jspx?_adf.ctrl-state=6nan5b3fo_9>

JINDAL, S.; KHALIGHI, B.; IACCARINO, G. Numerical Investigation of Road Vehicle Aerodynamics Using Immersed Boundary RANS Approach, **SAE Technical Paper 2005-01-0546**, 2005.

JØRGENSEN, F. E. How to Measure Turbulence with Hot-wire Anemometers. Dantec Dynamics A/S, 2004.

KING, L. V. On the Convection of Heat from Small Cylinders in a Stream of Fluid: Determination of the Convection Constants of Small Platinum Wires, with Applications to Hot-Wire Anemometry. **Phil. Trans. Roy. Soc. A214**, pp. 373-432, 1914.

LEE, D.; PARAMESWARAN, S. Transient Numerical Simulation of the Flow Field Around a Pickup Truck. In: FOURTH INTERNATIONAL SYMPOSIUM ON COMPUTATIONAL WIND ENGINEERING, 4. Yokohama, 2006.

MERZKIRCH, W. **Flow Visualization**. 2 ed. London: Academic Press, 1987.

MOKHTAR, W. A.; CAMP, R. E. Pickup Trucks - Box Configuration and Drag Reduction. In: 28TH AIAA APPLIED AERODYNAMICS CONFERENCE, 28, 2010.

MOKHTAR, W. A.; BRITCHER, C. P.; CAMP, R. E. Further Analysis of Pickup Trucks Aerodynamics. **SAE Technical Paper 2009-01-1161,** 2009.

MOKHTAR, W.; KIM, J.; PATTERMANN, J.; MENON, V. A CFD Study of Pickup Truck Aerodynamics. In: PROCEEDINGS OF THE 2011 ASEE NORTH CENTRAL & ILLINOIS-INDIANA SECTION CONFERENC, 2011.

MOUSSA, A. A.; FISCHER, J.; YADAV, R. Aerodynamic Drag Reduction for a Generic Truck Using Geometrically Optimized Rear Cabin Bumps. **Journal of Engineering**. 2015.

MOUSSA, A. A.; YADAV, R.; BAKER, J.; FISCHER, J. Geometry Optimization of Aerodynamic Add-on Devices Using the Globalized and Bounded Nelder-Mead Algorithm. **International Journal of Engineering Research & Technology**, 3(2), p. 2268-2273. 2014.

The International Council on Clean Transportation. (2011). European Vehicle Market Statistics: 2011 Pocketbook. Washington DC.

The Wall Street Journal. Retrieved December 29, 2015, from Auto Sales - Markets Data Center: <http://online.wsj.com/mdc/public/page/2_3022-autosales.html>.

WANG, H.; LIN, T.; YUAN, X.; ZHANG, Q. Simulation and Aerodynamic Optimization of Flow Over a Pickup Truck Model. **SAE Technical Paper 2014-01-2437**. 2014.

WHITE, F. M. **Fluid Mechanics**. 4 ed. London: McGraw-Hill Higher Education, 1998.

WOOD, R. M., & BAUER, S. X. (2003). Simple and Low-Cost Aerodynamic Drag Reduction Devices for Tractor-Trailer Trucks. 2003.

.

APPENDIX I

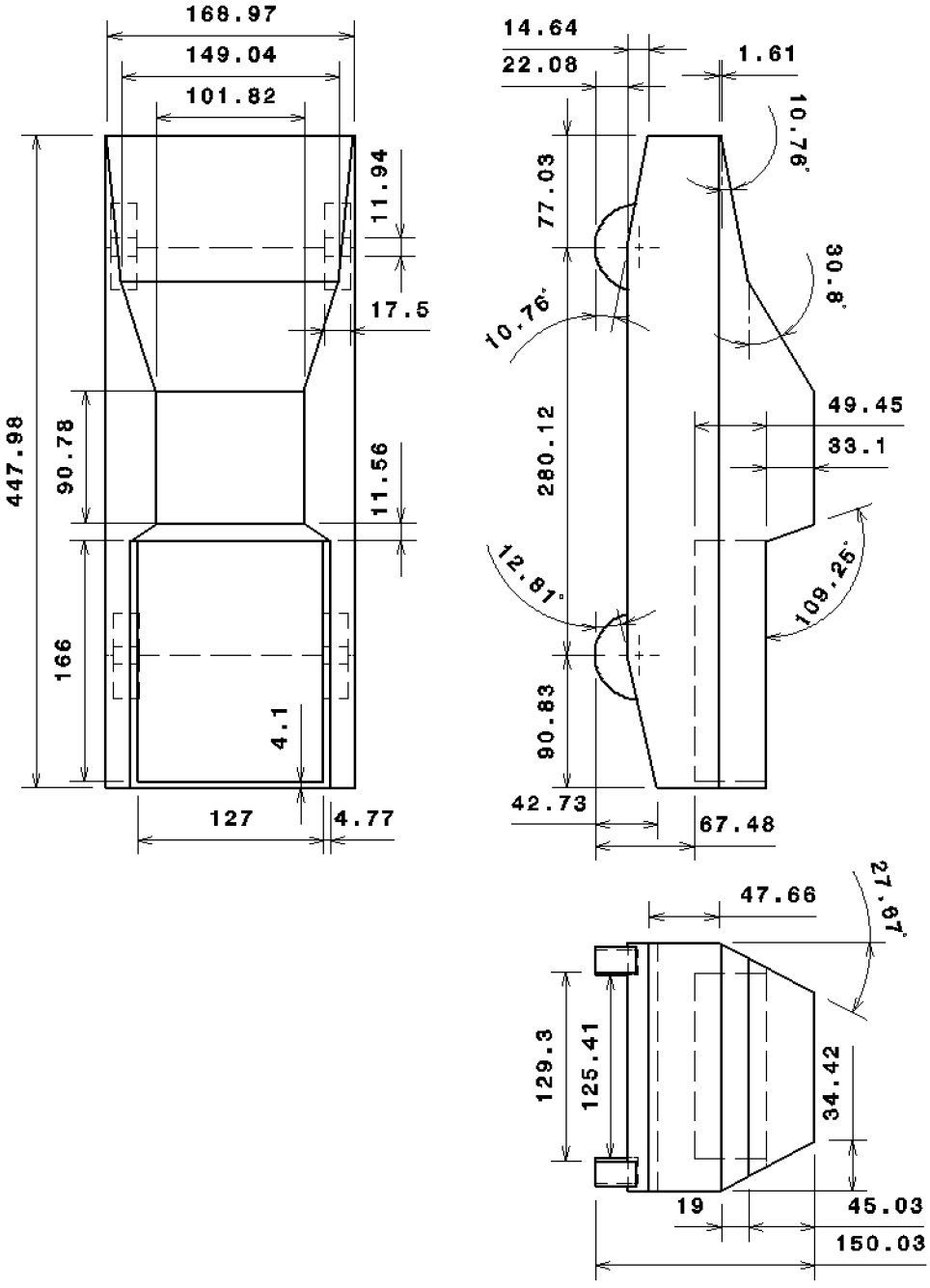
168.97
149.04
101.82
11.94
17.5
447.98
90.78
11.56
166
4.1
127
4.77
14.64
22.08
1.61
10.76°
77.03
30.8°
10.76°
49.45
33.1
280.12
12.81°
109.25°
90.83
42.73
67.48
47.66
27.78°
129.3
125.41
34.42
19
45.03
150.03

APPENDIX II

In order to perform the experimental procedures, validation and calibration routines are made on wind-tunnel. Two procedures are responsible for increasing flow quality at the test section: first, rotor rebalancing and a net was added at the beginning of the expansion; later, a total of sixteen 15 cm long guide vanes were placed right before the net in order to reduce rotating tendency at the test section (see Fig. I). On the following graphs on this appendix, the previous wind-tunnel condition is referred as 'initial; 'fix' and 'guides' refer to two quality increasing processes, respectively.

The results presented here proceed from hot-wire testing. The parameters are the same used on the experiments: 1D probe placed along the flow, 4^{th} degree polynomial calibration law, N = 32,768 acquisition points of and acquisition frequency of 2 kHz. All measurements are performed on the symmetry plane of test section. Tests for boundary layer and turbulent intensity characterization and calibration are presented next.

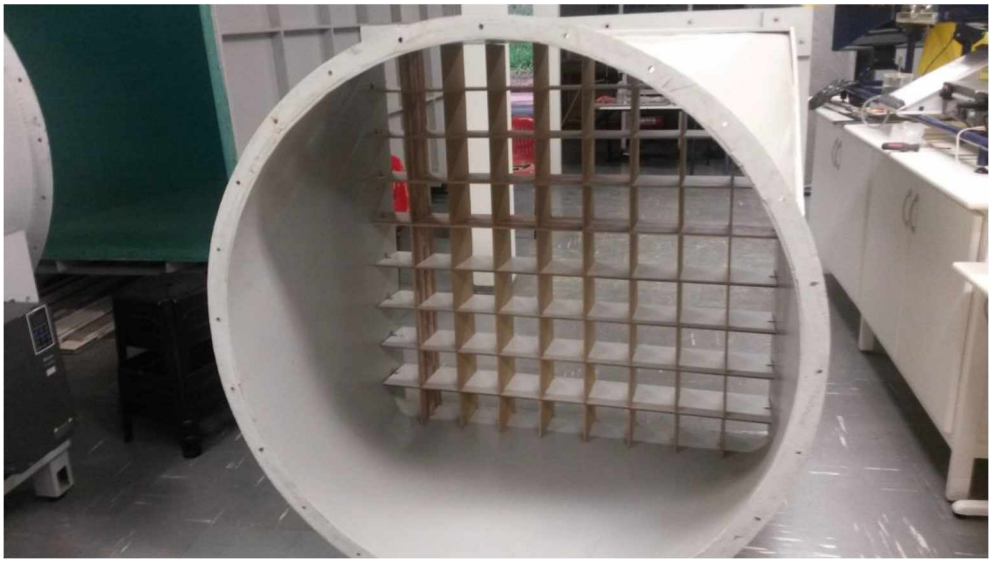

Figure I – Guide vanes installed on wind-tunnel.

I - Boundary layer

Boundary layer is defined for 'initial' and 'fixed' setups. The hot-wire probe support is placed on test section roof and measures are performed from ascending direction. For both configurations the boundary layer thickness is less than 7 mm, as presented on the normalized profiles of Fig. II. Properties of the last experiment are presented on Table I. Obtained shape factors are typical of turbulent boundary layers (WHITE, 1998).

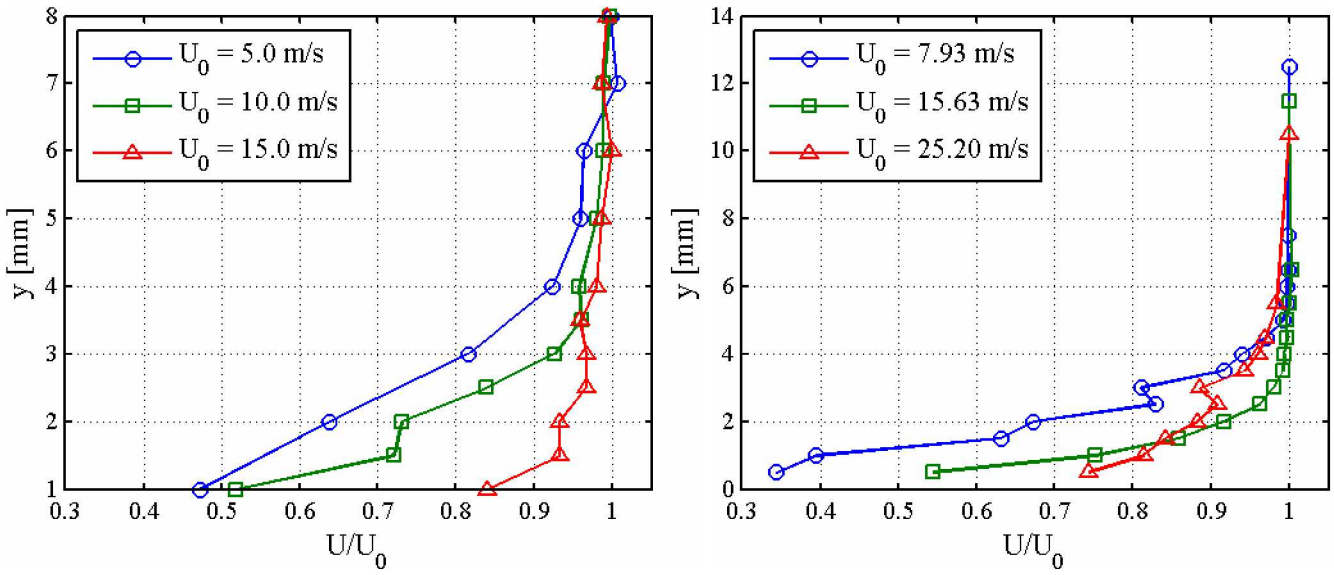

Figure II – Normalized velocity profile at the boundary layer of 'initial' (left) and 'fixed' condition (right).

Table I – Boundary layer properties.

U_0 [m/s]	LAYER THICKNESS	DISPLACEMENT THICKNESS	MOMENTUM THICKNESS	SHAPE FACTOR
	δ [mm]	δ* [mm]	θ [mm]	H = δ*/θ
7.93	4.5	1.0973	0.6454	1.7003
15.63	3.0	0.3801	0.2830	1.3431
25.20	5.5	0.5169	0.4490	1.1512

II – Calibration and Turbulence Intensity

For the probe placed 15 cm away from the wall, velocity is acquired for several motor frequencies. Tests are done for support placed at the test section roof for the two first conditions and on test section floor for the last one. For the same data, calibration is performed and test section turbulence intensity is evaluated. Figure III shows the calibration points for the three conditions and the respectively coefficients for the derived regression lines are listed on Tab. II.

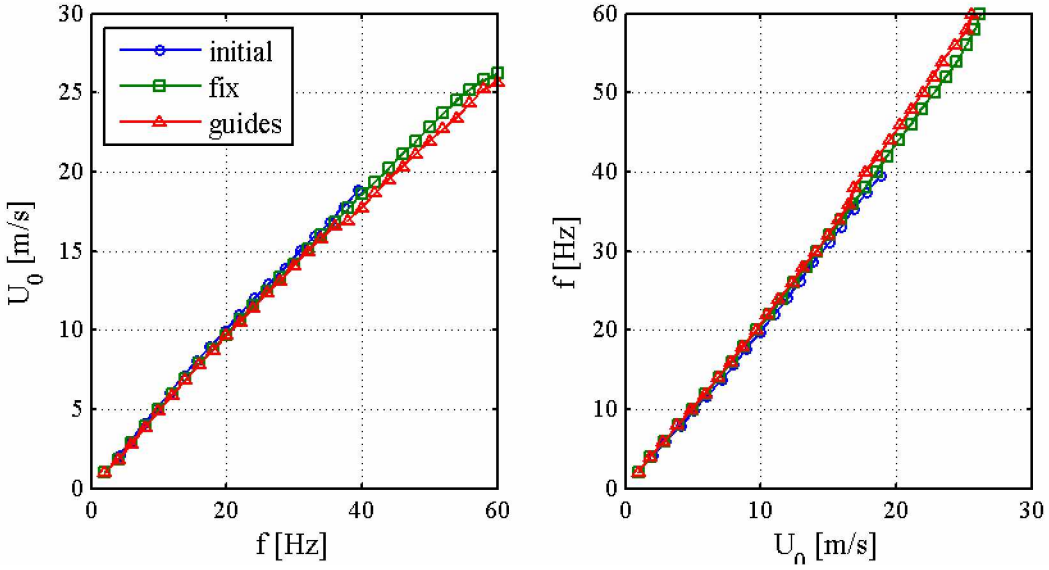

Figure III - Calibration points.

Table II – Calibration coefficients.

	initial	fix	guides
	f [Hz] = A × U [m/s] + B		
A	2.1311	2.2576	2.3481
B	-1.0539	-1,4427	-1.8464
	U [m/s] = C × f [Hz] + D		
C	0.4686	0.4422	0.4248
D	0.5080	0.6635	0.8192

Last obtained calibration curve for the current condition of the wind-tunnel is presented on Fig. V.

The net and guide vanes that were add to the wind-tunnel reduced its maximum air velocity from 26.20 m/s to 25.63 m/s (decrease of 2%). However, the two performed enhancements caused a decrease on turbulent intensity for all tested velocities (see Fig. IV). Considering all scales, average turbulent intensity dropped from 1.2234 % to 0.8116 %. The rotational behavior observed on test section was mitigated by the guide vanes.

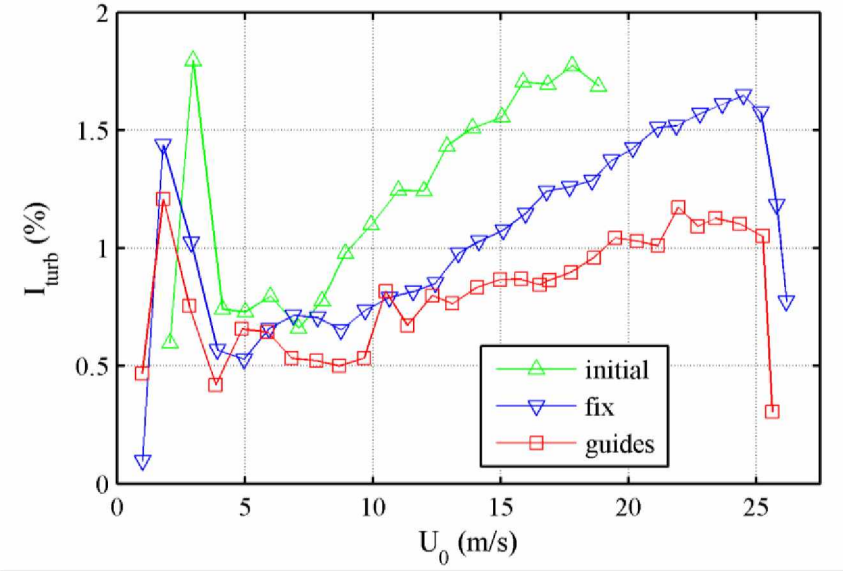

Figure IV – Turbulent intensity evolution.

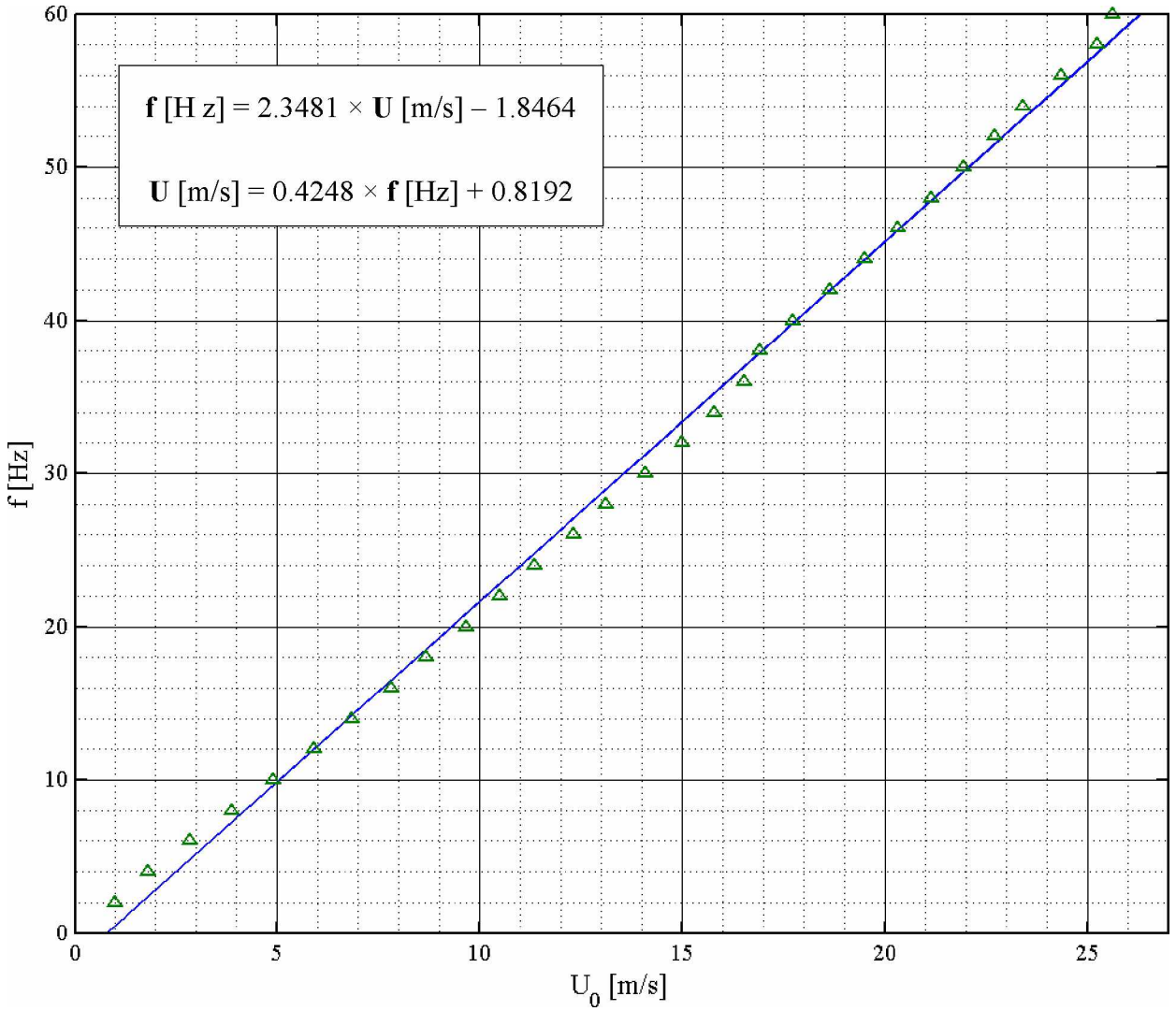

Figure V – Wind-tunnel calibration